Winter 1993

Studies of rotationally inelastic collisions in argon + hydrogen fluoride

James J C Barrett
University of New Hampshire, Durham

Order Number 9420560

Studies of rotationally inelastic collisions in Ar + HF

Barrett, James J. C., Ph.D.

University of New Hampshire, 1993

U·M·I
300 N. Zeeb Rd.
Ann Arbor, MI 48106

STUDIES OF ROTATIONALLY INELASTIC COLLISIONS IN Ar + HF

By

JAMES J.C. BARRETT
B.S., Eastern Michigan University, 1985

DISSERTATION

Submitted to the University of New Hampshire
in Partial Fulfillment of
the Requirements for the Degree of

Doctor of Philosophy

in

Chemistry

December, 1993

This dissertation has been examined and approved.

Dissertation director, Howard R. Mayne
Associate Professor of Chemistry

Frank L. Pilar
Professor of Chemistry, Emeritus

Colin D. Hubbard
Professor of Chemistry

Paul R. Jones
Professor of Chemistry and
Chairperson of Chemistry Department

Dawn C. Meredith
Associate Professor of Physics

12-1-93
Date

DEDICATION

This work is dedicated to the most important people in my life.
whose sacrifices have made this accomplishment possible.
My wife, my son and my parents.

ACKNOWLEDGEMENTS

First and foremost I wish to acknowledge my advisor Professor Howard R. Mayne. Without his guidance and patience I would not be here today. I first met Howard at Eastern Michigan University. He was my Physical Chemistry instructor and I also did my undergraduate research with him. This research was my first introduction into the field of Chemical Physics. This initial work fired my imagination. After three years of managerial work, I was still inspired by my early research with Dr. Mayne and decided to pursue a Ph. D. in Theoretical Chemistry. By this time Howard had taken his current position at the University of New Hampshire and he played a pivotal role in my acceptance to graduate school here. Over the years our relationship has covered all aspects from friend to foe, teacher to student. I wish to thank him for his help support and encouragement over the years. Howard is responsible for my coming to New Hampshire and to this day I am not sure whether this is a curse or a compliment.

My thanks are given to Professor Mark Keil, University of Oklahoma, who initially got us started on the Ar+HF problem. I would also like to thank the members of Prof. Keil's research for their experimental and theoretical results. I am also grateful to Professor M. A. Alexander, University of Maryland, for the quantum close-coupled results reported here.

During my time at U.N.H I have had the good fortune to make many wonderful friends, the most important of these is Yu Chen. She is so important a friend to me that two and a half years ago we were married. She is a person whom I love and respect both as a scientist

and as a person. I wish to thank her for her care and support during the writing of this dissertation.

Among the other friends I have made during my time here, I would like to give particular acknowledgement to Jay and Janelle Niesse and to their beautiful daughter Liz, who has made my life so much brighter by being in the world. I would also like to thank Dan and Darlene Hill, Jamie Clothier and Jon Asbjornson for their continued friendship and support.

I cannot forget each of the players on the Chemistry Department softball teams the Freebases and the Buckyballs. Especially the Buckyballs for giving me the opportunity to contribute to a CHAMPIONSHIP team.

Finally, I would like to acknowledge my son Justin Koch. The time that I've taken from you while completing this degree can never be replaced. Let's hope that we will make better use of the times still to come.

TABLE OF CONTENTS

LIST OF FIGURES

LIST OF TABLES

LIST OF ABBREVIATIONS

BF	Body fixed
CoM	Center of mass frame
CC	Close-coupled
$\mathbf{u}$	CoM velocity
CS	Coupled states
σ	Integral cross section
DCS	Differential cross section
ES	Energy sudden
E_{coll}	Relative collision energy
HFD	Hartree-Fock damped dispersion
HH	Hutson and Howard
HX	Hydrogen halide
b	Impact parameter
IOSA	Infinite order sudden approximation
Θ	Lab scattering angle
$\mathbf{v}$	Lab velocity
Lab	Laboratory frame
meV	Millielectron volts
MC	Monte Carlo
NCC	Nesbitt, Clary and Child
θ_r	Center of mass rainbow angle
Rg	Rare gas atom
θ	Center of mass scattering angle
$S_1, S_2, S_{1/2}$	Test potential energy sufaces, S_2 and $S_{1/2}$ have a well depth of 2X and 0.5X that of surface S_1
SC-CS	Semiclassical coupled states
SC-ES	Semiclassical energy sudden
SC-IOS	Semiclassical infinite order sudden
SF	Space fixed
vdW	van der Waals

ABSTRACT

STUDIES OF ROTATIONALLY INELASTIC
COLLISIONS IN Ar + HF
by

James J. C. Barrett
University of New Hampshire, December, 1993

In this dissertation we examine rotationally inelastic collisions involving an atom plus a diatom. We concentrate specifically on the Ar+HF system. In these investigations we employ a number of theoretical methods, including classical trajectories, quantum close-coupled calculations and semiclassical methods, to examine the differential cross sections in Ar+HF. We also investigate the effects of various "sudden" approximations on the scattering dynamics and the limitations of these approximations.

Through this work we were able to identify a new quantum feature in rotationally inelastic scattering. By studying the time evolution of transition amplitudes (rather than probabilities) we are able to ascribe this feature to a balance between the attractive and repulsive parts of the potential energy surface governing the collision system. We propose that this feature will be a general scattering feature in systems with a potential that has substantial repulsive anisotropy and a significant attractive well.

We present a classical trajectory method for direct simulation of a scattering experiment. We use this method to calculate laboratory frame differential cross sections for rotationally inelastic scattering in the Ar+HF system. We find that the results of this method are in excellent agreement with more standard approaches for the comparison of theoretical to experimental results.

Chapter 1

Introduction

A major goal of all chemists is to understand the fundamental workings of the chemical reaction at the molecular level. Molecular beam scattering studies have provided chemists and chemical physicists with a powerful tool for attaining this goal and has opened up the field of chemical reaction dynamics.[1] The importance of this work has been acknowledged by the awarding of the 1986 Nobel Prize in Chemistry to three recent practitioners in this field, D. R. Herschbach, Y. T. Lee and J. C. Polanyi.

With the development of the early molecular beam experiments[2] chemists began to gain control over specific reaction conditions. Use of these techniques provides the capability to explore reactions under single collision conditions with great control over the initial state of reactants and the energies at which they collide. The continued development of better and more sophisticated vacuum chambers and pumps, as well as invention and innovation in the area of detection techniques have allowed for the

identification of not only the reaction products, but also their internal energy state. Combining the molecular beam techniques with these sophisticated detection schemes has enabled investigators to approach the goal of experimentally probing state-to-state chemical reactions.

The development of these exciting experimental techniques has been joined, and sometimes led, by advances in theoretical methods for investigating these processes.[3] Early quantum mechanical studies could describe reactions for systems containing only the fewest number of electrons and focused on the simplest of all chemical reactions, the hydrogen exchange reaction.[4] This reaction continues to hold many secrets that today's modern computers and most sophisticated experiments are still trying to unlock.[5]

Development of the classical trajectory method[6] (which had been originally applied to the $H+H_2$ reaction) allowed for the investigation of an ever increasing variety of systems, including protein simulation.[7] This technique gave chemists a new tool for probing deeper into the nature of the chemical reaction. Comparing the results from quantum and classical dynamics, and finding differences between them, led to the acknowledgement of the importance of "quantum effects" in chemical reactions.[8]

In all of these studies the limiting factor of our ability to model the reaction process is our understanding of the potential energy surface. In classical terms, this potential governs the motion of the particles as they approach one another as reactants and separate as products. Quantum mechanically, the Hamiltonian determines the time-dependent evolution of the wave function for the system under investigation.

Many methods have been employed for the accurate determination of the potential energy surface.[9] *Ab initio* methods have been successful in determining the surface for small molecular systems.[10] However, for large molecular systems *ab initio* methods can be very inefficient. By contrast, semi-empirical methods have been employed with great success for very large molecular systems.[11] Use of semi-empirical potentials in molecular mechanics calculations have been very fruitful in understanding of the dynamics and conformations of large biological molecules.[12] The parameters used in these semi-empirical potentials are fit to experimental data on the components of these large molecules.[13] These data include transport properties, dipole moments and spectroscopic information.

Spectroscopy has become an important source of information on a large variety of van der Waals molecules.[14] Through the investigation of bound state vibrational modes and internal rotations of these systems a great deal of information may be gained, particularly on the attractive minimum of the surface.[14] This has been exploited to great advantage in the study of atom+diatom van der Waals complexes. A prototype system for this type of investigation has been the Ar+HF complex.[15]

Spectroscopic studies, however, provide very little information on the repulsive part of the potential surface. Scattering experiments probe this part of the surface and thus provide complementary information to that from spectroscopy.[16] In particular, rotationally inelastic scattering can provide information on the repulsive anisotropy of the potential.[17]

Recently, experiments on the scattering of hydrogen fluoride from argon have been conducted.[18,19] These studies have provided integral[18] and differential cross sections[19] for

this system. A very recent crossed molecular beam scattering experiment has employed a laser+bolometer detection scheme to provide final state-selected differential cross sections for rotationally inelastic Ar+HF scattering of the hydrogen fluoride in the ground vibrational state.[20] This study revealed novel features in the differential cross sections. In this dissertation we explain the origin of these features and relate them back to the potential energy surface.

In Chapter 2 of this dissertation we briefly review the four most recent potential energy surfaces for the Ar+HF system. We discuss the origin of these surfaces and provide some analysis of the surfaces. Chapter 3 introduces some of the basic concepts employed in scattering theory by carrying out scattering studies on several model potential energy surfaces. In this chapter we examine the effects of different regions of the potential on observed scattering features.

In Chapter 4 we perform classical scattering studies on the Ar+HF system using the four surfaces discussed in Chapter 2. The calculations are conducted so as to model the experimental conditions of reference 20. We also compare the classical differential cross sections to the experimental results and find substantial differences between them. In order to understand the origin of these differences, we compare the classical results to quantum calculations for this system on the "best" available potential surface. These are also compared to the experiment and we find very good agreement between the quantum and experimental results.

In Chapter 5 the disagreement between the quantum and classical calculations is explored in greater detail. We find that there is evidence of a new quantum mechanical scattering feature in this system. This feature may be generally observed in rotationally inelastic scattering on potential energy surfaces which are strongly attractive and have

substantial anisotropy. In the final chapter we investigate the breakdown of several well known sudden approximations commonly used in rotationally inelastic scattering calculations.

References

1. Special issue of Ber. Bunsenges. Phys. Chem., **86**, 348-483 (1982)
2. W. B. Miller, S. A. Safron and D. R. Herschbach, Discuss. Faraday. Soc., **44**, 108 (1967);
   Y. T. Lee, J. D. McDonald, R. P. LeBreton and D. R. Herschbach, J. Chem. Phys., **49**, 2447 (1968)
3. J. O. Hirschfelder, Ber. Bunsenges. Phys. Chem., **86**, 349 (1982)
4. A. Kuppermann and G. C. Schatz, J. Chem. Phys., **62**, 2502 (1975)
5. D. A. V. Kliner, A. D. Adelman and R. N. Zare, J. Chem. Phys., **95**, 214 (1991)
6. M. Karplus, R. M. Porter and R. D. Sharma, J. Chem. Phys., **43**, 3259 (1965)
7. C. L. Brooks, III, M. Karplus and B. M. Pettitt, Adv. Chem. Phys., **71**, 1 (1988)
8. P. Kollman, Ann. Rev. Phys. Chem., **38**, 303 (1987);
   D. G. Truhlar, ed., *Resonances in Electron-Molecule Scattering, van der Waals Complexes and Reactive Chemical Dynamics Calculations*, ACS Symp. Ser. 263., Am. Chem. Soc., Washington, DC, (1984), 552;
   G. C. Schatz, Ann. Rev. Phys. Chem., **39**, 317 (1988)
9. A. D. Buckingham, P. W. Fowler and J. M. Hutson, Chem. Rev., **88**, 963 (1988);
   G. C. Maitland, M. Rigby, E. B. Smith and W. A. Wakeham, *Intermolecular Forces*, Clarendon, London, (1981)
10. J. S. Binkley and J. A. Pople, Int. J. Quant. Chem., **9**, 229 (1975);
    D. M. Silver, Comp. Phys. Commun., **14**, 91 (1978)
11. L. Dunfield, A. Burgess and H. Scheraga, J. Phys. Chem., **82**, 2609 (1978)
12. H. A. Scheraga, Adv. Phys. Org. Chem., **6**, 103 (1968);
    U. Burkett and N. L. Allinger, *Molecular Mechanics*, American Chemical Society, Washington, D. C. (1982)
13. L. Nilsson and M. Karplus, J. Comp. Chem., **7**, 591 (1986)
14. J. M. Hutson, Ann. Rev. Chem. Phys., **41**, 123 (1990)
15. J. M. Hutson and B. J. Howard, Mol. Phys., **45**, 791 (1982);
    D. J. Nesbitt, M. S. Child and D. C. Clary, J. Chem. Phys., **90**, 4855 (1989);
    J. M. Hutson, J. Chem. Phys., **96**, 6752 (1992)
16. U. Buck, H. Meyer and R. J. LeRoy, J. Chem. Phys., **80**, 5589 (1984)
17. P. L. Jones, U. Hefter, A. Mattheus, J. Witt, W. Müller, W. Meyer and R. Schinke, Phys. Rev. B, **26**, 1283 (1982)
18. J. A. Barnes, M. Keil, R. E. Kutina and J. C. Polanyi, J. Chem. Phys., **76**, 913

(1982)
19. P. F. Vohralik, R. E. Miller and R. O. Watts, J. Chem. Phys. **90**, 2182 (1989)
20. Rawluk, Y. B. Fan, Y. Apelblat and M. Keil, J. Chem. Phys., **94**, 4205 (1991)

Chapter 2

Review of Ar+HF Potential Energy Surfaces

I. Introduction

In this chapter we briefly review four of the most recent potential energy surfaces available for the Ar+HF system.[1,2,3,4] We will discuss the methods employed in the development of these surfaces and the spectroscopic data used in their construction. This is not meant as an exhaustive review on the literature on this system. However we do wish to provide some general background as to the origin of these surfaces. For the interested reader, an excellent review of the construction of potential energy surfaces for van der Waals complexes from spectroscopic data is available.[5]

In addition to discussing the general features of the Ar+HF potentials, we also analyze the differences between the four surfaces. The implications of these differences for rotationally inelastic scattering will be discussed in the following Chapters.

II. Potential Energy Surfaces

All of the following potential energy surfaces for the Ar+HF system[1-4] will be used in trajectory calculations for

the scattering of a rigid rotor diatom from a rare gas atom. Therefore, each of these surfaces is vibrationally averaged over the internuclear bond coordinate, so that the potential is given as a function of R and γ, the intermolecular separation and orientation angle, respectively.

Two of the surfaces, reference 1, referred to hereafter as "HH M5", and reference 2, referred to as "Douketis", are constructed for HF in the ground vibrational state. The surface in reference 3 was developed from spectroscopic data of the Ar•HF complex with the hydrogen fluoride in the v=1 vibrational state. The Hutson H6 surface, reference 4, is a much more sophisticated potential, as will be discussed below.

The HH M5 surface[1] was developed using a non-linear least squares fitting procedure[6] to molecular beam electronic resonance spectroscopy[7] on the Ar•HF(v=0) van der Waals (vdW) complex. The Douketis surface[2] was developed from a Hartree-Fock damped dispersion (HFD) *ab initio* calculation[8] on Ar•HF(v=0). In prior work,[9] it was found that the attractive part of a previous HFD potential[10] was required to be increased by ~16% in order to accurately reproduce total differential cross sections for Ar+HF scattering.[9] A similar procedure for the Douketis surface was carried out to fit the surface to some of the available spectroscopic data.[2] The NCC surface[3] was fit to infrared spectroscopic data for the Ar•HF van der Waals complex, with HF in vibrational state, v=1, using an RKR inversion method.[11]

The Hutson H6 potential,[4] is the most sophisticated potential function of the four surfaces considered in this study. The surface is developed from a multi-parameter fit to all available spectroscopic information available (at the time of publication) on the Ar•HF complex.[12] This work included spectroscopic information on the Ar•DF complex, with

DF in the ground state[13] as well as vibrationally excited DF.[14] The spectroscopic database also included work on vibrationally excited Ar•HF complexes.[15]

The H6 potential surface was constructed to incorporate HF vibrational states, v=-1/2 (rigid rotor), 0, 1, 2. It also incorporates isotopic substitution of D for H in the diatom.[4] As a test of the validity of the surface, calculations using the H6 surface correctly reproduced transition frequencies for the Ar•HF vdW complex, not included in the fitting data base.[4] The surface has also been used to predict transition frequencies in the Ar•HF spectrum,[16] which were subsequently located by new spectroscopic experiments.[17]

While the four surfaces used in this study are quantitatively different, they are qualitatively similar. The general features common to each of these potentials are: (1) Preferred geometry in the FH···Ar configuration (γ=0°); (2) Secondary minimum in the HF···Ar configuration(γ=180°); (3) Strongly anisotropic, attractive potential; binding energy ranging from 20-30 meV.

In figures 1-3 we show various views of the potential energy surfaces[1-4] for the Ar+HF system used in this study. In figure 1 we present relief plots for each of the four surfaces. These plots are set up so that the HF center of mass lies at the origin of the diagram with the "H-end" of the diatom to the right side of the front axis. The radial distance from the origin indicates the internuclear separation, the orientation angle, γ, as defined above is given as zero along the positive ordinate.

In figure 2 we plot the potential as a function of γ at several fixed values of R. The differences in the repulsive wall anisotropy are seen in figures 2(a) and 2(b) for R=2.5 Å and R=3.0 Å. It is evident from these figures that the NCC

potential shows the least anisotropy in the repulsive region, whereas the HH M5 surface displays the most dramatic repulsive anisotropy. These plots also indicate the asymmetric (about γ=90°) nature of the potential. The slices near the attractive minima are taken as near as possible to absolute minimum of each surface to show the attractive anisotropy of each surface.

The location and energy of the minima for each surface are more easily seen in figure 3, where the potentials are displayed as a function of R at a fixed value of γ. The values and locations of the potential minima for each surface are listed in Table 1. Figures 3(a) and 3(c) also show that the "H" end of the system is more steeply repulsive than the "F" end.

We now would like to make a more quantitative comparison between the potential energy surfaces. However, the functional forms of each of the potentials are vastly different. In order to put each of the surfaces on an equal footing for comparison, we expand each of the surfaces in a normalized Legendre basis, $\tilde{P}_l(\cos\gamma)$. The functional form of the expansion is given by

$$V(R,\gamma) = \sum_{l=0}^{\infty} V_l(R)\tilde{P}_l(\cos\gamma) \qquad (1)$$

written in this manner the expansion is exact. In practice, however, the expansion is truncated at some reasonable value, N. For the comparison made here, we truncate the expansion at N=5.

Using the orthonormality relationships of the Legendre basis, i.e.

$$\int_{-1}^{1} d(\cos\gamma)\tilde{P}_l \tilde{P}_{l'} = \delta_{ll'} \qquad (2)$$

we can solve for the expansion coefficients, $V_l(R)$, explicitly by

$$C_l(R) = \int_{-1}^{1} d(\cos\gamma)\tilde{P}_l(\cos\gamma)\, V(\cos\gamma; R) \qquad (3)$$

at some fixed value of R. The integration of equation 3 is carried out by Gauss-Legendre quadrature.[18,19] The expansion coefficients at several values of R for each surface are given in Table 2. From these coefficients it is readily seen that the HH M5 surface does indeed display the most anisotropic character in the repulsive wall, while the anisotropy of the NCC potential arises from $\tilde{P}_1$ and $\tilde{P}_2$ only. We will use these expansion coefficients in later Chapters to qualitatively and quantitatively compare the scattering dynamics on each of these surfaces.

References

1. J. M. Hutson and B. J. Howard, Mol. Phys., **45**, 791 (1982)
2. C. Douketis, J. M. Hutson, B. J. Orr and G. Scoles, Mol. Phys., **52**, 763 (1984)
3. D. J. Nesbitt, M. S. Child and D. C. Clary, J. Chem. Phys., **90**, 4855 (1989)
4. J. M. Hutson, J. Chem. Phys., **96**, 6752 (1992)
5. J. M. Hutson, Ann. Rev. Phys. Chem., **41**, 123 (`1990)
6. J. M. Hutson and B. J. Howard, Mol. Phys., **45**, 769 (1982)
7. S. J. Harris, S. E. Novick and W. Klemperer, J. Chem. Phys., **74**, 6539 (1981); R. M. Keenan, L. W. Buxton, T. J. Balle and W. H. Flygare, Chem. Phys., **54**, 173 (1981)
8. J. Hepburn, G. Scoles and R. Penco, Chem. Phys. Lett., **36**, 451 (1975); R. Ahlichs, R. Penco and G. Scoles, Chem. Phys., **19**, 119 (1977); C. Douketis, G. Scoles, S. Marchetti, M. Zen and A. J. Thakkar, J. Chem. Phys., **76**, 3057 (1982); W. R. Rodwell and G. Scoles, J. Phys. Chem., **86**, 1053 (1982)
9. P. F. Vohralik, R. E. Miller and R. O. Watts, J. Chem. Phys., **90**, 913 (1982)
10. W. R. Rodwell, L. T. Sin Fai Lam and R. O. Watts, Mol. Phys., **44**, 2265 (1981)
11. R. Rydberg, Z. Phys., **73**, 326 (1931); *ibid.*, **80**, 514 (1933); O. Klein, *ibid.*, **76**, 226 (1932); A. L. G. Rees, Proc. Phys. Soc. London, **59**, 998 (1947); J. Tellinghuisen, Comput. Phys. Commun., **6**, 221 (1974); M. S. Child and D. J. Nesbitt, Chem. Phys. Lett., **149**, 404 (1988)
12. C. M. Lovejoy, M. D. Schuder and D. J. Nesbitt, Chem. Phys. Lett., **127**, 374 (1986); G. T. Fraser and A. S. Pine, J. Chem. Phys., **85**, 2502 (1986); C. M. Lovejoy, M. D. Schuder and D. J. Nesbitt, J. Chem. Phys., **85**, 4890 (1986); Z. S. Huang, K. W. Jucks and R. E. Miller, J. Chem. Phys., **85**, 6905 (1986)
13. T. A. Dixon, C. H. Joyner, F. A. Baiocchi and W. Klemperer, J. Chem. Phys., **74**, 6539 (1981); M. R. Keenan, L. W. Buxton, E. J. Campell, A. C. Legon and W. H. Flygare, J. Chem. Phys., **74**, 2133 (1981)
14. C. M. Lovejoy, J. M. Hutson and D. J. Nesbitt, J. Chem. Phys., **97**, 8009 (1992)
15. C. M. Lovejoy and D. J. Nesbitt, J. Chem. Phys., **91**, 2790 (1989);

M. A. Dvorak, S. W. Reeve, W. A. Burns, A. Grushow and K. R. Leopold, Chem. Phys. Lett., **185**, 399 (1991);
J. T. Farrell, Jr., O. Sneh, A. McIlroy, A. E. Knight and D. J. Nesbitt, J. Chem. Phys., **97**, 7967 (1992)

16. Reference 4, Table IX.
17. Results from preliminary H6 potentials used to guide experiments in reference 14. (See section XIII of reference 4.)
18. *Handbook of Mathematical functions with Formulas, Graphs and Mathematical Tables*, ed. M. Abramowitz and I. A. Stegun, NBS Applied Mathematics Series #5 (1964) p. 887
19. W. H. Press, S. A. Teukolsky, W. T. Vetterling and B. P. Flanery, *Numerical Recipes*, Cambridge U. Press, New York (1992) pp. 145-148

Table 1. R_{min} and potential energy at several values of γ for each Ar+HF potential employed in this study.

Hutson H6		
R_{min} [Å]	γ [degree]	-V(R,γ) [meV]
3.434	0°	27.30
3.496	90°	8.310
3.375	180°	13.33
HH M5		
R_{min} [Å]	γ [degree]	-V(R,γ) [meV]
3.390	0°	26.56
3.456	90°	10.34
3.346	180°	9.918
Douketis		
R_{min} [Å]	γ [degree]	-V(R,γ) [meV]
3.45	0°	28.92
3.45	90°	11.38
3.30	180°	16.82
NCC		
R_{min} [Å]	γ [degree]	-V(R,γ) [meV]
3.400	0°	26.78
3.550	90°	8.894
3.400	180°	16.24

Table 2. Expansion coefficients for each potential energy surface used in this study at several values of R. Coefficients given in meV/Å.

Hutson H6						
R [Å]	$C_0(R)$	$C_1(R)$	$C_2(R)$	$C_3(R)$	$C_4(R)$	$C_5(R)$
2.5	414.8	82.83	69.95	39.75	22.65	0.2378
3.0	13.16	2.136	-1.013	2.297	0.6122	0.0074
3.5	-17.62	-3.290	-3.546	-1.310	-0.8480	-0.0268
4.0	-11.24	-2.231	-1.778	-0.9012	-0.4810	-0.0108
5.0	-2.988	-0.5152	-0.3857	-0.2145	-0.0973	-0.0004
6.0	-0.9196	-0.1355	-0.1089	-0.0552	-0.0222	0.0001
HH M5						
R [Å]	$C_0(R)$	$C_1(R)$	$C_2(R)$	$C_3(R)$	$C_4(R)$	$C_5(R)$
2.5	737.0	579.9	555.4	491.6	396.7	313.7
3.0	17.38	12.92	7.263	7.191	4.391	2.765
3.5	-15.36	-4.454	-3.665	-1.353	-0.3301	-0.0293
4.0	-9.062	-2.567	-1.754	-0.5707	0.0080	0.1167
5.0	-2.374	-0.6718	-0.4367	-0.1400	0.0094	0.0339
6.0	-0.7555	-0.2179	-0.1435	-0.0485	0.0002	0.0092
Douketis						
R [Å]	$C_0(R)$	$C_1(R)$	$C_2(R)$	$C_3(R)$	$C_4(R)$	$C_5(R)$
2.5	386.3	65.33	34.01	32.80	19.37	22.51
3.0	9.555	4.359	-2.194	2.590	0.6120	0.2889
3.5	-20.35	-3.501	-4.115	-0.8929	-0.3773	-0.2012
4.0	-12.66	-2.246	-2.089	-0.6390	-0.1875	-0.0509
5.0	-3.377	-0.5018	-0.4405	-0.1456	-0.0340	-0.0059
6.0	-1.063	-0.1316	-0.1224	-0.0381	-0.0077	-0.0012
NCC						
R [Å]	$C_0(R)$	$C_1(R)$	$C_2(R)$	$C_3(R)$	$C_4(R)$	$C_5(R)$
2.5	674.6	150.1	92.21	0.000	0.000	0.000
3.0	16.50	2.639	-2.643	0.000	0.000	0.000
3.5	-18.22	-4.294	-5.057	0.000	0.000	0.000

4.0	-11.68	-2.634	-2.282	0.000	0.000	0.000
5.0	-3.479	-0.5970	-0.4772	0.000	0.000	0.000
6.0	-1.198	-0.1925	-0.1502	0.000	0.000	0.000

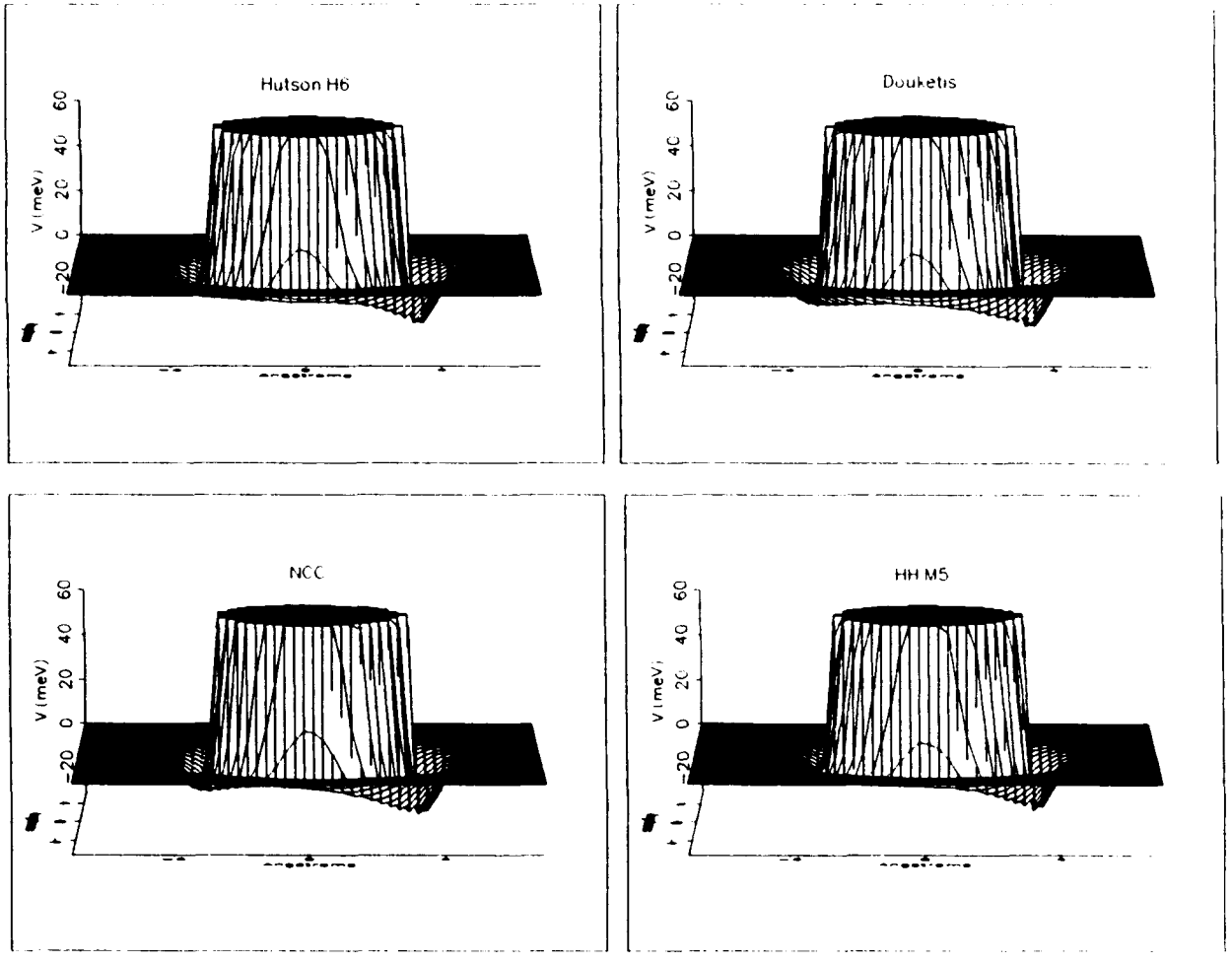

Figure 1. Relief plots of the Ar + HF potential energy surfaces.

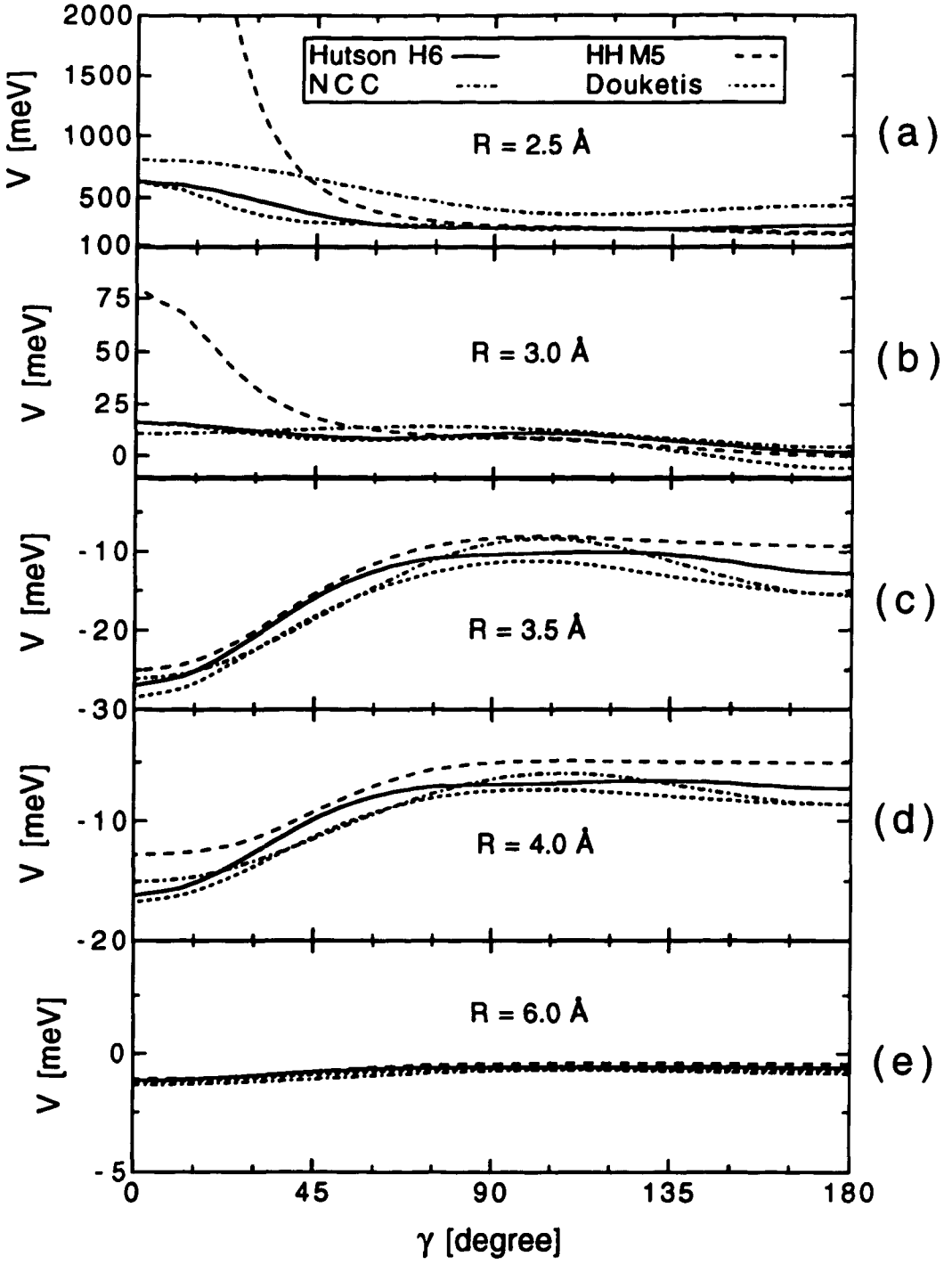

Figure 2. Potential shown as a function of γ at several values of R.

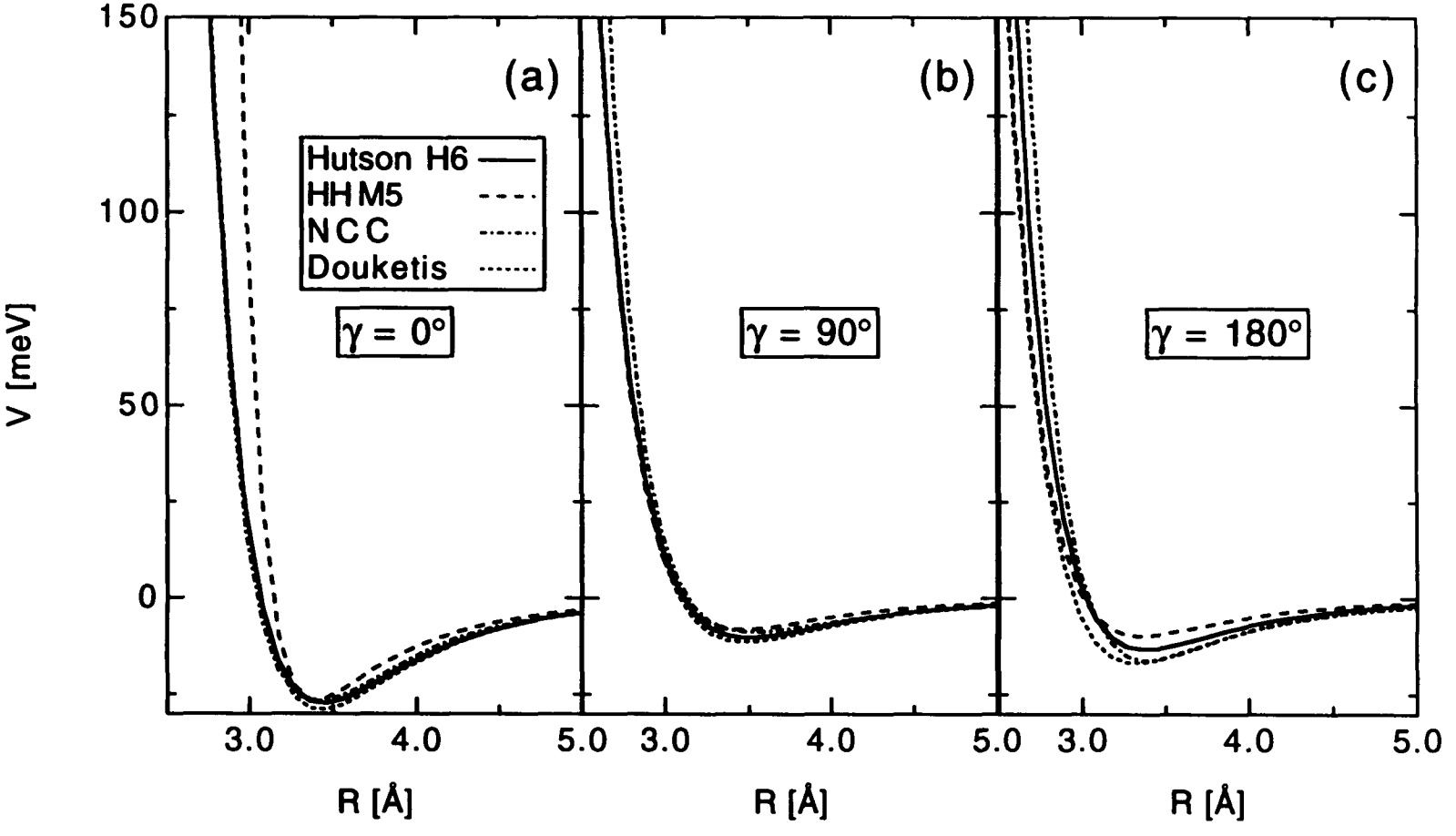

Figure 3. Potentials shown as a function of R at several values of γ.

Chapter 3

Scattering on Model Potential Energy Surfaces

I. Introduction

Rotationally inelastic scattering in atom + diatom systems has been an exciting field of research for a number of years.[1] This research has produced a rich literature relating observed scattering features to the potential energy surface which produced the scattering event.[2] Along with the vast experimental literature on rotationally inelastic scattering,[3] many powerful theoretical models have been developed to investigate these processes.[4]

The bulk of the experimental and theoretical work on rotationally inelastic scattering has focused on systems which involve homonuclear diatoms and potential energy surface which are predominantly repulsive in nature.[5] Examples of this type of scattering system are He+Na_2,[6] Rg+H_2,[7] and Rg+N_2[8] where Rg refers to a rare gas atom. Some work has been carried out on heteronuclear diatom systems, such as Rg+NO[9] and Rg+LiH;[10] however, these systems again are predominantly repulsive.

Many rotationally inelastic scattering experiments reveal a rich structure in the angular distribution (the

differential cross section) of the scattered products. Features such as the rotational rainbow have been predicted computationally[11] and observed experimentally.[12] The implications of rotational rainbow scattering as a source of information on the potential energy surface have also been discussed. The development of simple, efficient computational methods for investigating rotationally inelastic scattering, such as the infinite order sudden approximation (IOSA),[13] have also been important in furthering our understanding of these types of processes.

For atom+diatom systems, in which there exists an attractive well capable of sustaining bound states, the most reliable source of information on the potential energy surface has been spectroscopic studies of the bound complex.[14] Prototype systems for these types of studies have been rare gas + hydrogen halide (Rg+HX) systems.[15] In particular, Ar+HCl[16] and Ar+HF[17] have been very well studied.

Spectroscopic studies of the van der Waals dimers of Rg+HX complexes have led to potential energy functions in which the region of the primary attractive minimum has been well characterized.[18] Recent spectroscopic studies[19] on Ar•HF have made it possible to construct a potential function of high sophistication which not only characterizes the primary minimum, but also provides an excellent representation of the total attractive anisotropy.[20]

Spectroscopic studies of van der Waals complexes provide detailed information on the attractive part of the potential. However, spectroscopic data give very little information on the repulsive part of the potential energy surface. Scattering studies, on the other hand, probe the repulsive part of the potential and rotationally inelastic scattering studies give information on the repulsive anisotropy of the surface.[21] Unfortunately, it is very

difficult to extract detailed information on the potential surface from scattering studies for systems which have substantial attractive character.[22]

Several scattering studies on Rg+HX systems have been undertaken in recent years.[23] In particular, the Ar+HF system has received a great deal of attention.[24] Interesting features have been observed in rotationally resolved differential cross sections (DCS) for this system.[25] The scattering dynamics in Ar+HF have also been investigated theoretically.[26] Scattering data give information on the potential surface which is complementary to that obtained by spectroscopic measurements. Therefore, it is necessary to understand the details of the collision dynamics for systems such as Ar+HF, or Rg+HX systems in general, in order to use the information obtained from molecular beam scattering experiments to refine the potential energy function.

To gain insight into the complicated scattering dynamics of systems such as Ar+HF, we present scattering calculations on several model potential energy surfaces. We use the model potentials in this study to gain control over the attractive well depths and the attractive and repulsive anisotropies. By employing a simple functional form for the potential, without regard to fitting a potential energy function to a particular atom + diatom system, we may arbitrarily adjust the potential parameters and attempt to correlate the scattering features to changes in the potential energy surface.

In Section II we present the potential functions used in this study. In Section III we present the computational methods employed in the scattering calculations, including the methods by which the integrals necessary for implementation of the scattering calculations are computed. An alternative computational approach is also mentioned. Also

in Section III, the computational methods for calculating the differential cross sections from the deflection and opacity functions generated from the scattering calculation are given. The results from the scattering calculations using the model potentials are discussed in Section IV. In Section V we present integral cross sections calculated for Rg+HF scattering, where the mass of the Rg atom is changed, but the calculations are performed using the same potential surface in each case. The potential surface used in this part of the study is the Hutson potential for Ar+HF.[20] Concluding remarks are made in Section VI.

II. Model Potential Energy Surfaces

The potential energy surfaces for Rg+HX systems are unlike those employed for many previous studies of rotationally inelastic scattering.[27] General features of Rg+HX potentials include a primary minimum in the collinear X-H···Rg configuration. There is also a secondary minimum in the collinear H-X···Rg configuration. The potential surfaces also have substantial repulsive anisotropy.

In order to account for these features in a simple potential function, the potential is written as an expansion in the normalized Legendre polynomials, $\tilde{P}_\lambda$. The function is given as

$$V(R,\gamma) = \sum_{\lambda} V_\lambda(R)\tilde{P}_\lambda(\cos\gamma) \qquad (1)$$

where R is the internuclear separation from the atom to the diatom center-of-mass, γ is given as the angle between the diatom bond vector, **r**, and the vector **R**. By convention γ=0° in the X-H···Rg configuration and γ=180° in the H-X···Rg

configuration. The expansion is truncated at λ=5. The R dependent part of the potential, $V_\lambda(R)$, is in the form of a Lennard-Jones 6-12 function, given as

$$V_\lambda(R) = 4\varepsilon_\lambda\left(\left(\frac{\sigma_\lambda}{R}\right)^{12} - \left(\frac{\sigma_\lambda}{R}\right)^{6}\right) \qquad (2)$$

where ε_λ is the attractive well depth and σ_λ is the value of R at which V=0, for each term in the expansion. This functional form allows for a high level of flexibility and reproduces the essential features common to the Rg+HX surfaces.

Problems associated with using a Lennard-Jones or Morse type function in systematic scattering studies have been pointed out in the past.[28] Of particular note is the dependence of the repulsive part of the potential on the ε parameter in the Lennard-Jones function. Thus by adjusting the well depth, the repulsive part of the surface is also affected. However the convenient form of these functions lends itselve well to computational studies and has been used frequently in the past.[29] As discussed below, great care has been taken to minimize the effect due to differences in the repulsive part of the potential.

In this study we also employ a repulsive surface, denoted hereafter as REP, as a "control". Use of a repulsive surface allows the elucidation of the role played by the attractive anisotropy in the scattering dynamics. This function is also written as a Legendre expansion and has the form of eq.1, with the R dependent part of the potential given by

$$V_\lambda(R) = 4\varepsilon_\lambda\left(\frac{\sigma_\lambda}{R}\right)^{14} \qquad (3)$$

Three attractive surfaces are employed in this study. The surface 1 (S_1) is qualitatively fit to the Hutson H6 potential for Ar+HF.[20] This fit is carried out by expanding the Hutson H6 potential in a normalized Legendre basis (truncated at λ=5) and determining the potential minimum (ε_λ) and R position where $V_\lambda(R)$ changes sign (σ_λ) for each expansion term. Surfaces 2 and 3 are generated by doubling and halving the ε_λ parameters of S_1, respectively. These three surfaces are plotted in figure 1. As can be seen from the figure, the repulsive anisotropies of these surfaces are substantially different. Of greatest concern is the position of the classical turning point (the position where the potential equals the collision energy, E_{coll}) on each each surface. The values of R when $V(R,\gamma=0°)$ = 135meV are listed in Table 1. In order to minimize these differences in the turning point on each surface, the σ_λ parameters for surfaces 2 and 3 are modified by -0.1Å and +0.1Å, respectively, from the S_1 values. The modified surfaces 2 and 3 (S_2 and $S_{1/2}$, respectively) are shown in figure 2 along with S_1.

The REP potential is constructed so that the repulsive wall anisotropy mimics the repulsive region of the Lennard-Jones surfaces. The surface is also adjusted so that the turning point is near 5.33 bohr. The REP potential is also shown in figure 2. The potential parameters for each of the surfaces are given in Table 2.

III. Computational Methods

A. Scattering Calculations

In this chapter we employ a semiclassical model to explore the collision dynamics of the Rg+HX scattering. We have used this model successfully[26(b)] to explain features observed experimentally in DCS for Ar+HF.[25] In the semiclassical (or classical path) model[30] the translational

coordinate is treated classically, while the internal degrees of freedom of the diatom are treated quantum mechanically. The classical equations of motion for the system are given by

$$\dot{\mathbf{R}} = \frac{\mathbf{P}}{M} \qquad ; \qquad \dot{\mathbf{P}} = -\nabla_{\mathbf{R}} \langle V(R,\gamma) \rangle \tag{4}$$

where **R** is the intermolecular vector from the diatom center of mass to the atom and **P** is its conjugate momentum. The reduced mass of the collision system, M, is given by

$$M = \frac{m_{Rg} * m_{HX}}{m_{Rg} + m_{HX}} \tag{5}$$

where m_{Rg} is the mass of a Rg atom and m_{HX} (= m_H+m_X) is the mass of the diatom. $\langle V(R,\gamma) \rangle$ is an appropriate angular average of the potential, at a fixed value of R. In this study we employ a spherical average over the potential energy function. It has been suggested that an Erhenfest average over the potential,[31] given as

$$\langle V \rangle = \langle \Psi(t) | V(t) | \Psi(t) \rangle \tag{6}$$

provides a more accurate description of the translational dynamics. We have compared the dynamics using a spherical average to the Erhenfest approach and find no significant difference in the collision dynamics, but achieve considerable time savings using the spherical average.

The time evolution of the diatom wave function is treated quantum mechanically by solution of the time-dependent Schrödinger equation. The time-dependent wave function for the diatom, $\Psi(t)$, is given as an expansion in a rigid rotor (spherical harmonic) basis set. The quantum equations of motion[32] are given by

$$i\hbar\dot{c}_k(t) = \sum_l c_k(t)\langle k|V(t)|l\rangle \exp\left(i^{(E_k - E_l)t}/_{\hbar}\right) \qquad (7)$$

where |k> and |l> represent rotational states, |j,m> and |j',m'> with an energy of E_k and E_k, respectively. The expansion coefficients, $c_l(t)$, are given by

$$c_l(t) = \langle l|\Psi(t)\rangle = \langle Y_{jm}|\Psi(t)\rangle \qquad (8)$$

where Y_{jm} is given explicitly as

$$Y_{jm}(\theta,\phi) = P_j^m(\cos\theta)\exp(i\,m\,\phi) \qquad (9)$$

with P_j^m being an associated Legendre function. The interaction potential, V(t), is made time-dependent through the classical translation, **R**(t). The integration of <k|V(t)|l> is performed by Gauss-Legendre quadrature over the θ coordinate and by trapezium rule over ϕ. To ensure numerical orthonormality in the numerical integration, the Gauss-Legendre quadrature requires $(j_{max}+1)$ points; the trapezium requires $2j_{max}$ points, where j_{max} is the highest rotational state employed in the expansion. Typically, $j_{max}=[(E_{coll}+Bj^2)/B]+2$, where the [] demotes the maximum integer function.

The quantum system may be represented in one of two coordinate systems, the space fixed(SF) coordinates or the body fixed(BF) system.[33] In the semiclassical approximation the coupling between m states arises naturally as the trajectory proceeds in the SF coordinate system. In the BF representation, the rotational basis is represented in a rotating coordinate system, with the z-axis oriented along the classical R vector. In this coordinate system, the m coupling is included through the Clebsch-Gordan coefficients and coordinate transformation matrix between the "fixed" (translational) coordinates and "rotating" basis.[34] The BF

coordinate system allows for the implementation of a simple approximation to reduce the dimensionality of the quantum equations of motion. This approximation includes coupling between only the rotational states where m'=m.[34] This is the semiclassical version of the coupled states (CS) approximation.[33,35]

In this chapter we use the semiclassical CS approximation for the bulk of our calculations. We have compared the semiclassical CS to a semiclassical calculation using full m-coupling and find the degeneracy-averaged results to be in very good agreement.

B. Deflection and opacity functions

In a scattering calculation, the deflection function is given by the scattering angle as a function of the impact parameter, $\theta(b)$.[36] While the deflection function is not "observable" in a molecular beam scattering experiment, computationally $\theta(b)$ gives a great deal of information on the potential energy surface governing the scattering dynamics. The scattering angle, θ, is defined as the angle between the initial and final classical relative momentum vectors, $\mathbf{P}$ and $\mathbf{P'}$, respectively,

$$|\theta| = \cos^{-1}\left(\frac{\mathbf{P'}\cdot\mathbf{P}}{|\mathbf{P'}||\mathbf{P}|}\right) \qquad (10)$$

The general trend of the scattering angle goes from θ=180° at b=0 to θ=0° as b→∞, for example see the REP $\theta(b)$ in figure 3. When scattering on an attractive potential surface the deflection function goes through a minimum, see S_1 $\theta(b)$ in figure 3, which is characteristic of the well depth to collision energy ratio. This minimum is known as the "rainbow" angle.[37]

The opacity function, the final rotational state probability as a function of impact parameter, is also an important quantity for analyzing scattering results and the potential surface. Examples of the opacity function for rotationally inelastic scattering can be seen in figures 4-6. In general lower b-values are associated with back scattering (high scattering angles) and large Δj transitions, see figure 6. High b-values are associated with forward scattering and small Δj transitions, for example see figure 4. These general trends hold for all potential energy surfaces; however in the mid-range impact parameters correlations of Δj with b may not be as straightforward.

The semiclassical probability of scattering from an initial state, l, into a final rotational state, k, at a given impact parameter, $P_{lk}(b)$, is given by

$$P_{l\to k}(b) = \left|c_k(t;b)\right|^2 \tag{11}$$

as time, t, approaches infinity. In this study we will be primarily concerned with the total scattering probability from an initial rotational level j, into a final rotational level j'. This is given as a weighted sum over the $|j,m\rangle$ states of the initial j level, times the sum of probabilities into the $|j'm'\rangle$ states of the final j' level,

$$P_{j\to j'}(b) = P_{jj'}(b) = \sum_{m=-j}^{j} \rho_{jm} \sum_{m'=-j'}^{j'} \left|c_{j,j'm'}(b)\right|^2 \tag{12}$$

where ρ_{jm} is the statistical weight of the initial rotational state $|jm\rangle$.

C. Differential Cross Sections

The angular distribution of the final rotational states, the differential scattering cross section (DCS), can be calculated from the opacity and deflection functions. The classical formulation for the DCS, $d\sigma/d\varpi$, is given by

$$\frac{d\sigma_{jj'}(\theta)}{d\varpi} = \sum_{i}^{n} \frac{b_i}{\sin\theta} \frac{P_{jj'}(\theta(b_i))}{\left|d\theta/db_i\right|} \qquad (13)$$

where $d\varpi = \sin\theta\, d\theta\, d\phi$. Due to the cylindrical symmetry of the scattering system in the center of mass frame, several impact parameters may contribute to the same scattering angle. The sum in equation 13 accounts for this. For $\theta<\theta_r$, n=3; for $\theta>\theta_r$, n=1, where θ_r is the rainbow scattering angle.

In this study the semiclassical trajectories are calculated, from b=0 up to b_{max}, in increments of Δb. For $b>b_{max}$, the transition probability, $P_{jj'}(b)=\delta_{jj'}$. In practice, trajectories are performed up to the lowest impact parameter for which the final rotational state probability remains in the initial state. At each impact parameter the trajectory is integrated until all rotational state probabilities have converged to four decimal places.

The calculation of the DCS from equation 13 is typically carried out at 1° increments. To do this, it is necessary to interpolate the opacity and deflection functions between the values generated from the trajectory calculation. This is carried out by a four-point Lagrange interpolation method[38] over $\theta(b)$ and $P_{jj'}(b)$. The derivative, $d\theta/db$, at a given value of b, is found by a four-point Lagrangian differentiation method[39] using the numerical deflection function values, $\theta(b_i)$.

The DCS gives detailed information on the scattering dynamics, however, the overall strength of the scattering transition is determined from the integral cross section, $\sigma_{jj'}$. We obtain $\sigma_{jj'}$ by integration of equation 13 to give

$$\sigma_{jj'} = 2\pi \int_{b=0}^{\infty} db\, b\, P_{jj'}(b) \qquad (14)$$

Detailed examination of the integral cross sections will be given in section V.

IV. Results and Discussion

The mass combination employed in the following calculations is that for an argon atom (m_{Rg}=40 amu) colliding with a hydrogen fluoride diatom (m_H=1, m_X=19 amu). The relative collision energy is 135meV; this corresponds to a relative collision velocity of 1.40 km/s. The initial diatom rotational state is j=0. For these initial conditions, the highest final rotational state is j'=6.

A. *Deflection functions*

We first examine the effect of the different potential surfaces on the deflection function; see figure 3. As expected,[40] the rainbow angle scales monotonically with an increase in well depth, while no minimum is observed in the deflection function for the repulsive REP surface. At a given collision energy, the rainbow angle may be used as a diagnostic for the attractive well depth of a potential surface.

From Fluendy and Lawley,[41] an empirical formula,

$$\theta_r = \frac{2\varepsilon_s}{E_{coll}}\left(\frac{180^\circ}{\pi}\right) \qquad (15)$$

relates the rainbow angle to a ratio of the spherical average of the potential well depth, ε_s, to the collision energy, E_{coll}. Using the ε_0 parameter, from each of the Lennard-Jones potentials, we can calculate an expected θ_r. As shown in Table 3, the θ_r values thus calculated are in good agreement with the rainbow angles from the trajectories.

Backscattering is generally considered to be a diagnostic of the repulsive part of the potential. Even though care was taken in constructing the potentials used here, the repulsive parts of each of the surfaces show some differences. The greatest difference between the surfaces is in the "hardness" or steepness of the surfaces. We can quantify this by calculating $(\partial V/\partial R)_\gamma$ for each of the surfaces at the collision energy, the values are listed in Table 4. The differences in the repulsive walls are evident in figure 3 by comparing the scattering angles at low impact parameters, i.e. b<6 bohr. For impact parameters in the range, 3<b<5 bohr, differences in scattering angle of approximately 15° are observed between the S_2 and REP surfaces, with surfaces S_1 and $S_{1/2}$ lying between S_2 and REP, in order of the steepness of the potential. These differences in the deflection function will affect the differential cross sections, as shown below.

B. *Opacity functions*

We now examine the opacity functions from each of the test potentials. These are shown in figures 4-6. First examine the opacity functions for the REP potential. The opacity function for $j=0\rightarrow j'=0$ (figure 4) on this surface shows a steadily increasing curve up to unity at b~7.0 bohr. No additional structure is observed in this opacity function. For the higher final rotational states (figures 5 and 6) the opacity functions show an essentially flat or slightly

decreasing function at low b, then drops rapidly to zero after some characteristic value of b. The b_{max} value for each j' decreases as j' increases.

Comparing the opacity functions for $S_{1/2}$ to REP, we can see that the addition of even a shallow attractive well has profound effects on the opacity function. For the 0→0 transition, (figure 4) the opacity functions are quite similar through b~5.5 bohr, with the probability increasing. At b=5.5 bohr the opacity function on the $S_{1/2}$ surface drops abruptly to a minimum, then rises to unity near b=11 bohr. The structure observed in the 0→0 opacity function is mirrored in the 0→1 transition probability. The peak seen for 0→0 at b~5.5 bohr is complemented by a minimum for 0→1, likewise, the minimum at b~7.0 bohr in 0→0 is complemented by a peak in the 0→1 opacity function. This "coupling" is not observed in any of the other opacity functions on the $S_{1/2}$ surface.

The j'=2 opacity function on the $S_{1/2}$ surface (figure 5) shows a steadily decreasing function, which fades slowly to zero near b~7.0 bohr. The higher j' (i.e. j'≥3) show a peak in the opacity functions, at decreasing values of b with increasing j'. After the peak the probabilities fall rapidly to zero, as was seen on the REP surface. In fact, all of the attractive surfaces exhibit this type of behavior for the high j' opacity functions. Furthermore, for j'=4 and 5 (figure 6) the opacity functions for all of the surfaces have very similar form. This indicates that the scattering dynamics for the highly inelastic collisions are determined mainly by the repulsive part of the potential. The role of the attractive part of the potential for these high Δj transitions is to increase the total inelasticity of the surface. This is indicated by the greater $P_{j'}(b)$ values on the surfaces with deeper well depths.

Returning to the opacity functions for the 0→0 and 0→1 transitions, (figure 4) we see that the coupling between j'=0 and j'=1 observed on the $S_{1/2}$ surface is also present on the S_1 and S_2 surfaces. Doubling the attractive well depth on surface S1 (over the $S_{1/2}$ surface) has shifted the first peak in the j'=0 opacity function 0.7 bohr to a lower impact parameter compared to the $S_{1/2}$ surface. The change in the potential has also caused the minimum in j'=0 opacity function to be deepened and broadened.

Another doubling of the well depth (on the S_2 surface) causes a further shift in the position of the first peak and minimum in the j'=0 opacity function of 1.6 bohr to lower impact parameter. In addition, the increased well depth gives rise to more complicated structure in the impact parameter range, b=5-8 bohr, for j'=0 and 1. This b range corresponds to the internuclear separation in the region of the attractive well for the potential. Oscillations observed in the j'=2 opacity function (figure 5) on the S_1 surface are present for S_2. Like the oscillations observed for j'= 0 and 1, the minimum and peak in j'=2 are shifted to lower impact parameters on the more attractive surface.

C. *Differential cross sections*

As seen in the above analysis, addition of the attractive well to the scattering potential leads to rich structure in the opacity functions. However, the observable in a scattering experiment is the differential cross section. Using equation 13, we calculate the DCS using the deflection and opacity functions from the trajectory calculations. In this section we examine the DCS for several j' on each surface to determine the extent that the features seen in the opacity functions are retained in the DCS.

In figures 7-9, the DCS for $j=0 \rightarrow j'=0\text{-}5$ are shown. Figure 7 shows the DCS for $j'=0$ and 1. The DCS on the REP surface for $j'=0$ decreases monotonically from the strong forward, elastically scattered, signal, to a flat signal in the backscattering region. As with the opacity functions, no structure is apparent in the low Δj DCS for the REP potential. In contrast, each of the L-J type potentials exhibits the characteristic rainbow scattering peak near 35°, 15° and 8°, for the S_2, S_1, and $S_{1/2}$ surfaces, respectively.

Each of the L-J surfaces exhibits a peak in the opacity function for $j'=0$ at low impact parameter. The peak occurs at b~2.9, 4.7 and 5.4 bohr on the S_2, S_1 and $S_{1/2}$ surfaces, respectively. The scattering angles corresponding to these impact parameters on the three surfaces are θ~120°, 60° and 30°. Inspection of the $j'=0$ differential cross sections reveals a "shoulder" in the area of each of these scattering angles on the respective surfaces. Concomitantly, there is a "dip" in the $j'=1$ DCS appearing at the same scattering angles as the shoulder in the $j'=0$ DCS on each of the surfaces. This dip in the DCS corresponds to the position of the first minimum in the $j'=1$ opacity function for each of the L-J surfaces.

Like the well known rainbow feature, the "shoulder/dip" features in the $j'=0$ and 1 DCS shift in a monotonic fashion to higher scattering angles with increasing well depth (at a fixed collision energy). This type of scattering feature, if observable experimentally,[42] may be of use in obtaining information on the potential energy surface from rotationally resolved experimental scattering data.

On surface S_2, there is an additional feature which appears in the low impact parameter region, near b=4.5 bohr, for the $j'=0$ and 1 opacity functions. These additional features manifest themselves in the $j'=0$ and 1 DCS as a dip

and bulge, respectively, near θ~70°. These additional features in the S_2 DCS can be attributed to the increased depth of the attractive well. The j'=0 opacity functions for surfaces S_1 and $S_{1/2}$ show a dip n the rainbow scattering region, while the S_2 surface shows a strong oscillatory structure. This structure also may be attributed to the increased well depth of the S_2 surface. However, much of the oscillatory structure seen in the opacity function for j'=0 and 1 on this surface is obscured by the rainbow peak, near 35°.

Figure 8 displays the DCS for j'=2 and 3 for each of the surfaces. Forward scattering, near θ=0, into j'=2 is not observed for the REP surface. The strictly repulsive nature of this surface does not support higher Δj transitions in the forward direction, which is also observed in the DCS for j'=3. The structure seen in the opacity functions for j'=2 on the S_1 and S_2 surfaces is observed as a dip in the DCS near θ=60° and 110°, respectively. For j'=3, the sharply rising DCS to the backscattering direction indicates the existence of a rotational rainbow. This peak moves to higher values of θ for each of the L-J surfaces in order of increasing well depth.

For the highly inelastic collisions leading to j'=4, only the S_1 and S_2 are capable of supporting forward scattering. It should be noted that the ordering of the rotational rainbow angle has switched. The order goes according to attractive well depth, with the rotational rainbow angle on the REP surface being largest and the angle shifting to lower angles as the well depth increases. It is also noted that the DCS for each of the surfaces are taking on the shape of that for the REP surface. This indicates that the very inelastic collisions are governed most significantly by the repulsive wall.

V. Comparison of Integral Cross Sections on a Ar+HF Surface Using Classical and Semiclassical Methods

In this section we examine integral cross sections for rotationally inelastic scattering of HF from a "Rg" atom on a prototype potential energy surface using classical and semiclassical methods. The goal is to investigate the effects of changing the atomic collision partner in the scattering dynamics. We achieve this by altering the mass of the rare gas atom in the calculations. The surface used for each mass combination is the Hutson H6 for Ar+HF(v=0).[20] In order to compare some of our findings with previous scattering experiments,[43] an initial rotational state of j=1 in these calculations was used.

In order to compare the classical calculation directly with the semiclassical method we employ an ensemble method for the classical trajectory.[44] In this method a "swarm" of trajectories is calculated simultaneously in the average potential field generated by the swarm. The equations of motion for the ensemble trajectories are given by

$$\dot{\mathbf{p}}_{r_i} = -\nabla_r V(\hat{\mathbf{R}}, \hat{\mathbf{r}}_i) \qquad ; \qquad \dot{\mathbf{r}}_i = \frac{\mathbf{p}_{r_i}}{\mu} \tag{16a}$$

$$\dot{\mathbf{P}}_R = -\left\langle \nabla_R V(\hat{\mathbf{R}}, \hat{\mathbf{r}}) \right\rangle_r \qquad ; \qquad \dot{\mathbf{R}} = \frac{\mathbf{P}_R}{M} \tag{16b}$$

where i refers to the i-th trajectory in the swarm, the average $\langle\rangle_r$ refers to the ensemble average over all trajectories in the swarm. The reduced mass of the diatom is represented by μ and M is as defined in eq.5.

As the trajectory swarm progresses, the time dependent "rotational state" of a diatom in the swarm is calculated from

$$\tilde{j}_i(t) = \left|\tilde{\mathbf{j}}_i(t)\right| = \left|\mathbf{r}_i(t) \times \mathbf{p}_i(t)\right| \hbar^{-1} \qquad (17)$$

where $\tilde{\mathbf{j}}_i$ is the continuous rotational angular momentum vector of the i-th trajectory. We bin the $\tilde{j}_i$ by round off, i.e. the i-th trajectory contributes to the j-th integer rotational state box, if $j - \frac{1}{2} \le \left|\tilde{\mathbf{j}}_i\right| < j + \frac{1}{2}$.

Another binning method, truncation,[45] which ensures that an energy-inaccessible transition has not been made, has been tested. We find that truncation greatly overestimates the j→j-1 transition at high impact parameters giving a transition probability of ~50%, where the round-off method showed a zero transition probability. Truncation showed no significant differences from rounding in the rotational state probabilities for other transitions. The weighted binning[46] method was also tested. This method greatly increased the transition probabilities for j'=j±1. This increase translates into a ~50% larger integral cross section for these transitions when employing the weighted binning method over the cross section when binning by round off. Cross sections for all other transitions are within 5% of each other.

In this paper we will employ the more widely accepted method of round off for binning the classical rotational states.[47] Binning the $\tilde{j}_i$ allows the determination of the classical time-dependent rotational state probability, $P_{j'}^{cl}(t;b)$, for the swarm, given by

$$P_{j'}^{cl}(t;b) = \frac{N_{j'}(t)}{N} \qquad (18)$$

where $N_{j'}(t)$ is the number of trajectories in a j-rotational state bin at a given time, t, and N is the total number of

trajectories in the swarm at a given impact parameter, b. The classical opacity function is given by $P_j^{ci}(t;b)$ as $t\rightarrow\infty$. The integral cross sections are calculated using eq.10.

We have carried out scattering calculations using the semiclassical coupled states and classical ensemble models for Rg+HF collisions (Rg has the mass of He, Ne, Ar or Kr) at several relative collision energies between 50 and 875 meV from a j=1 initial state. The scattering results for the different mass combinations are labelled with the corresponding Rg symbol. In figure 10a we present integral cross sections for each of the mass combinations as a function of collision energy. The classical integral cross section for $j=1\rightarrow j'=0$ transition show an essentially flat trend with both collision energy and mass combination. The exception to this trend is when He is the collision partner, these integral cross sections show a slight downward trend with increasing collision energy. In the classical model, the He results, at the higher collision energies, are approximately 10-20% lower than those for the other mass combinations.

The semiclassical cross sections show an interesting trend with collision energy. At low energy, the cross sections, σ_{10}, for the Ne, Ar, and Kr collision partners are small and increase to a maximum at E_{coll}=174 meV, then tail off slowly at high collision energy. The He cross sections show a similar decrease from a large to smaller cross section with increasing collision energy. As with the classical cross sections, the semiclassical cross sections for He as the collision partner are much smaller than those for Ne, Ar, or Kr.

None of the other integral cross sections show this type of behavior with collision energy. In figure 10b we show

the classical and semiclassical cross sections for the transition j=1→j'=2. The classical cross sections again show an essentially flat trend (with, perhaps, a slight decrease) with increasing collision energy. The semiclassical cross sections are also essentially flat with increasing collision energy, except for the decrease in the cross section where the σ_{10} goes through a maximum. The He cross section, however shows a modest increase at E_{coll}=174 meV. For the remainder of this section we will focus our attention on the 1→0 transition.

To get a better understanding of the collision dynamics leading to the cross sections we present the opacity functions for each of the mass combinations at several collision energies in figure 11. A similar structure in the opacity functions is apparent for all mass combinations and collision energies. For b<3.5 bohr, there is an initial flat region, then $P_{10}(b)$ falls off dramatically near b~4-6 bohr. The He transition probability for j=1→0 drops to essentially zero in this region. Between the impact parameters b~6-8 bohr, the 1→0 transition probability surges to a maximum near b=6.5, then falls off to zero at impact parameters, b>8.0 bohr.

In an earlier study on Ar+HF scattering[26(b)] the first dip in the opacity function was attributed to a "balance" between the attractive and repulsive parts of the potential energy surface. This balance corresponds to a "zero action" trajectory, which leaves the diatom essentially in its initial rotational state. In the impact parameter range where the 1→0 probability shows the dip, the elastic scattering probability is above 80% in most cases. Close examination of the opacity functions shows that the balance trajectory shifts to higher impact parameters with increasing collision energy.

In figure 12, typical plots of the elastic coupling potential

$$V_{11}(t) = \left\langle 1 \middle| V(\gamma; R) \middle| 1 \right\rangle \tag{19}$$

at a fixed relative collision energy, E_{coll}=173 meV, at several impact parameters are shown. We now employ these plots to help explain this shift in the opacity functions described above.

In Chapter 4 we will show that the dynamics is governed by the elastic coupling potential, $V_{jj}(t)$. For impact parameters where the potential goes positive, b<5.5 bohr, we may break up the coupling potential into components from the attractive ($V_{jj}(t)<0$) and repulsive ($V_{jj}(t)>0$) regions. In figure 12 we can see that the contribution to the dynamics due to the attractive part of the potential for b<5.5 bohr is essentially constant. However, it is clear that the contribution from the repulsive part of the potential decreases with increasing b. In figure 13 we plot the coupling potential at a single impact parameter for the Ar+HF mass combination at several collision energies. As the collision energy is increased, the trajectory accesses more of the repulsive part of the potential, thus the repulsive contribution to the dynamics at a given impact parameter is increased. Concomitantly, the attractive contribution is decreased with increasing collision energy. These changes in the coupling potential with b and E_{coll} explain the shift of the balance trajectory to higher impact parameters with increasing collision energy.

In figure 11 we observed that the largest contribution to the integral cross section comes from the impact parameter region, b~6-8 bohr. To highlight this, we present the b weighted opacity functions in figure 14. It is apparent from

figure 14 that the greatest contribution to the integral cross section does come from this impact parameter range. Since the bulge in the b-weighted opacity functions is in a region where the potential is always attractive, it should be clear that the coupling between the j=1 and j=0 states is driven by the attractive part of the potential.

In figure 15 we present the classical b-weighted opacity functions for the same mass combinations shown in figure 14. First, we note that the classical transition probability for 1→0 is ~6X smaller (note the different scales in figures 14 and 15) than in the semiclassical model. (The total transition probability in the semiclassical model must be degeneracy weighted.) Second, these plots show that the classical integral cross sections are not dominated by transitions in the impact parameter range, b~6-8 bohr, as in the semiclassical model. This is a crucial difference between the classical and semiclassical models. The quantum treatment of the diatom rotational states allows a strong coupling, in the attractive region of the potential, between the j=1 and 0 rotational states which is not seen in the classical model.

We now examine the mass effects on the integral cross sections. By changing the reduced mass of the collision system (i.e. the Rg collision partner) at a given relative collision energy, we are able to control the relative collision velocity. To investigate the effects of the relative collision velocity on the integral cross section we plot the semiclassical and classical integral cross sections for all mass combinations vs collision velocity in figure 16.

The classical integral cross sections show a linearly decreasing trend with increasing collision velocity. The semiclassical cross sections, for all mass combinations, lie along a single curve as a function of collision velocity. The peak in the semiclassical integral cross sections comes at a

collision velocity of ~1.40km/s. Each mass combination peaks near this collision velocity, except He. The calculated collision energy to achieve the 1.40km/s collision velocity for He+HF is 33.85 meV. At this low collision energy the trajectories show complex behavior, i.e. trapping and orbiting. The simple approximations used in this study calculate the cross sections break down under these conditions.

To explore the decrease in the integral cross section with collision velocity we recall that the integral cross section is dominated by the impact parameter range, b~6-8 bohr. In figure 14 it is seen that as the collision energy (velocity) is increased, the contribution to the cross section from this region is decreased. In figure 17 we plot the coupling potential at an impact parameter of b=7.0 bohr at several collision velocities. With increasing collision velocity the interaction time is correspondingly decreased, reducing the overall action for the trajectory. As we reduce the collision velocity below 1.40km/s, the probability for T⇔R transfer decreases and the integral cross section decreases.

VI. Conclusions

In this chapter we have attempted to correlate specific features in the observable differential cross sections for rotationally inelastic scattering to the potential energy surface. We have seen that in addition to the "impact parameter rainbow" and the rotational rainbow, the potential surfaces studied here exhibit another type of feature. This feature appears as a shoulder in the elastic DCS and a dip in the slightly inelastic (j'=j+1) DCS. Specifically for the system studied, a "shoulder/dip" feature was observed in the j'=0 and j'=1 differential cross sections. This feature shifted in a "rainbow-like" manner to higher scattering

angles as the attractive well depth on the potential surface was increased. Additional structure in the elastic and slightly inelastic opacity functions was observed on the surface having the deepest attractive well depth.

In addition we have presented integral cross sections for "Rg"+HF ("Rg" = He, Ne, Ar, Kr) rotationally inelastic scattering using semiclassical and classical trajectory calculations. The classical and semiclassical cross sections are found to be qualitatively different as a function of collision velocity. The classical cross sections decrease linearly with increasing collision velocity. The semiclassical integral cross sections peak at a velocity near 1.40 km/s for each mass combination. The differences between the classical and semiclassical results are due to a strong coupling between the j=0 and 1 states at impact parameters corresponding to the attractive minimum, i.e. b=6.0-8.0 bohr, in the semiclassical model.

References

1. (a) J. C. Light, *Atom-Molecule Collision Theory*, ed. R. B. Bernstein, Plenum, NY, (1979), Chap. 6;
   (b) D. Secrest, *ibid.*, Chap. 8;
   (c) D. J. Kouri, *ibid.*, Chap. 9;
   (d) R. Schinke and J. M. Bowman, *Molecular Collision Dynamics*", ed. J. M. Bowman Springer, Berlin, (1982);
   (e) U. Buck, in *Atomic and Molecular Beam Methods, vol. 1*, ed. G. Scoles Oxford U. Press, Oxford, (1988) Chap. 18, 21;
   (f) P. Dagdigian, *ibid.*, Chap. 23

2. (a) P. L. Jones, U. Hefter, A. Mattheus, J. Witt, K. Bergmann, W. Müller, W. Meyer and R. Schinke, Phys. Rev. B, **26**, 1283 (1982);
   (b) P. L. Jones, E. Gottwald, U. Hefter and K. Bermann, J. Chem. Phys., **78**, 3838 (1983);
   (c) U. Buck, H. Meyer and R. J. LeRoy, J. Chem. Phys., **80**, 5589 (1984);
   (d) M. Keil, J. T. Slankas and A. Kuppermann, J. Chem. Phys., **70**, 541 (1979)

3. P.F. Vohralik, R.E. Miller and R.O. Watts, J. Chem. Phys., **90**, 2182 (1989)

4. (a) W. H. Miller, J. Chem. Phys., **53**, 1949 (1970);
   (b) R. A. Marcus, J. Chem. Phys., **54**, 3965 (1971);
   (c) W. Schepper, U. Ross and D. Beck, Z. Phys. A, **290**, 131 (1979);
   (d) D. Beck, U. Ross and W. Schepper, Phys. Rev. A, **19**, 2173 (1979);
   (e) ref. 1 (a), (b), (c), (d)

5. (a) J. Andres, U. Buck, F. Huisken, J. Schleusener and F. Torello, J. Chem. Phys., **73**, 5629 (1980);
   (b) R. Schinke, W. Müller, W. Meyer and P. McGuire, J. Chem. Phys., **74**, 3916 (1981);
   (c) R. Schinke, W. Müller and W. Meyer, J. Chem. Phys., **76**, 895 (1982)

6. (a) K. Bergmann, R. Engelhardt, U. Hefter and J. Witt, J. Chem. Phys., **71**, 2726 (1979);
   (b) K. Bergmann, U. Hefter and J. Witt, J. Chem. Phys., **72**, 4777 (1980);
   (c) K. Bergmann, U. Hefter, A. Mattheus and J. Witt, Chem. Phys. Lett., **78**, 61 (1981);
   (d) U. Hefter, P. L. Jones, A. Mattheus, J. Witt, K. Bergmann and R. Schinke, Phys. Rev. Lett., **46**, 915 (1981)

7. (a) U. Buck, F. Huisken, J. Schleusener and J. Schäfer, J. Chem. Phys., **72**, 1512 (1980)
   (b) U. Buck, Faraday Discuss. Chem. Soc., **73**, 187 (19482)

8. M. Keil, J. T. Slankas and A. Kuppermann, J. Chem. Phys., **70**, 541 (1979)

9. (a) M. Faubel, K. H. Kohl and J. P. Toennies, J. Chem. Phys., **73**, 2506 (1980);
(b) M. Faubel, K. H. Kohl, J. P. Toennies, K. T. Tang and Y. Y. Yung, Faraday. Discuss., **73**, 205 (1982);
(c) S. D. Jons, J. E. Shirley, M. T. Vonk, C. F. Giese and W. R. Gentry, J. Chem. Phys. (1992)

10. (a) D. M. Silver, J. Chem. Phys., **72**, 6445 (1980);
(b) E. F. Jendrek and M. H. Alexander, *ibid.*, 6452;
(c) P. J. Dagdigian and B. E. Wilcomb, *ibid.*, 6462

11. (a) D. L. Thompson, J. Chem. Phys., **67**, 5224 (1977);
(b) H. J. Loesch, Adv. Chem. Phys., **52**, 421 (1980);
(c) R. Schinke, H. J. Korsch and D. Poppe, J. Chem. Phys., **77**, 6005 (1982);
(d) R. Schinke,and J. M. Bowman, in *Molecular Collision Dynamics*, ed. J. M. Bowman, Springer, Berlin, (1982), Chap. 4

12. (a) F. A. Morse, R. B. Bernstein and H. U. Hostettler, J. Chem. Phys., **36**, 1947 (1962);
(b) U. Buck, M. Kick and H. Pauly, J. Chem. Phys., **56**, 4925 (1974);
(c) R. T Pack, J. J. Valentini, C. H. Becker and Y. T. Lee, J. Chem. Phys., **77**, 5475 (1982);
(d) R. T Pack, E. Piper, G. A. Pfeffer and J. P. Toennies, J. Chem. Phys., **80**, 4940 (1984);
(e) A. G. Suits, L. S. Bontuyan, P. L. Houston and B. J. Whitaker, J. Chem. Phys., **96**, 8618 (1992)

13. (a) G. A. Parker and R. T Pack, J. Chem. Phys., **68**, 1585 (1978);
(b) R. T Pack, Chem. Phys. Lett., **55**, 197 (1978)

14. J. M. Hutson, Ann. Rev. Phys. Chem., **41**, 123 (1990)

15. (a) T. A. Dixon, C. H. Joyner, F. A. Baiocchi and W. Klemperer, J. Chem. Phys., **74**, 6539 (1981);
(b) M. R. Keenan, L. W. Buxton, E. J. Campell, A. C. Legon and W. H. Flygare, J. Chem. Phys., **74**, 2133 (1981)

16. (a) R. M. van Aalst, J. A. Schuurman and J. Elsken, Chem. Phys. Lett., **35**, 558 (1975);
(b) B. Schramm and U. Leuchs, Ber. Bunsenges. Phys. Chem., **83**, 847 (1979);
(c) J. M. Hutson and B. J. Howard, Mol. Phys., **45**, 769 (1982)

17. (a) C. Douketis, J. M. Hutson, B. J. Orr and G. Scoles, Mol. Phys., **52**, 763 (1984);

(b) C. M. Lovejoy, M. D. Schuder and D. J. Nesbitt, Chem. Phys. Lett., **127**, 374 (1986);
(c) G. T. Fraser and A. S. Pine, J. Chem. Phys., **85**, 2502 (1986);
(d) C. M. Lovejoy, M. D. Schuder and D. J. Nesbitt, J. Chem. Phys., **85**, 4890 (1986);
(e) Z. S. Huang, K. W. Jucks and R. E. Miller, J. Chem. Phys., **85**, 6905 (1986);
(f) D. J. Nesbitt, M. S. Child and D. C. Clary, J. Chem. Phys., **90**, 4855 (1989)

18. J. M. Hutson and B. J. Howard, Mol. Phys., **45**, 791 (1982)

19. (a) C. M. Lovejoy and D. J. Nesbitt, J. Chem. Phys., **91**, 2790 (1989);
(b) M. A. Dvorak, S. W. Reeve, W. A. Burns, A. Grushow and K. R. Leopold, Chem. Phys. Lett., **185**, 399 (1991);
(c) C. M. Lovejoy, J. M. Hutson and D. J. Nesbitt, J. Chem. Phys., **97**, 8009 (1992);
(d) J. T. Farrell, Jr., O. Sneh, A. Wright, A. E. Knight and D. J. Nesbitt, J. Chem. Phys., **97**, 7967 (1992)

20. J. M. Hutson, J. Chem. Phys., **96**, 6752, (1992)

21. (a) J. Andres, U. Buck, F. Huisken, J. Schleusener and F. Torello, J. Chem. Phys., **73**, 1512 (1980);
(b) U. Buck, H. Meyer and R. J. LeRoy, J. Chem. Phys., **80**, 5589 (1984)

22. U. Buck, Comments At. Mol. Phys., **17**, 541 (1979)

23. (a) G. Starkshall and R. G. Gordon, J. Chem. Phys., **54**, 663 (1970);
(b) J. M. Farrar and Y. T. Lee, Chem. Phys. Lett., **26**, 428 (1974);
(c) C. H. Becker, P. W. Tiedemann. J. J. Valentini and Y. T. Lee, J. Chem. Phys., **71**, 481 (1979);
(d) J. A. Barnes, M. Keil, R. E. Kutina and J. C. Polanyi, J. Chem. Phys., **76**, 913 (1982)

24. D. L. Thompson, J. Chem. Phys., **76**, 5947 (1982);
(b) C. V. Boughton, R. E. Miller, P. F. Vohralik and R. O. Watts, Mol. Phys., **58**, 827 (1986);
(c) P. F. Vohralik, R. E. Miller and R. O. Watts, J. Chem. Phys., **90**, 2182 (1989)

25. L. J. Rawluk, Y. B. Fan, Y. Apelblat and M. Keil, J. Chem. Phys, **94**, 4205 (1991)

26. (a) L. J. Rawluk, M. Keil, M. H. Alexander, H. R. Mayne and J. J. C. Barrett, Chem. Phys. Lett., **202**, 291 (1993);
(b) J. J. C. Barrett, H. R. Mayne and M. Keil, J. Chem. Phys., (in press, 1994);
(c) J. J. C. Barrett, H. R. Mayne, M. Keil and L. J. Rawluk, Can. J. Chem., (in press, 1994)

27. see references 6, 7, 8, 9, and 10

28. H. R. Mayne and M. Keil, J. Phys. Chem., **88**, 883 (1984)

29. R. Düren, R. K. B. Helbing and S. Miloševič, Chem. Phys., **151**, 287 (1991)

30. M. S. Child, *Molecular Collision Theory*, Academic Press, London, (1974), pp. 141-148

31. A. E. DePristo, J. Chem. Phys., **78**, 1237 (1983)

32. D. Bohm, *Quantum Theory*, Dover Publication, Inc. New York, 1989 Chap. 18, pp. 407-409

33. R. T Pack, J. Chem. Phys., **60**, 633 (1974)

34. G. D. Billing, Comp. Phys. Rep., **1**, 237 (1984)

35. P. McGuire and D. J. Kouri, J. Chem. Phys., **60**, 2488 (1974)

36. R. D. Levine and R. B. Bernstein, *Molecular Reaction Dynamics and Chemical Reactivity*, Oxford U. Press, (1987) pp.68-70

37. *ibid.*, p.69

38. M. Abramowitz and I. A. Stegun, *Handbook of Mathematical Functions with Formulas, Graphs and Mathematical Tables*, NBS, Applied Mathematics Series, #55, (1964), p. 878

39. *ibid.*, p.882

40. K. W. Ford and J. A. Wheeler, Ann. Phys., **7**, 259 (1959)

41. M. A. D. Fluendy and K. P. Lawley, *Chemical Applications of Molecular Beams*, Chapman and Hall, London (1973), p.24

42. A shoulder in the j'=0 differential cross section has been observed in a rotationally resolved inelastic scattering experiment for the Ar+HF system (ref. 25).

43. J. A. Barnes, M. Keil, R. E. Kutina and J. C. Polanyi, J. Chem. Phys., **72**, 6306 (1980);
(b) reference 23 (d)

44. K. Haug and H. Metiu, J. Chem. Phys., **97**, 4781 (1992)

45. L. M. Raff and D. L. Thompson, *Chemical Reaction Dynamics*, ed. M. Baer, CRC Press, Boca Raton, FL (1985), p.41

46. (a) P. Brumer, Chem. Phys. Lett., **28**, 345, (1974);
(b) A. Metropoulos and D. M. Silver, J. Chem. Phys., **81**, 1682 (1984)

47. A. F. Wagner and A. C. Wahl, J. Chem. Phys., **69**, 3756 (1978)

Table 1. Position of $V(R,\gamma=0)=135$ meV for each of the model potential energy surfaces.

	R [bohr]
Surface 1	5.33
Surface 2	5.52
Surface 3	5.16
Repulsive surface	5.35

Table 2. Lennard-Jones parameters for the potential surfaces employed in this calculation. The σ_λ for the S2 surface are shifted -0.1Å; σ_λ for the S2 surface are shifted +0.1Å from those given in the first part of the table. Potential parameters for the R14 surface are given in the second part of the table.

λ	σ_λ [Å]	S_1 ε_λ [meV]	S_2 ε_λ [meV]	$S_{1/2}$ ε_λ [meV]
0	3.12	17.6	36.2	8.81
1	3.10	3.73	7.46	1.86
2	2.95	3.93	7.86	1.96
3	3.20	1.31	2.62	0.655
4	3.12	0.843	1.696	0.424
5	3.01	0.0268	0.0536	0.0134

λ	σ_λ [Å]	REP ε_λ [meV]
0	2.85	17.6
1	2.85	3.73
2	2.85	3.93
3	2.85	1.31
4	2.85	0.843
5	2.85	0.0268

Table 3. Comparison of rainbow angles calculated from equation 15, using ε_0 as the well depth and the collision energy of 135 meV, to the trajectory result on each potential surface.

ε_0 [meV]	θ_r [°] eq.15	θ_r [°] trajectory
8.81	7.48	6.94
17.6	14.9	14.7
36.2	30.8	35.9

Table 4. Derivatives of the potential with respect to R at $\gamma=0$ at the energy $V(R,0)=135$ meV. Also given is the value of R at this point.

Surface	R [bohr]	$-(\partial V/\partial R)_{\gamma=0}$
S_1	5.33	529.2
S_2	5.33	656.2
$S_{1/2}$	5.33	428.4
REP	5.35	363.0

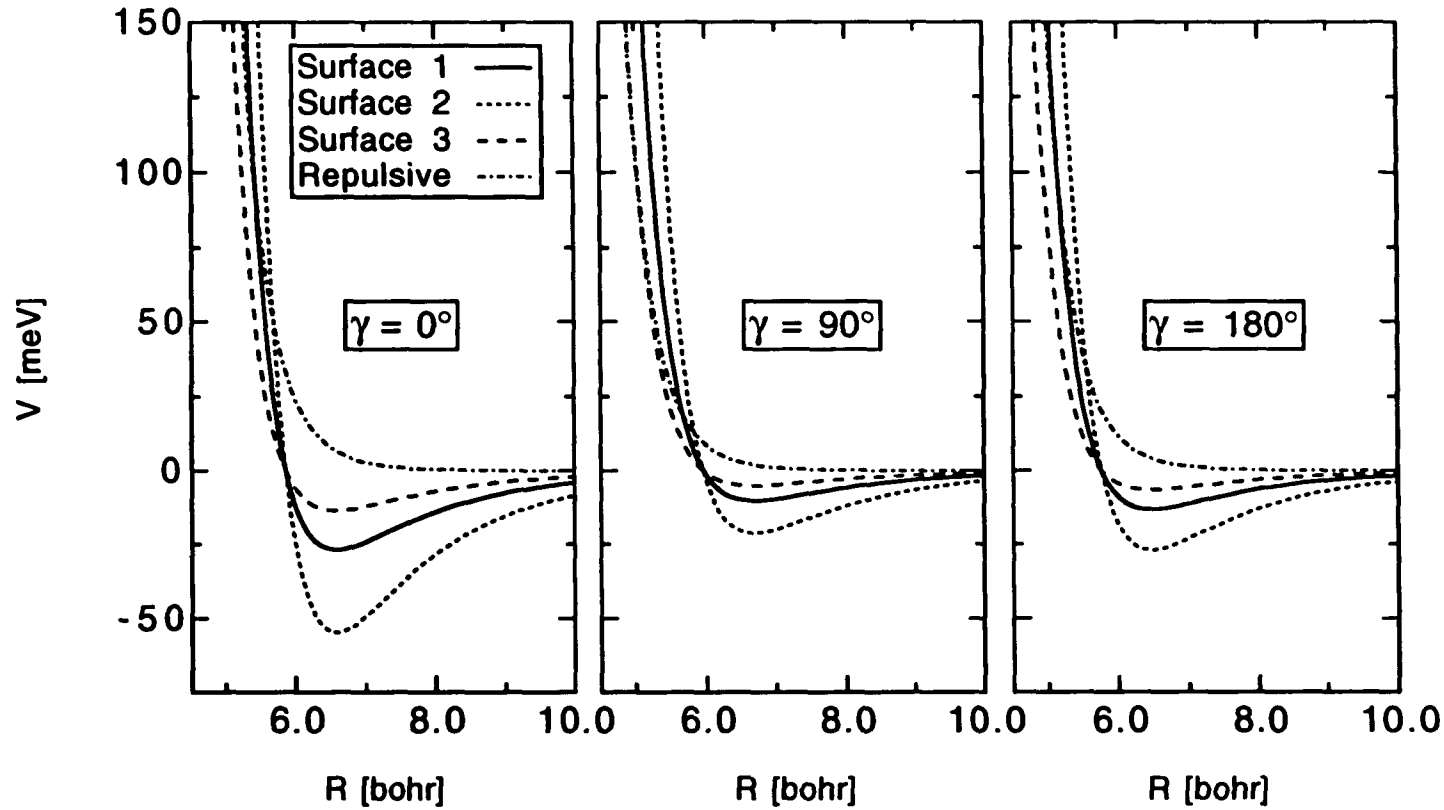

Figure 1. Lennard-Jones and repulsive potential energy functions as a function of R at fixed gamma.

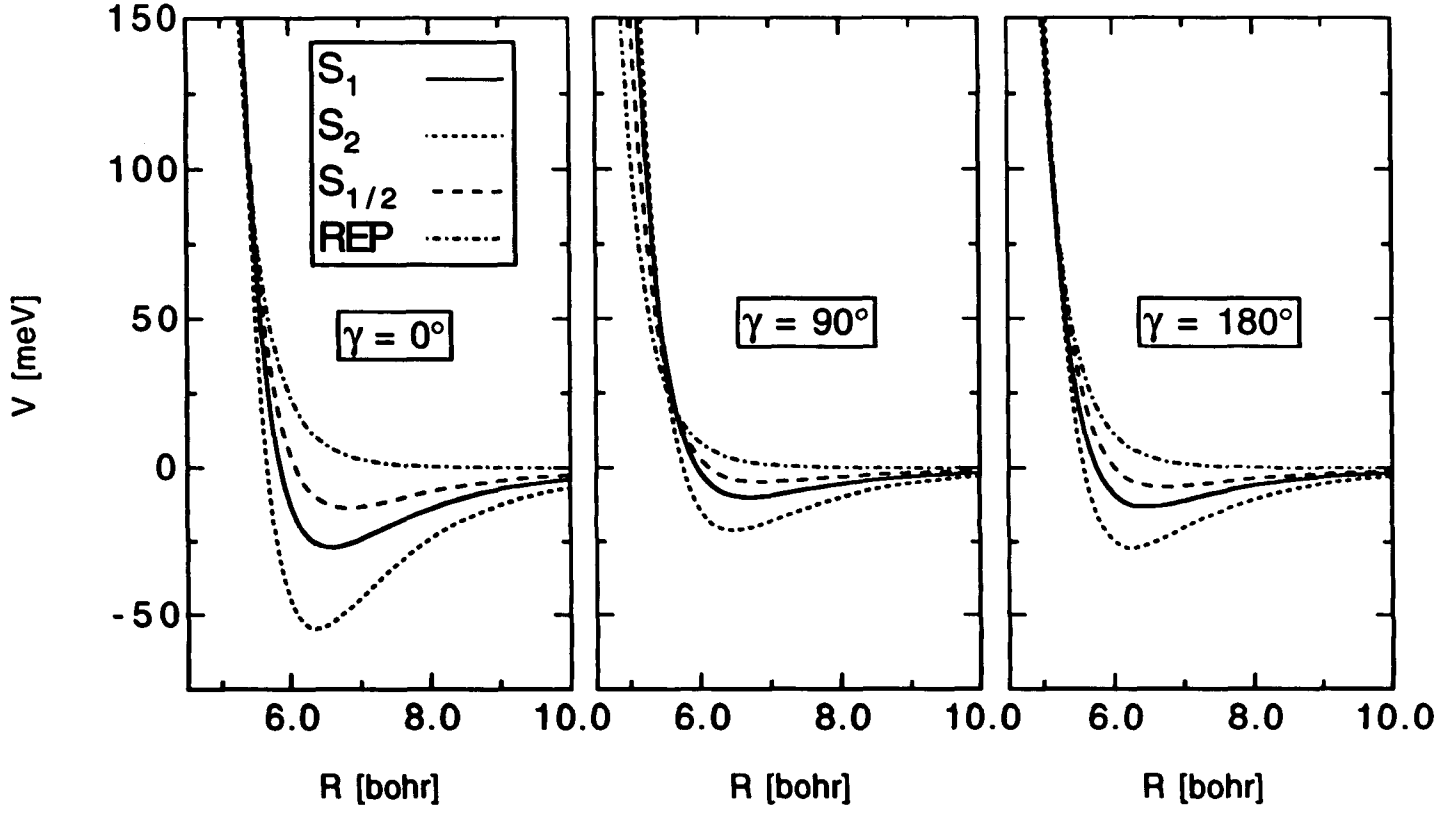

Figure 2. Lennard-Jones and REP surfaces as a function of R at fixed gamma values. S_2 and $S_{1/2}$ are shifted as described in text.

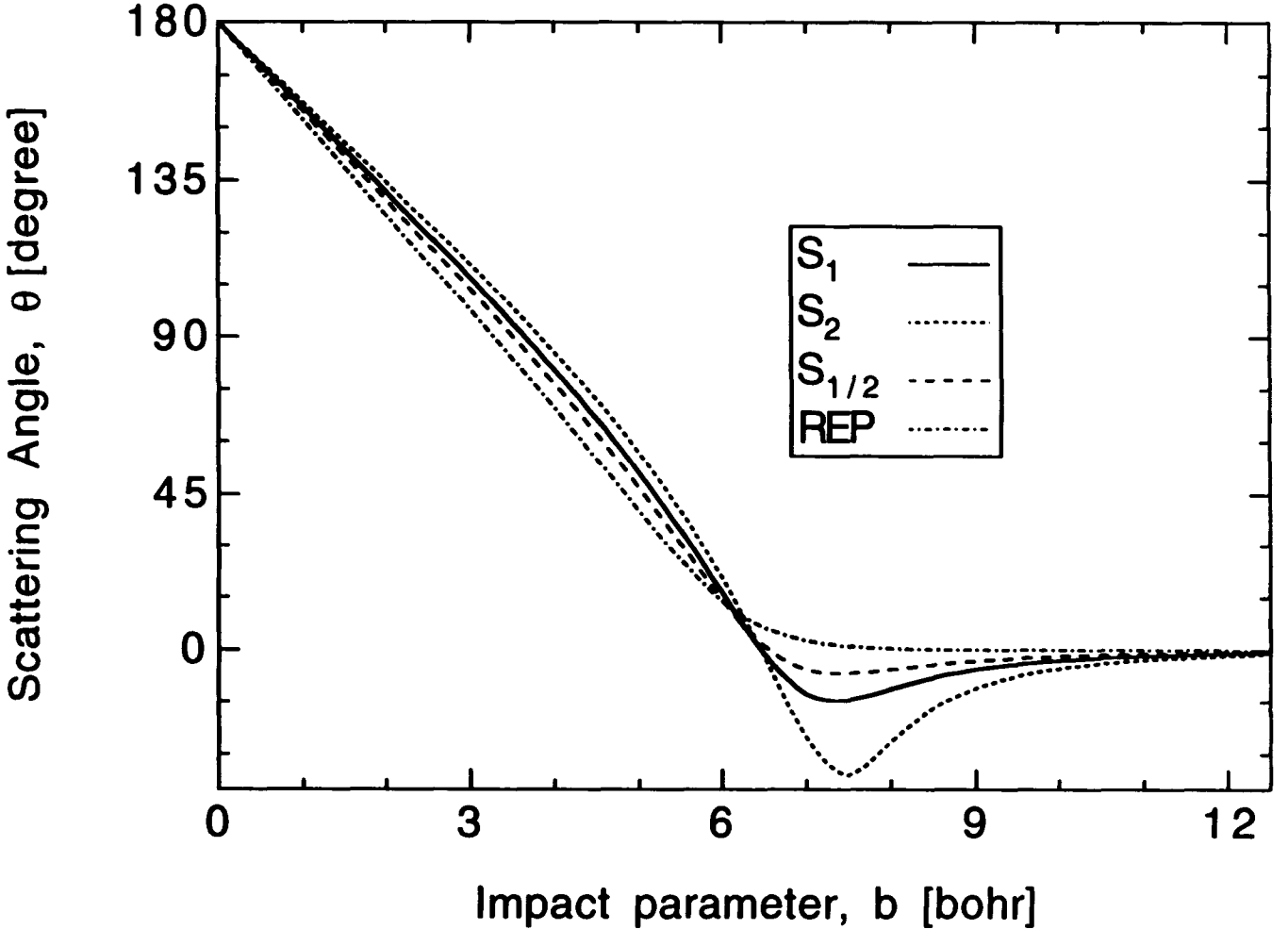

Figure 3. Comparison of deflection functions on each potential energy suface.

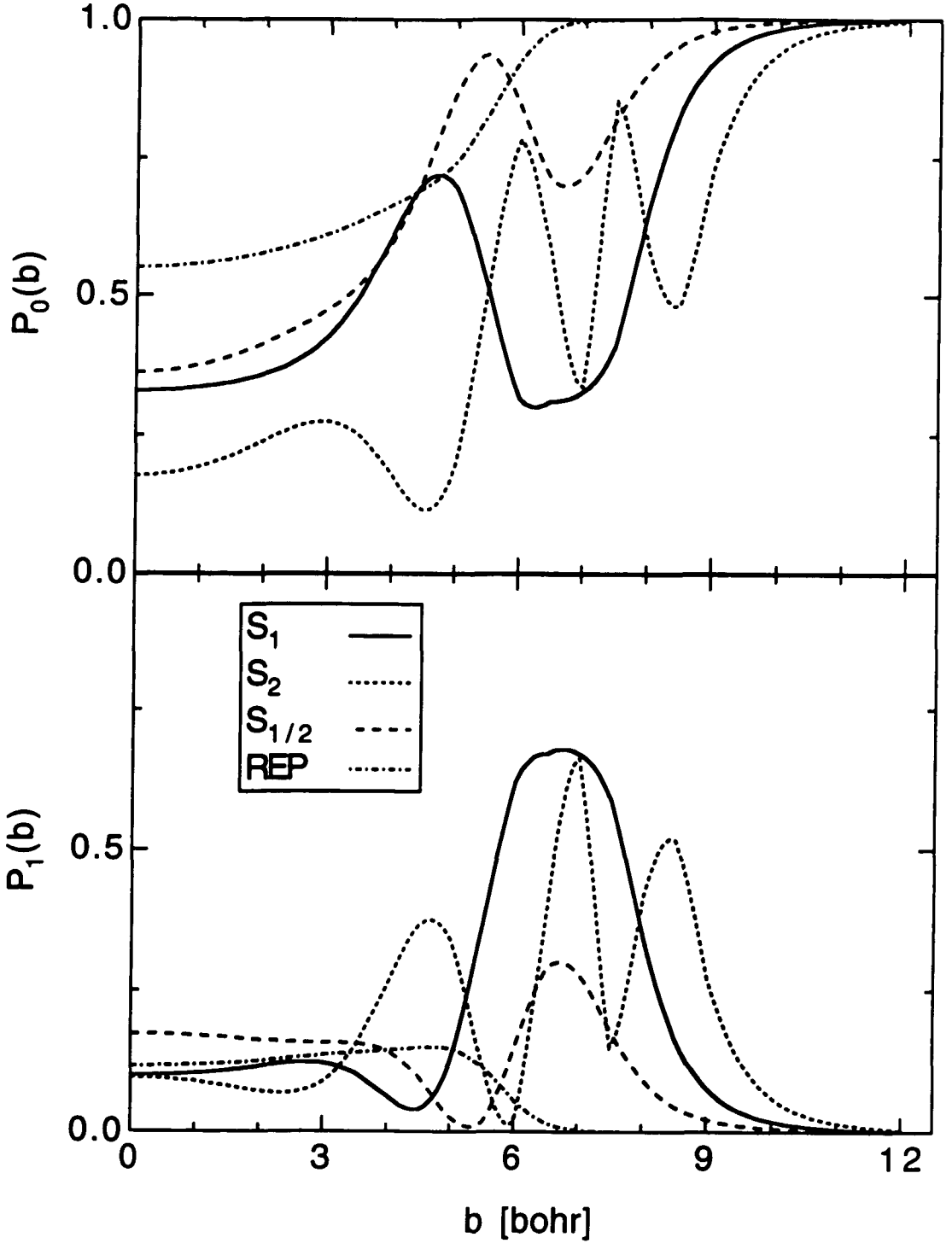

Figure 4. Opacity functions for j'=0 and j'=1 on each potential surface.

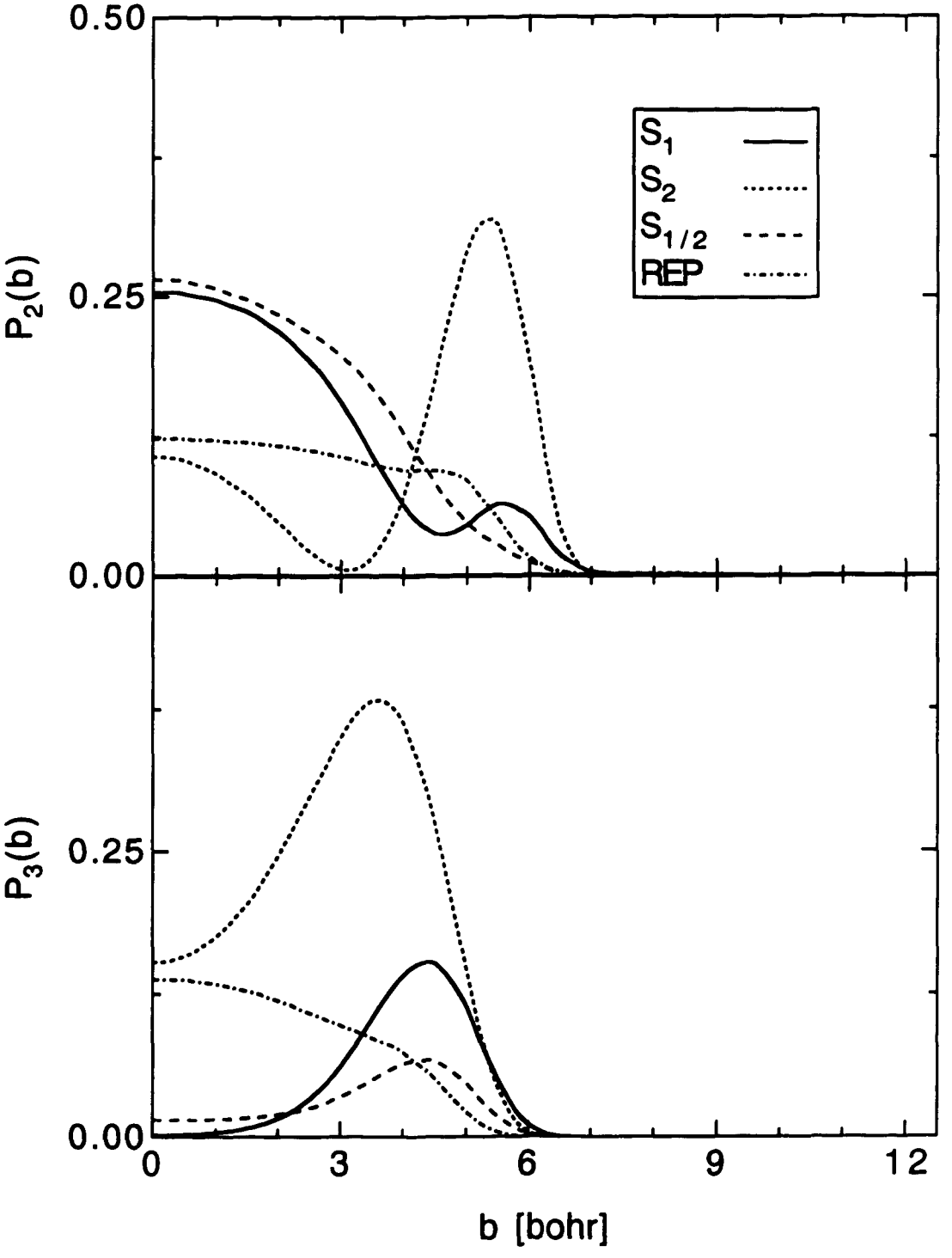

Figure 5. Opacity functions for j'=2 and j'=3 on each potential surface.

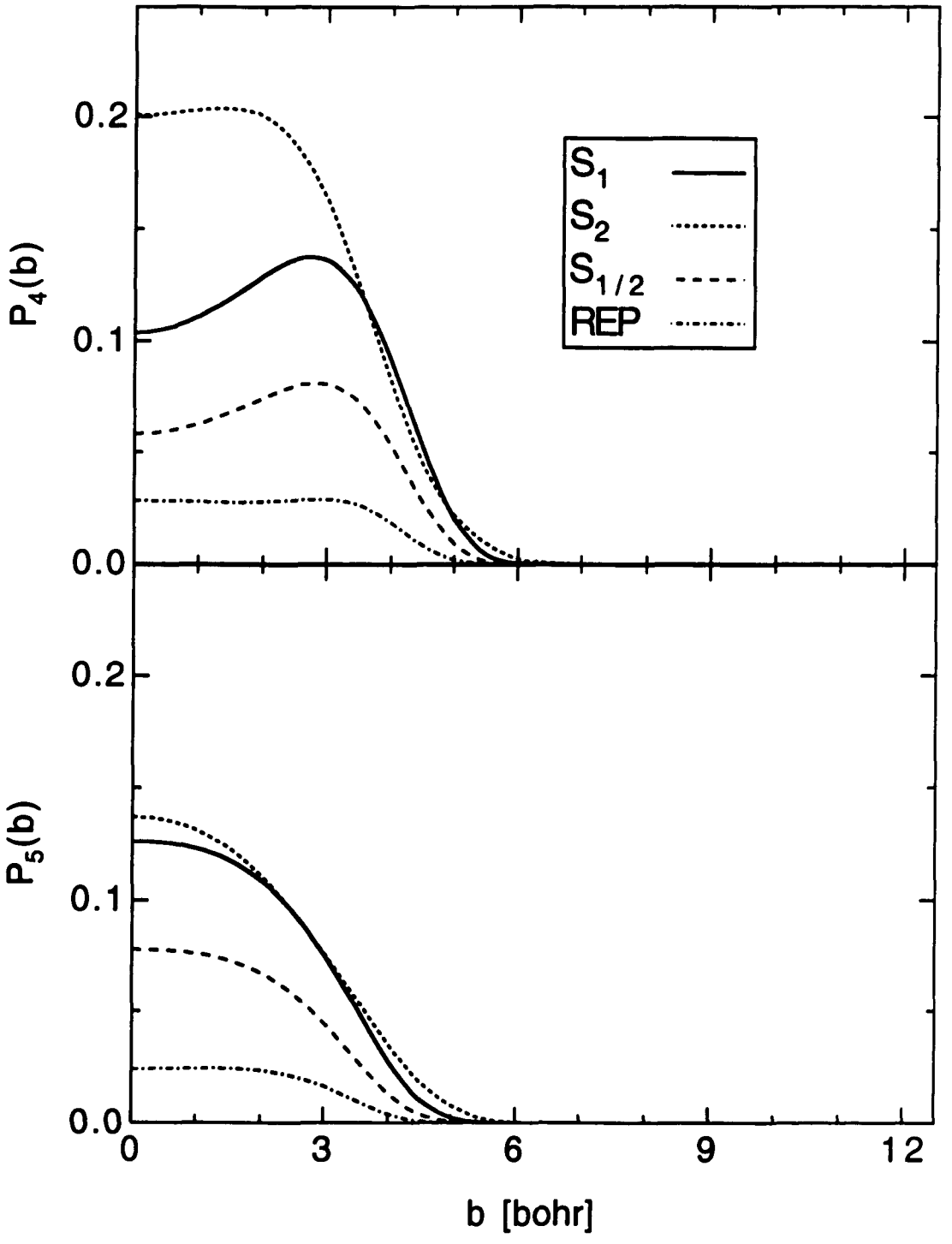

Figure 6. Opacity functions for j'=4 and j'=5 on each potential surface.

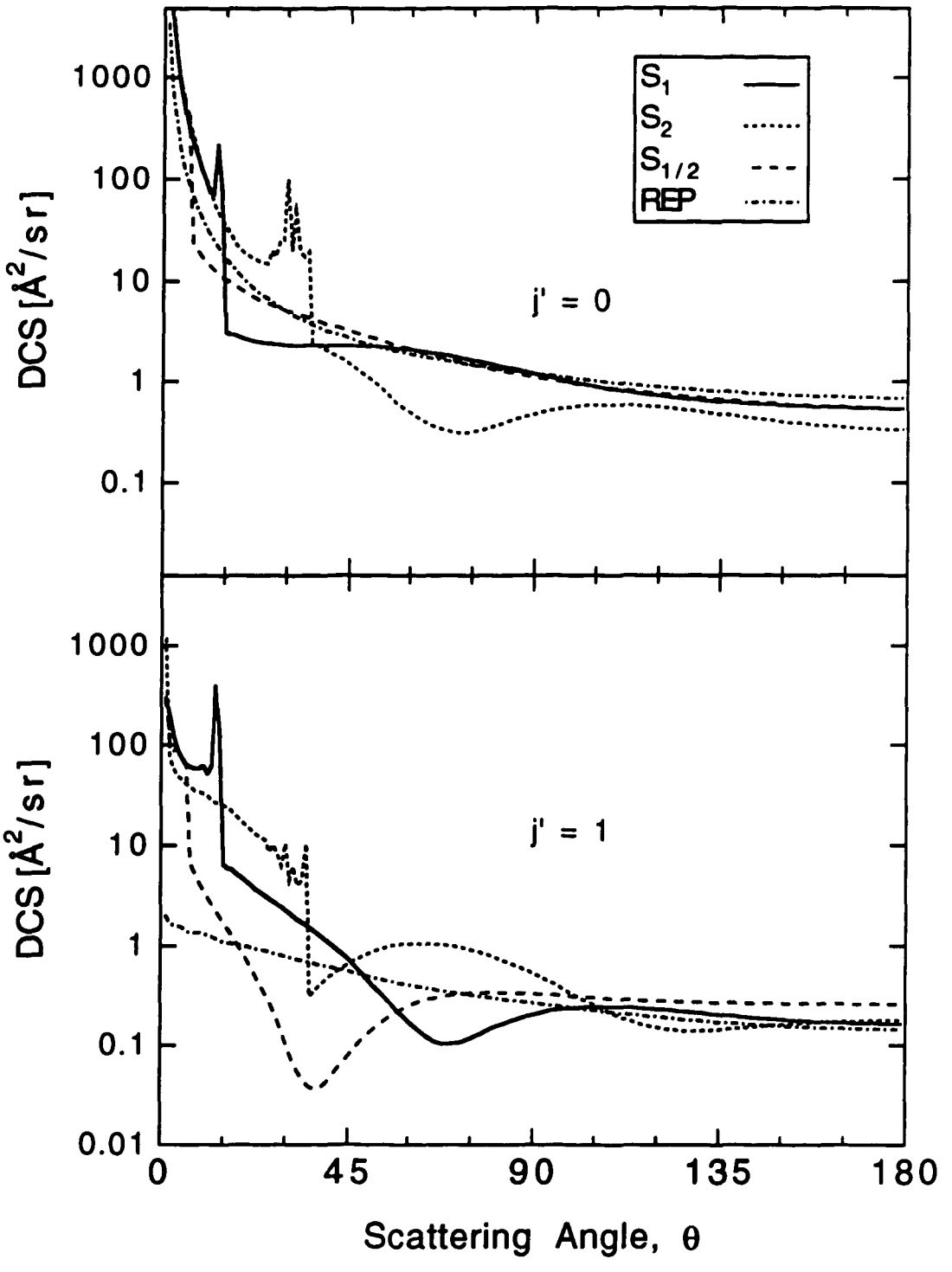

Figure 7. Differential cross sections for j'=0 and j'=1 on each surface.

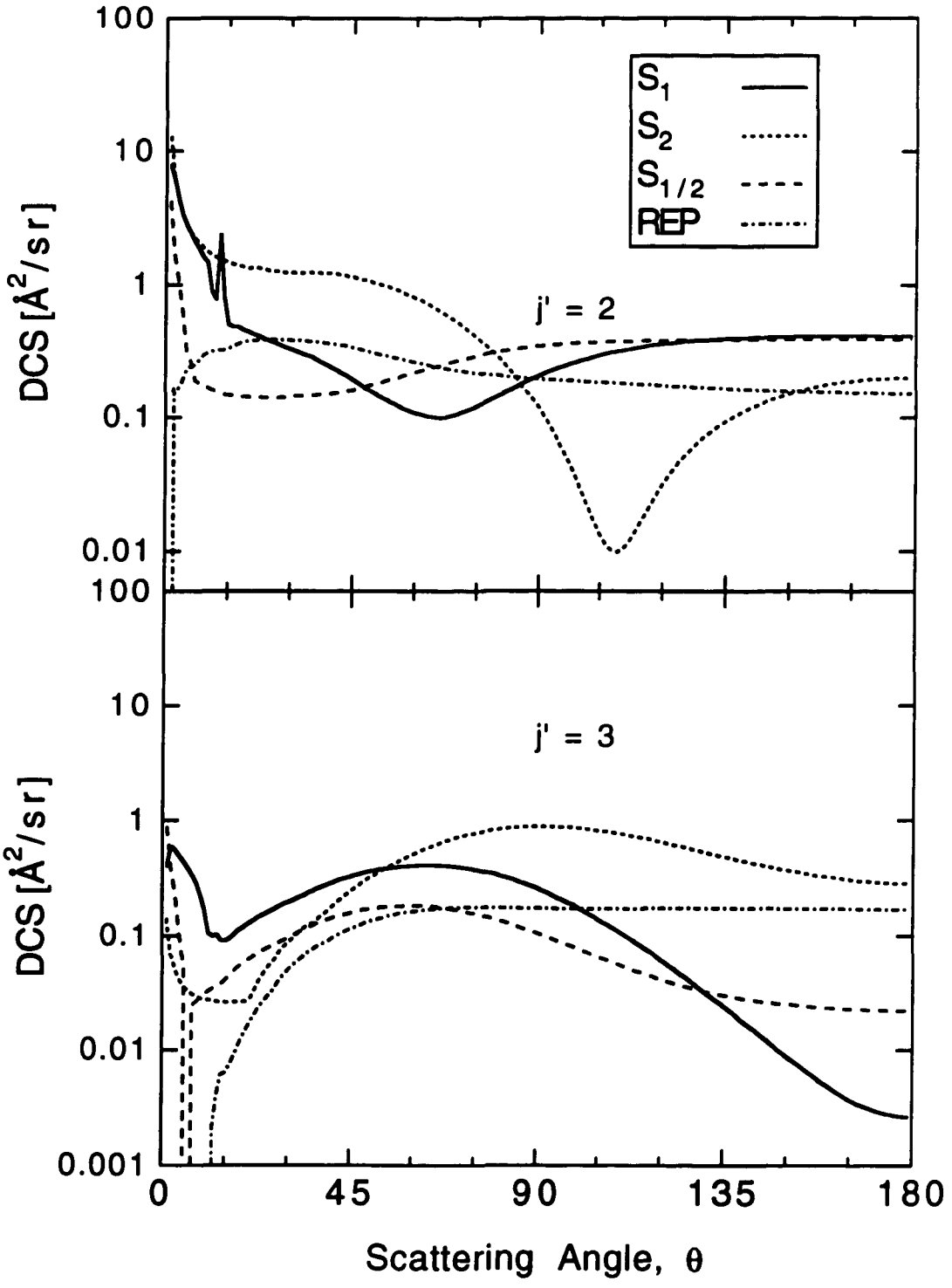

Figure 8. Differential cross sections for j'=2 and j'=3 on each surface.

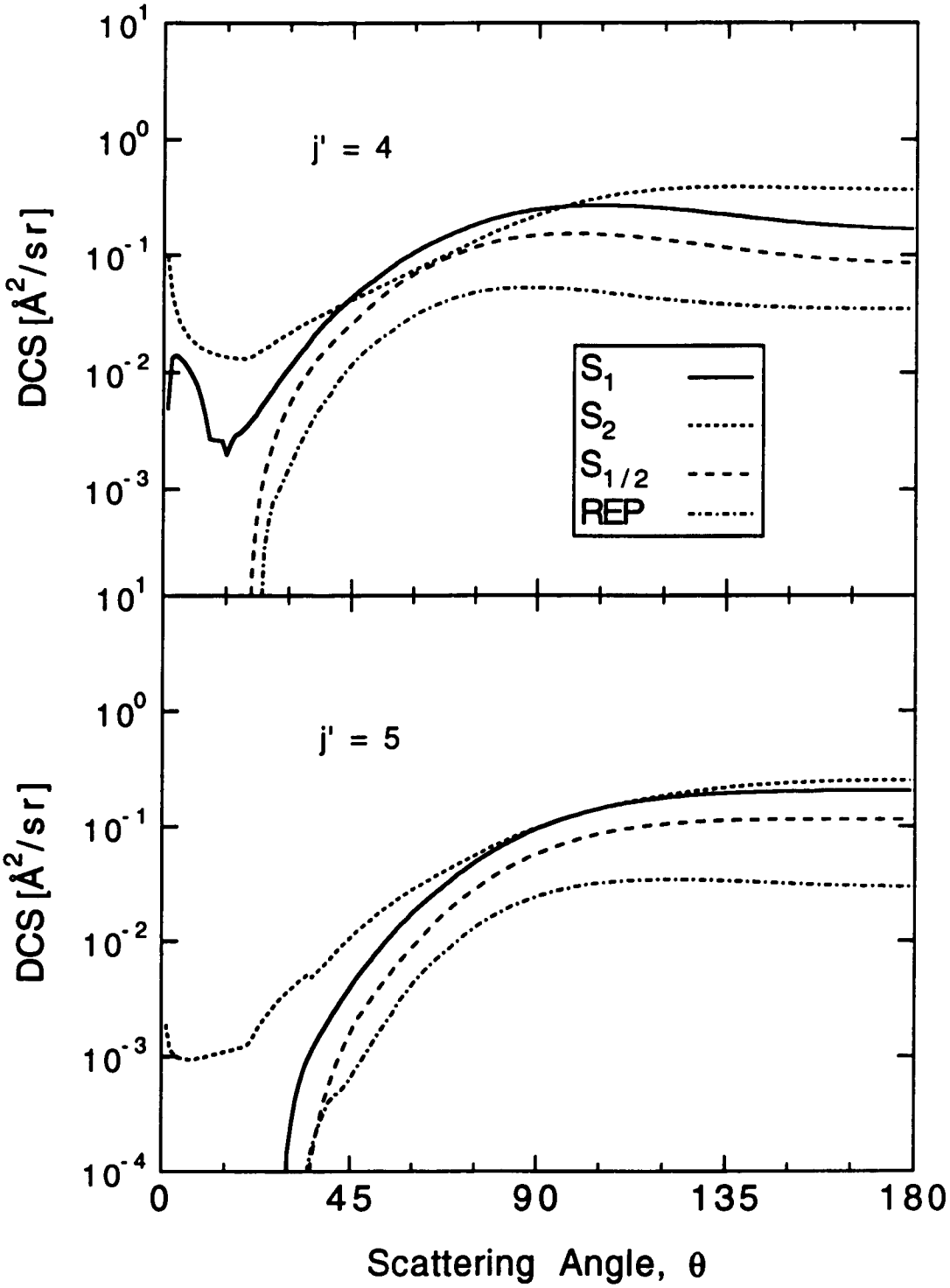

Figure 9. Differential cross sections for j'=4 and j'=5 on each surface.

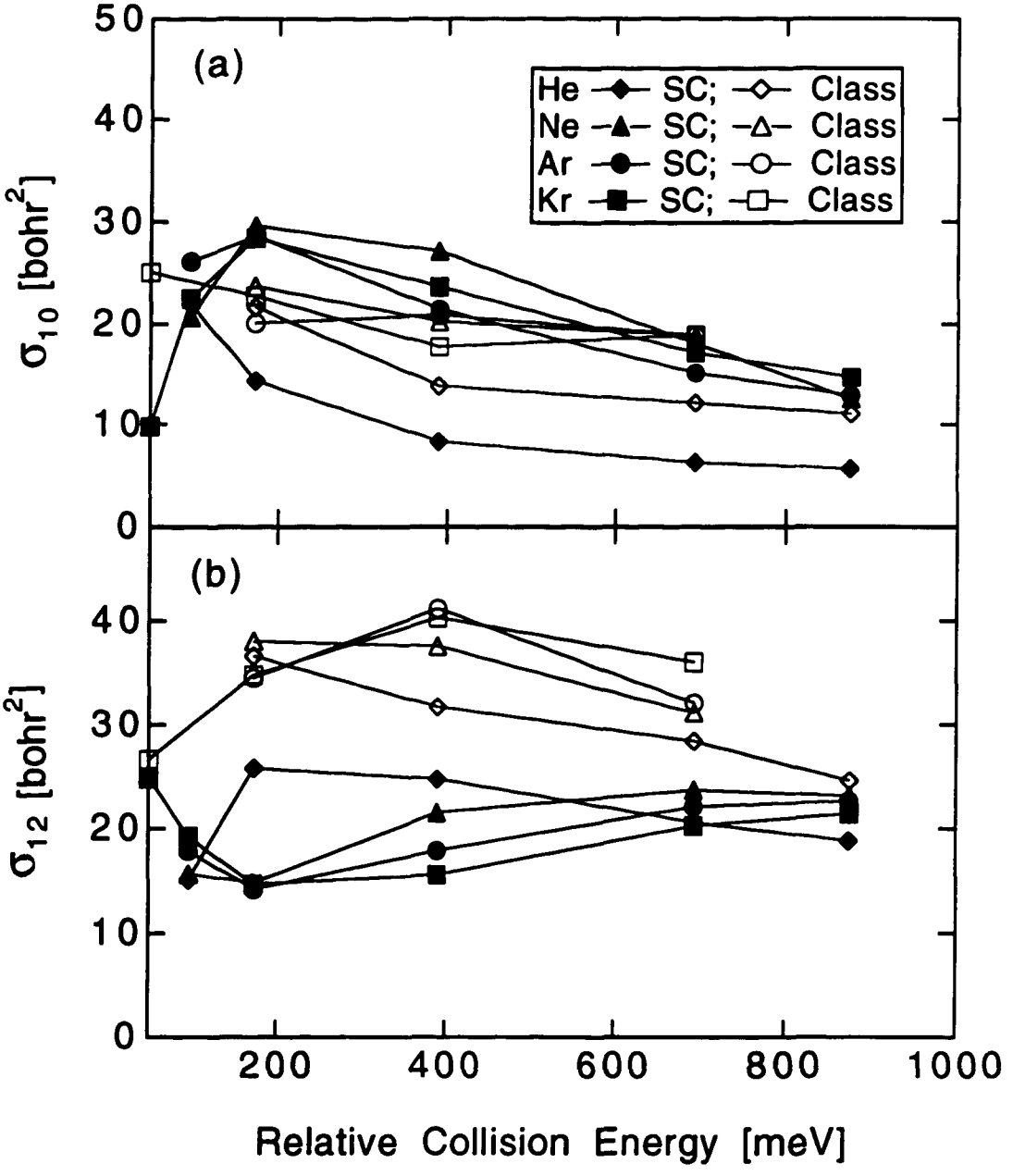

Figure 10. Semiclassical and classical integral cross sections as a function of collision energy and mass combination.

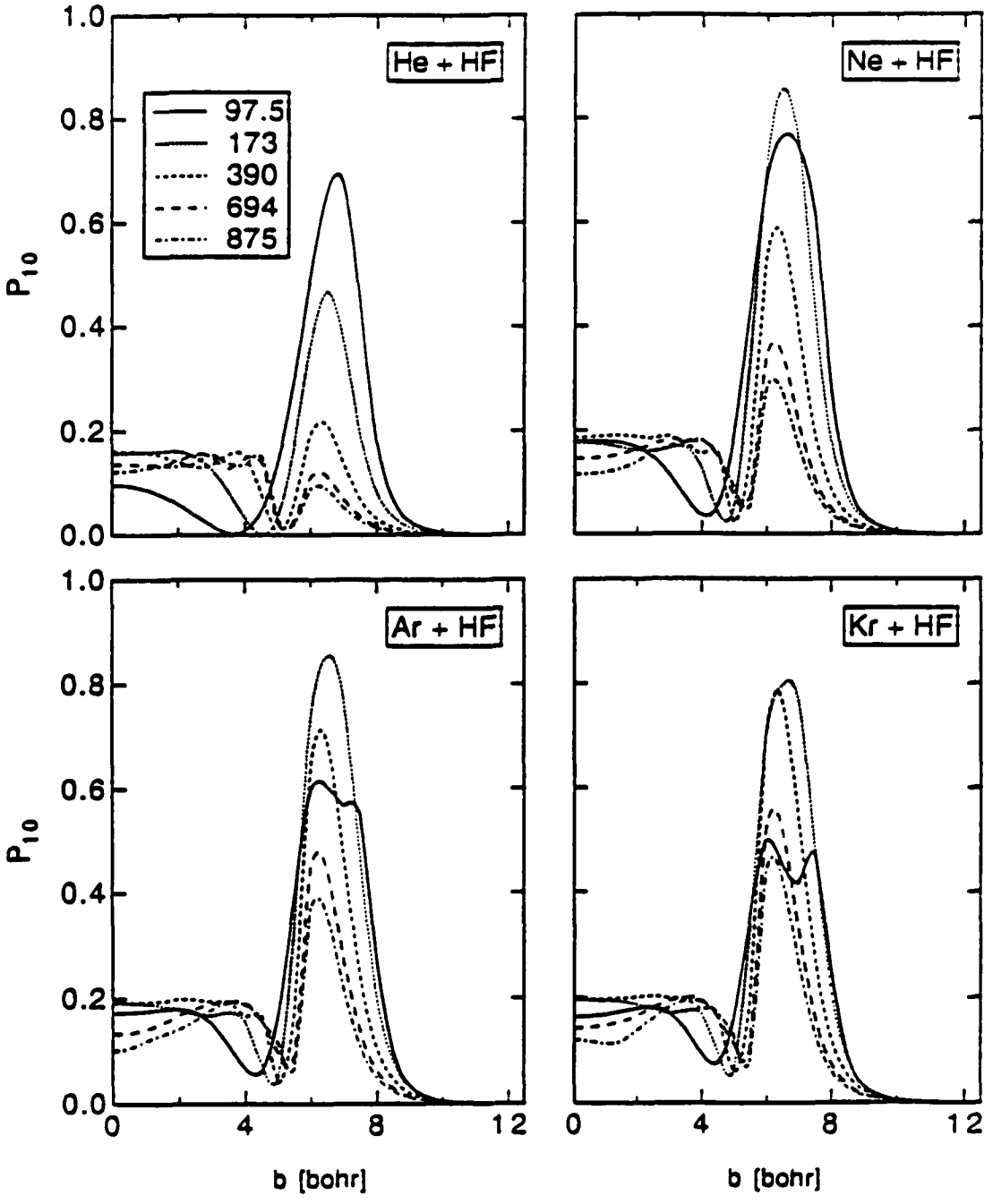

Figure 11. Semiclassical opacity functions for several mass combinations and collision energies. Collision energies in meV.

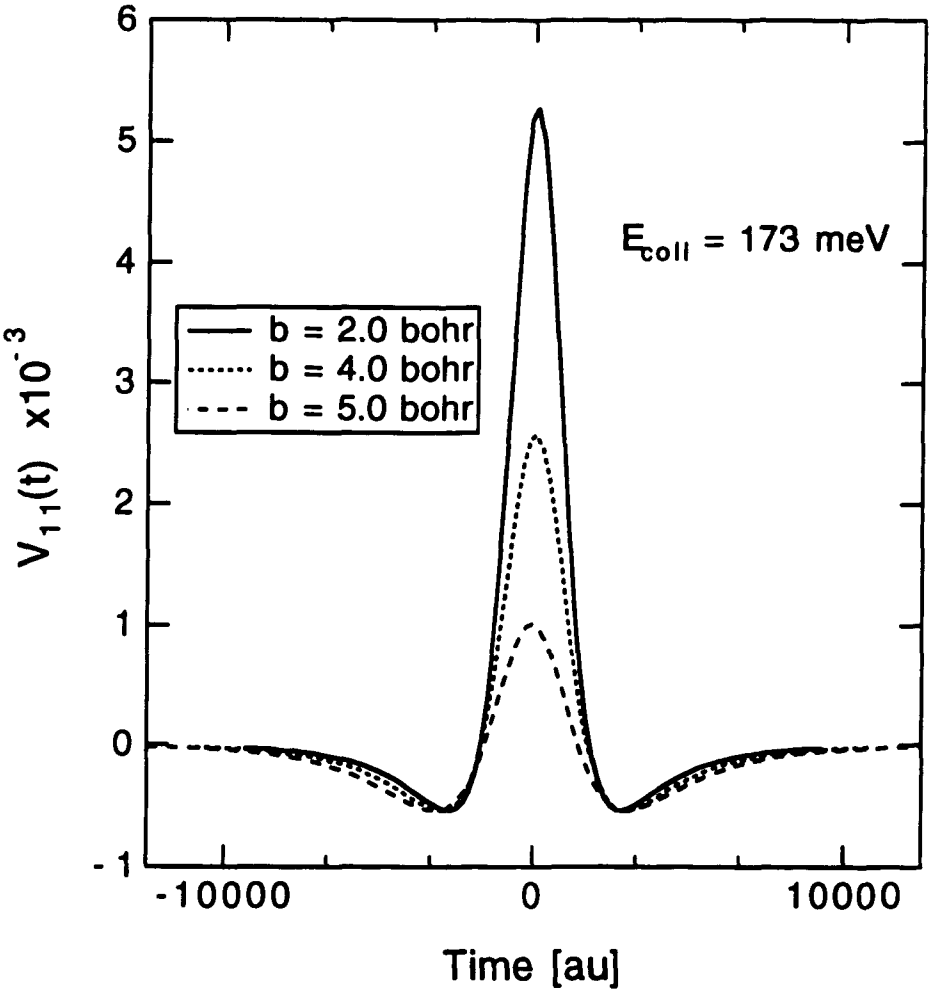

Figure 12. Elastic coupling potential at a single collision energy for several values of the impact parameter where the trajectory exhibits an encounter with the repulsive part of the potential.

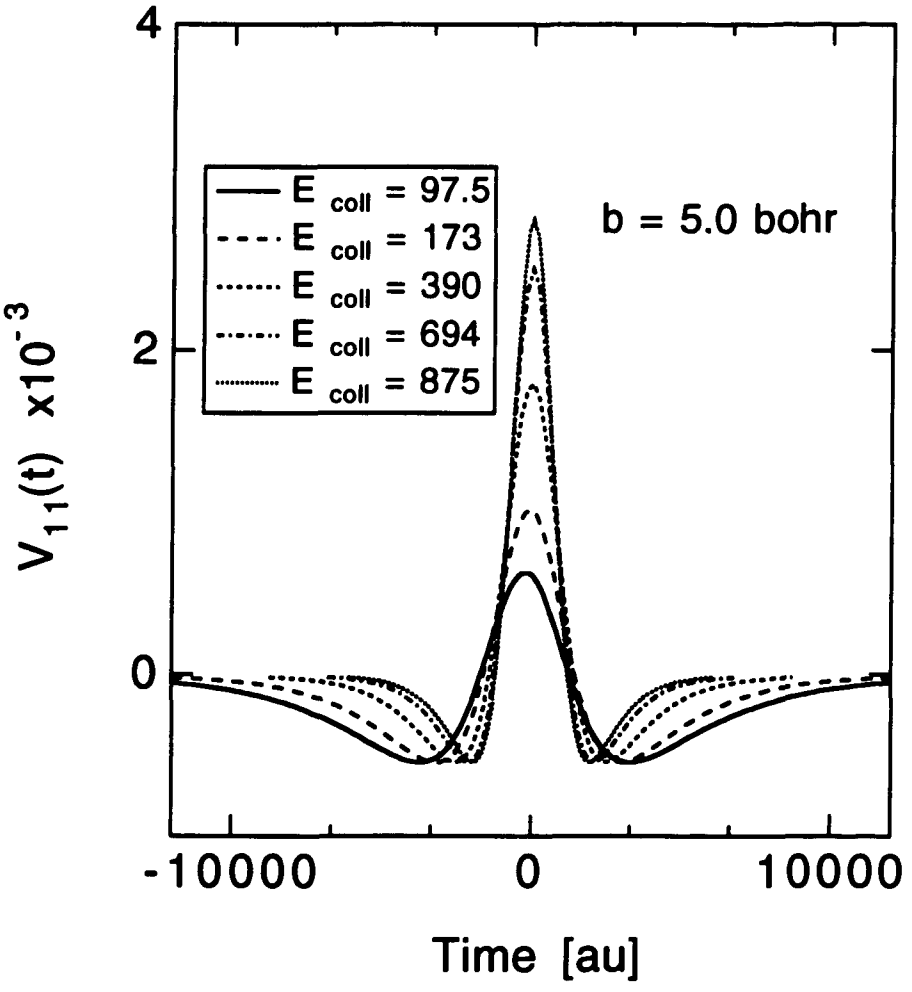

Figure 13. Elastic coupling potential for several collision energies at an impact parameter where the trajectory exhibits an encounter with the repulsive part of the potential. Collision energy in meV.

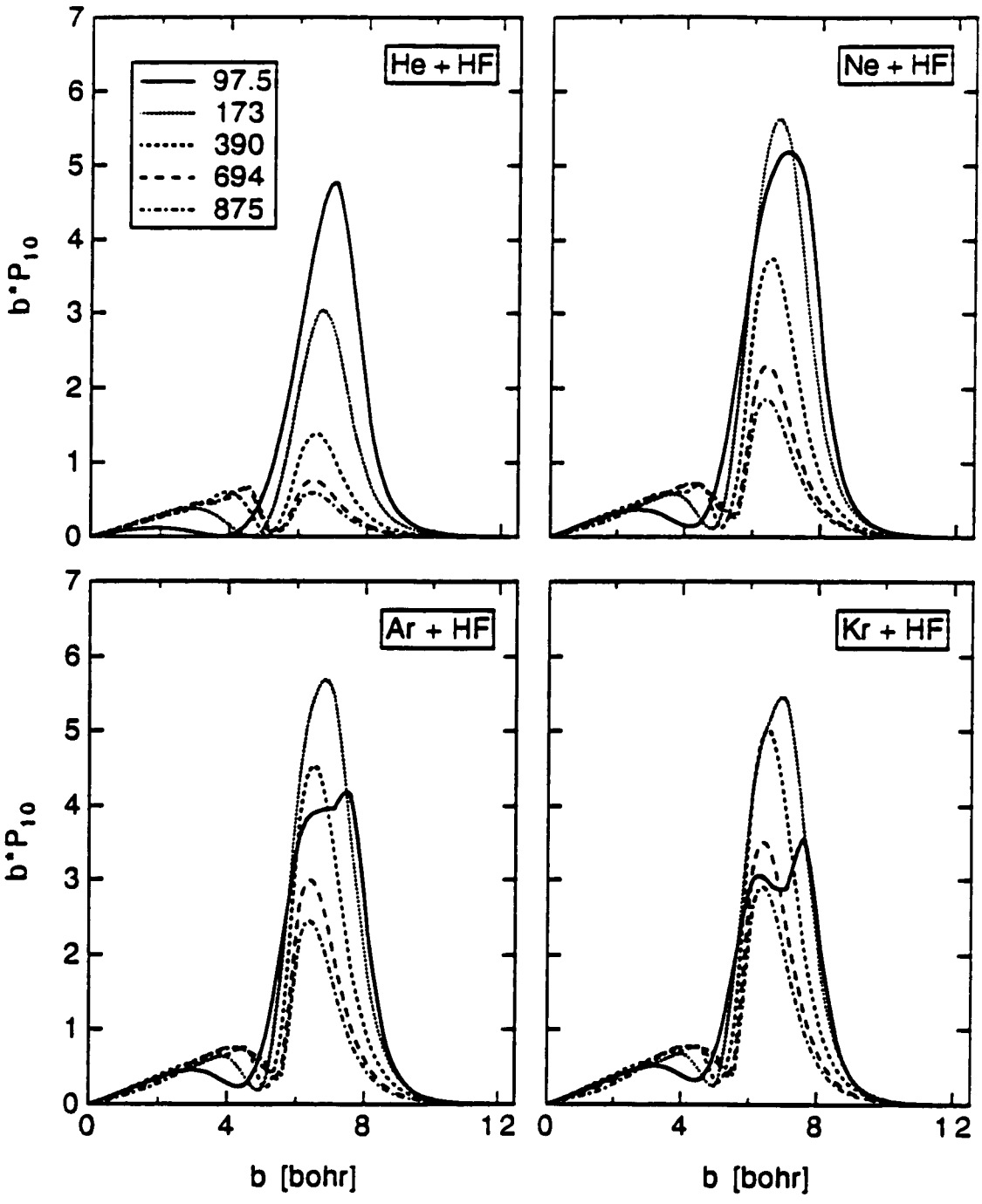

Figure 14. Impact parameter weighted opacity functions for several mass combinations and collision energies. Collision energies in meV.

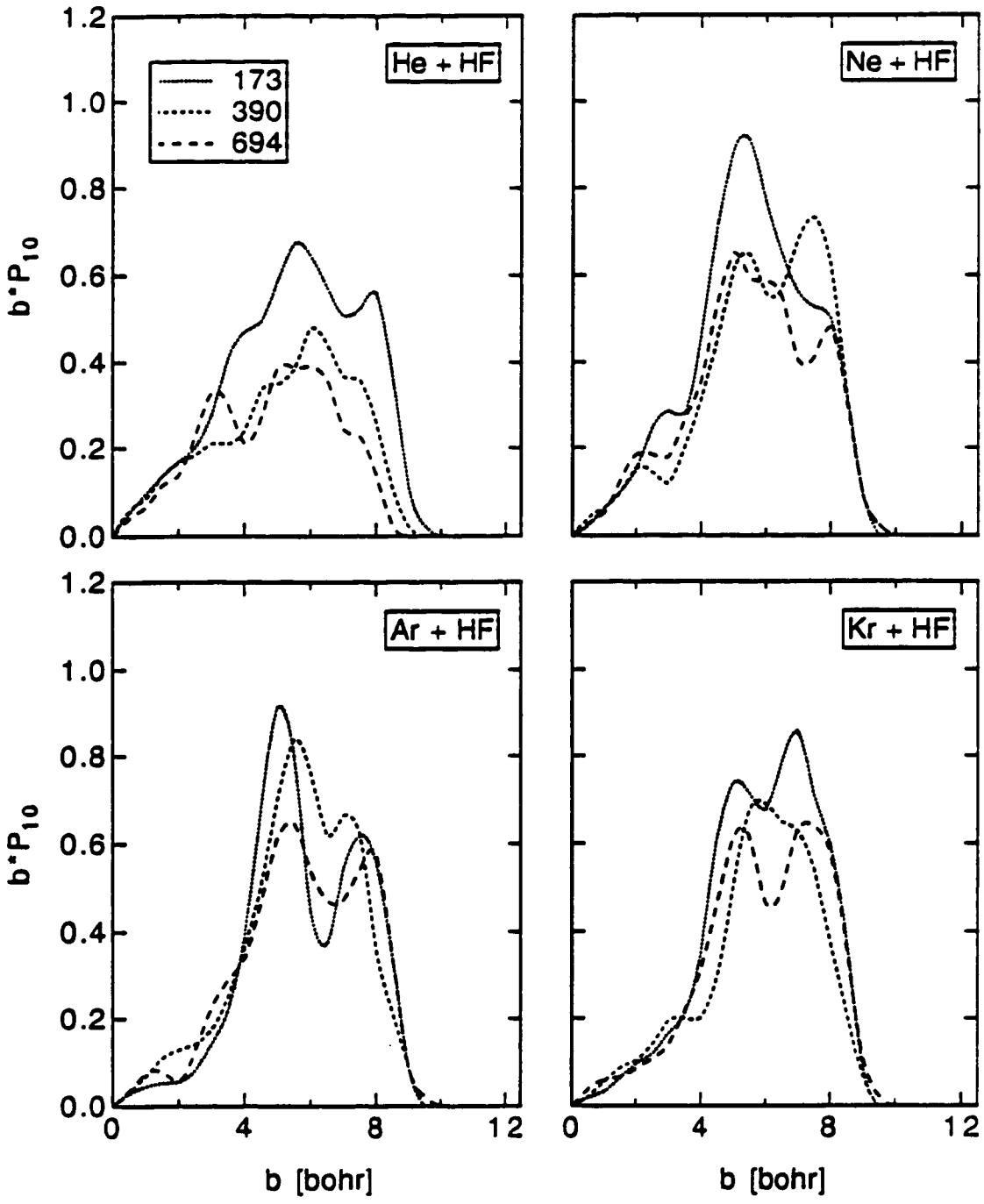

Figure 15. Impact parameter weighted opacity functions for several mass combinations and collision energies from classical trajectories. Collision energies in meV.

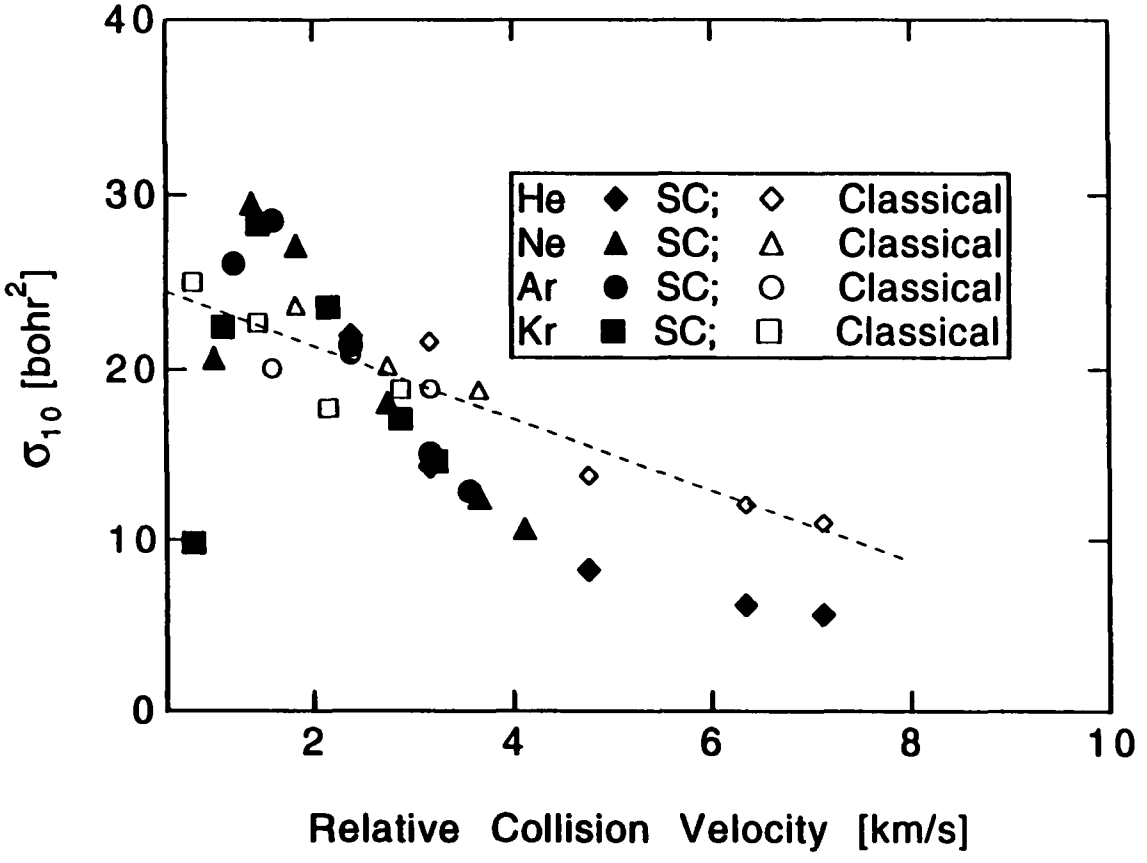

Figure 16. Integral cross sections for all mass combinations as a function of collision velocity. Dashed line is a linear least squares fit to the classical cross sections.

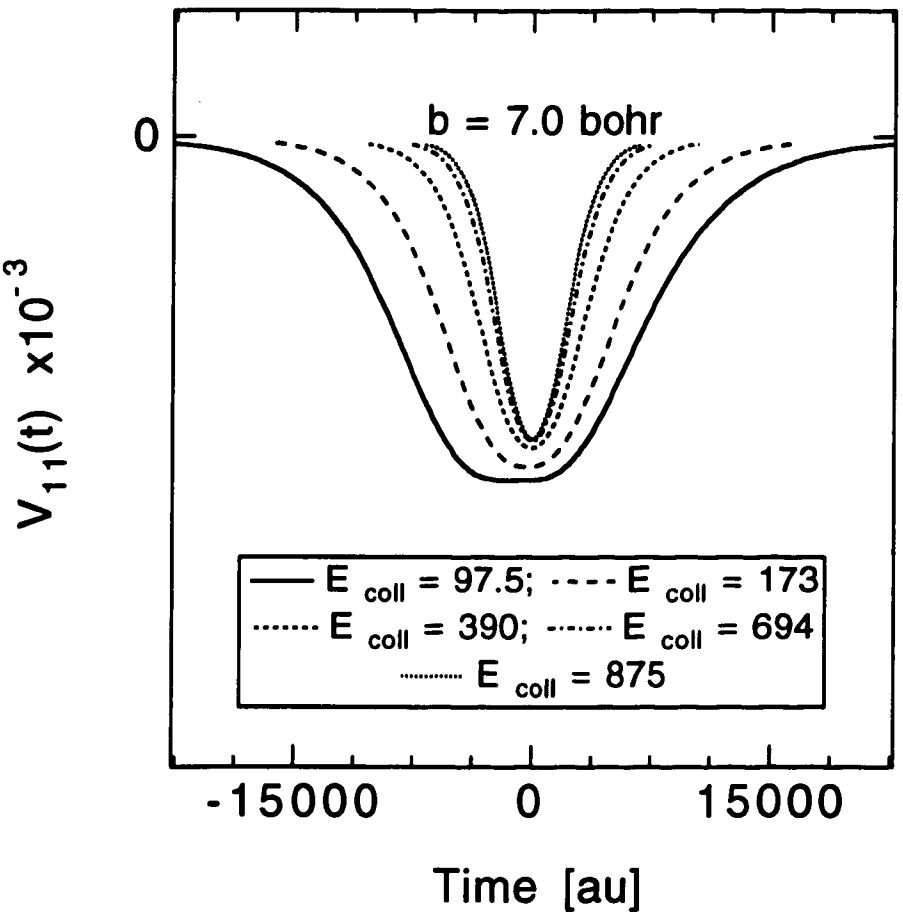

Figure 17. Elastic coupling potential for several collision energies at a single impact parameter.

Chapter 4

Simulation of the Ar+HF Scattering Experiment

I. Introduction

The classical trajectory method has been a workhorse in molecular dynamics calculations since its first applications to chemical reactions in 1965.[1] The method has been employed to study such widely diverse systems as the $H+H_2 \rightarrow H_2+H$ reaction and, more recently, protein dynamics simulations.[2] The method has proved reliable in many applications.

Despite the many successes of the classical trajectory method for predicting reactive and scattering dynamics for small systems (i.e. two to six atoms), many deviations between classical and quantum dynamics have been reported.[3] These discrepancies have led to the acceptance of the importance of quantum effects, arising from tunneling, zero-point energy and resonances, in reaction dynamics.[4]

Exact quantum methods have been developed for studying inelastic scattering processes[5] and have had great success in reproducing experimental scattering results.[6] While these methods have proved valuable for the study of systems containing a small few number of electrons, the methods are still too cumbersome for practical application to many larger

systems. Many approximate techniques have been devised to reduce the number of close-coupled equations required for fully quantum calculations.[7] In particular the infinite order sudden approximation (IOSA)[8] has proved to be an excellent method for describing rotationally inelastic scattering processes.[9] The IOSA has provided invaluable insight into the scattering dynamics for atom+diatom collision systems, and has led to the elucidation of scattering features such as the rotational rainbow.

Even with advances in computer power and theoretical methods, the classical trajectory method has still remained an important source of information on detailed scattering dynamics.[10] The appeal of the classical method lies in its ability to follow the encounter between the collision partners, and in the intuitive link between the scattering dynamics and the potential energy surface governing the collision. This combination of benefits provides valuable insight into the scattering process and the nature of the collision.

Another important function of the classical trajectory method is to provide a benchmark to which scattering results from other methods may be compared. It is in this capacity that allows what are termed "quantum effects" to be defined. In this sense, deviations between classical and quantum models establish the existence of a quantum effect for a particular system. Comparison of the theoretical results to experimental observations indicates the importance of quantum effects (if found) in the description of the natural process.

In this Chapter we present a method for the direct simulation of a scattering experiment using classical trajectories. The method is then applied to rotationally inelastic scattering of hydrogen fluoride from argon. The experiment being modeled is that of Rawluk, et al.[11] In this

experiment a beam of HF molecules is crossed by a second beam of Ar atoms. The scattered HF is detected by means of a laser+bolometer detection system.[12] The experimental setup provides single collision conditions and the detection is final rotational state selective.[11] At the collision energies of this experiment vibrational excitation of the HF by scattering is not energetically permissible.[11]

In Section II the computational methods are presented. These include the standard classical trajectory methods and methods for calculating the center of mass differential cross section. We also present the method for transformation of the center of mass results into the laboratory frame for comparison with experimental results. The method for direct simulation of the experimental conditions is also presented. In Section III we discuss the results of these calculations. We compare the results from more standard methods of calculating laboratory frame differential cross sections with our simulation method. We also examine the effects of the potential energy surface on the scattering dynamics.[13] The classical results are compared to the experimental differential cross sections[11] in Section IV. We also compare the classical and experimental results with fully converged quantum close-coupled results.[14] Conclusions on the methods and the classical to quantum comparison are made in Section V.

II. Calculations

A. Classical trajectory method

The classical Hamiltonian, H_{cl}, in Cartesian coordinates for an atom+diatom collision system is given by

$$H_{cl} = \frac{1}{2M}\mathbf{P}^2 + \frac{1}{2\mu}\mathbf{p}^2 + V(\mathbf{R},\mathbf{r}) \qquad (1)$$

where **R** and **P** are the relative position of the atom to the diatom center of mass and its conjugate momentum vectors, respectively; **r** is the diatom intramolecular bond vector and **p** its conjugate momentum. The interaction potential between a closed shell atom, A, and Σ state diatom, BC, is given by $V(\mathbf{R},\mathbf{r})$, and is single valued. The reduced mass of the collision system is given by

$$M = \frac{m_A(m_B + m_C)}{m_A + m_B + m_C} \tag{2}$$

where m_X is the mass of atom X. The diatom reduced mass is given by

$$\mu = \frac{m_B \cdot m_C}{m_B + m_C} \tag{3}$$

The classical equations of motion, given by the solution of Hamilton's equations of motion, are

$$\dot{\mathbf{P}} = -\nabla_R H_{cl} \quad ; \qquad \dot{\mathbf{R}} = \nabla_P H_{cl} \tag{4a}$$

$$\dot{\mathbf{p}} = -\nabla_r H_{cl} \quad ; \qquad \dot{\mathbf{r}} = \nabla_p H_{cl} \tag{4b}$$

Equations 4 comprise the twelve simultaneous differential equations describing the motion of the particles. Integration of equations 4, from a given set of initial conditions, is performed by a variable step size GEAR integrator.[15]

In the rigid rotor approximation, the length of the intramolecular bond vector is set to the equilibrium bond length, r_e. Within this approximation the interaction potential reduces to a function, $V(R,\gamma)$, of R and γ, the intermolecular separation and the orientation angle between the vectors **r** and **R**, respectively. Due to the cylindrical symmetry of the scattering system the initial intermolecular vector, $\mathbf{R}_i=(0,b,R_z)$, is set up with R_z large and b as the

impact parameter. The initial momentum vector is given by $\mathbf{P}=(0,0,-(2ME_{coll})^{1/2})$. Initial trajectory conditions are specified using standard methods.[1,16] The exception to the standard methods given in references 1 and 16 is the selection of b for the trajectory. Here we follow the methods of Raff, et al.[17] and Barg, et al.[18] The method of references 17 and 18 is to select b linearly, rather than quadratically. This allows a more efficient sampling of the impact parameter region where the more interesting scattering dynamics occur. Of course, when using linear sampling methods, the individual trajectory result must be appropriately weighted.[18]

For a given set of initial conditions we compute a trajectory by solution of equations 4 until some "end" criterion has been satisfied (i.e. the particles have separated to some large distance, typically R>25 bohr). The final trajectory conditions are then determined. These results are labeled with the impact parameter of the trajectory. The scattering angle, θ, is the angle between the initial and final relative momentum vectors, $\mathbf{P}$ and $\mathbf{P}'$, given by

$$\theta = \arccos\left(\frac{\mathbf{P}'\cdot\mathbf{P}}{|\mathbf{P}'||\mathbf{P}|}\right) \tag{5}$$

The final rotational state of the rotor can be determined from the continuous rotational action vector given by

$$\hbar\tilde{\mathbf{j}} = \mathbf{r}\times\mathbf{p} \tag{6}$$

Classically, the rotational energy is given by, $E_{rot} = B\left|\tilde{\mathbf{j}}\right|^2$, where $B=\hbar^2(2\mu r^2)^{-1}$ is the rotational constant of the diatom and $\left|\tilde{\mathbf{j}}\right|$ is the magnitude of the rotational action. Quantum

mechanically, the rotational energy is, $E_{rot} = B\,j(j+1)$, where j is the rotational quantum number. Equating the two expressions for the rotational energy we get a relation between the classical and quantum results

$$\tilde{j} = \left(|\tilde{\mathbf{j}}|^2 + 0.25 \right)^{1/2} - 0.5 \qquad (7)$$

where $\tilde{j}$ is defined as the continuous "rotational quantum number" resulting from the classical trajectory. Following the quasi-classical philosophy we now "bin" $\tilde{j}$ into integer boxes to mimic the quantum result. The binning method most often used is a simple round off,[19] where the trajectory contributes to the j'^{th}-bin if $(j'-0.5) < \tilde{j}' \leq (j'+0.5)$.

B. Differential cross section

The fundamental measure of the overall strength of a scattering event, X, is the integral cross section, σ_X, given as

$$\sigma_X = 2\pi \int_0^{b_{max}} db\, b P_X(b) \qquad (8)$$

where $P_X(b)$ is the probability of the event X as a function of b and $P_X(b)=0$ for $b>b_{max}$. The angular distribution of the scattering event, the differential cross section (DCS), is given by

$$\frac{d\sigma_X(\theta)}{d\varpi} = \frac{1}{d\theta \sin\theta} \int_0^{b_{max}} db\, b\, P_X(b) \qquad (9)$$

where $d\varpi = d\phi\, d\theta \sin\theta$, and due to the cylindrical symmetry of the scattering system in the center of mass (CoM) frame the integral over ϕ is given explicitly as 2π.

In this study we are primarily concerned with the final rotational state selected differential cross section, $\frac{d\sigma_{j'}(\theta)}{d\varpi}$. For each trajectory, labeled with an impact parameter, b, θ and j' are determined using equations 5 and 7, respectively. In order to determine the angular distribution of the scattered products from a Monte Carlo simulation the scattering angles are boxed. The angular boxes are centered at a series of angles, θ_i, with a width of $\Delta\theta_i$. The width of $\Delta\theta_i$ is chosen as fixed or variable over the range of θ. Variable width boxing is used to improve the resolution of the angular distribution where there is typically a high density of trajectories (at lower scattering angles for elastic scattering) and to reduce the error in the scattering region where the scattering density is low (the back scattering direction for highly inelastic collisions). This is most effective when examining state-to-state DCS. The fixed box width method is used when the scattered density is evenly distributed over the entire angular range. This method is used in calculating the experimentally averaged DCS from the Monte Carlo simulation.

A trajectory contributes to the i^{th} angular box if the scattering angle for the trajectory falls within $\theta_i \pm \Delta\theta_i/2$. The frequency or "weight" of scattering into a given angular interval is given by

$$\rho(j', \theta_i; b) = \frac{N(j', \theta_i; b)}{N} \qquad (10)$$

where $N(j', \theta_i; b)$ is the number of trajectories scattering into the i^{th} angular box with final rotational state j'. N is the total number of trajectories. Because θ is being boxed, equation 9 for the DCS is rewritten as

$$\frac{d\sigma_{j'}(\theta_i)}{d\varpi} = \frac{1}{\Delta\theta_i \sin\theta_i} \int_0^{b_{max}} db\, b\rho(j', \theta_i; b) \qquad (11)$$

to incorporate the θ-box size and equation 10.

In the spirit of the quasiclassical trajectory method[17] the impact parameters for the trajectories are selected based upon quantum mechanically allowed values of the orbital angular momentum, ℓ. The relations between b and ℓ are given by

$$b^2 = \ell(\ell+1)\left(\frac{\hbar}{P}\right)^2 \qquad (12a)$$

$$b\,db = \frac{(2\ell+1)}{2}\left(\frac{\hbar}{P}\right)^2 d\ell \qquad (12b)$$

Because of the non-continuous nature of the orbital angular momentum in quantum mechanics, $d\ell$ should be replaced by $\Delta\ell$ in equation 12b. In the trajectory calculations, b is selected from a narrow ℓ-interval centered at ℓ_1. The value of $\Delta\ell$ is chosen so that only a narrow strip of impact parameters is accessed in each ℓ-interval. (For $\Delta\ell$=10, Δb~0.5 bohr, at the collision energies and mass combinations of this study.)

Using equations 12 and substituting $\Delta\ell$ for $d\ell$, equation 11 is transformed from an integral over b to a sum over the orbital angular momentum to give the DCS as

$$\frac{d\sigma_{j'}(\theta_i)}{d\varpi} = \frac{\hbar^2}{2P^2} \frac{\Delta\ell}{\Delta\theta_i \sin\theta_i} \sum_{l} (2\ell_l + 1)\rho(j', \theta_i; \ell_l) \qquad (13)$$

where the weight into a final rotational state and angular box is now labeled by ℓ_1.

Equation 13 is an adequate formulation for the DCS when a fixed collision energy is used for all trajectories. However, for a simulation involving an experimental collision energy distribution function, the DCS is seen to be dependent on P. Since P affects both the transition probability and θ, equation 10 is modified to include the initial collision momentum and scattering angle for each trajectory contributing to a (j',θ_i) box. This "weighted probability" is given as

$$\mathcal{P}\left(j',\theta_i;\ell_l\right)=\left(N_l\right)^{-1}\sum_k \frac{(2\ell_k+1)}{(P_k)^2\sin\theta_k} \qquad (14)$$

where the k refers to the k^{th} trajectory and N_l is the total number of trajectories beginning in the l^{th} ℓ-interval. Using equation 14, the DCS is now given as

$$\frac{d\sigma_{j'}(\theta_i)}{d\varpi}=\frac{\hbar^2\Delta\ell}{2\Delta\theta_i}\sum_l \mathcal{P}\left(j',\theta_i;\ell_l\right) \qquad (15)$$

for a constant $\Delta\ell$.

C. Center of mass to laboratory transformation

In order to compare the calculated DCS to the experimental results, the CoM DCS must be transformed into the laboratory (Lab) frame. The relation between the CoM and Lab frames is illustrated in figure 1 for in-plane scattering. Due to the cylindrical symmetry of the scattering system about the relative collision velocity vector, the CoM scattering angle ($\pm\theta$) has two components which contribute to the Lab frame scattering signal. For obvious reasons the Lab frame vectors from these components are labeled as the "fast", f, and "slow", s, vectors. The Lab frame scattering

angle, Θ, is given as the angle between the initial, $\mathbf{v}_1$, and final, $\mathbf{v}_{1f'(\bullet)}$, Lab velocity vectors.

The Lab frame DCS is given by

$$\frac{d\sigma_{j'}(\Theta)}{d\Omega} = \sum \frac{d\sigma_{j'}(\theta)}{d\varpi} \mathcal{J} \qquad (16)$$

where the sum (if necessary) is over the fast and slow contributions to the Lab scattering angle, Θ. The appropriate[20] transformation Jacobian, $\mathcal{J}$, in equation 16 between the CoM and Lab frames is given by

$$\mathcal{J} = \frac{d\varpi}{d\Omega} = \frac{v'^2_1}{u'^2_1} \cos^{-1}\varepsilon \qquad (17)$$

where $\mathbf{v}'_i$ would be appropriately labelled as the fast or slow component. The angle, ε, as defined in figure 1, is between the final velocity vectors, $\mathbf{u}'_i$ and $\mathbf{v}'_i$.

Because the Jacobian includes velocity terms, this transformation is highly sensitive to the kinematics of the collision. For this reason it is standard practice[14] to compute the CoM cross sections at a single total energy (i.e. fixed collision energy; single initial rotational state) and transform these DCS into the Lab frame. The Lab frame DCS from the single energy calculations would then be appropriately weighted, according to experimental conditions, and averaged for comparison to the experimental results. When many initial states contribute to the final signal and the collisional energy distribution is wide, this standard method can become very cumbersome to implement.

In order to facilitate the CoM to Lab transformation in a trajectory calculation where the experimental conditions

are simulated by Monte Carlo integration, we employ a trajectory-by-trajectory CoM to Lab mapping. That is, each individual trajectory is mapped into the Lab frame carrying its appropriate Jacobian weighting prior to any averaging or boxing in the CoM frame. In a truly "Monte Carlo" simulation, a binary choice to accept the fast or slow Lab frame vector would be made for each CoM trajectory. In this study we have decided to "double" the "work" of each trajectory and include both the fast and slow contributions in the CoM to Lab transformation.

Following the development of the center of mass DCS, the Lab frame results are also labeled by the initial ℓ-interval. The Lab frame scattering angle, Θ, is boxed in a similar fashion to the CoM, a trajectory contributes to a Θ_i-box if Θ falls within $\Theta_i \pm \Delta\Theta_i/2$. A "weighted" Lab frame probability for a scattering event into the i^{th} Lab frame angular box is given as

$$\mathcal{P}\left(j', \Theta_i; \ell_l\right) = \left(2N_l\right)^{-1} \sum_k \frac{(2\ell_k + 1)}{(P_k)^2 \sin\theta_k} \mathcal{J}_k \qquad (18)$$

where k refers to the k^{th} trajectory in the ℓ_l-interval and $2N_l$ is employed to account for the "double work" of the CoM trajectory in the Lab frame. Finally, the Lab frame DCS is given by

$$\frac{d\sigma_{j'}(\Theta_i)}{d\Omega} = \frac{\hbar^2 \Delta\ell}{2\Delta\Theta_i} \sum_l \mathcal{P}\left(j', \Theta_i; \ell_l\right) \qquad (19)$$

The goal of this work is to simulate the experimental conditions of a resent experiment on the final state selected differential cross sections of HF scattering from Ar.[11] See Appendix A for details on the Monte Carlo integration scheme and distribution functions employed to model these

conditions. The translational energy weighting corresponding to the conditions of reference 11 is calculated from the initial beam velocity distributions. Treating the beam distributions as Gaussian, we generate a Gaussian distribution function for the relative collision velocity. The mean and FWHM for the beam and relative collision velocities are given in Table 1. The translational energy weight is calculated by normalizing the sum of the relative collision velocity probability for each of four collision energies to unity. The translational energy and initial rotational state weighting factors are given in Table 2.

III. Results and Discussion

A. Validation of the trajectory-by-trajectory transformation method

In figure 2 we plot the Lab frame classical differential cross sections (DCS) from the classical trajectory method using Monte Carlo integration over the experimental conditions and trajectory-by-trajectory transformation into the Lab frame (referred to hereafter as the MC trajectory method). We also plot the DCS resulting from 24 single total energy trajectory calculations properly weighted and summed over the experimental conditions. In this averaging the initial rotational state weighting is taken as the experimental rotational state distribution from Rawluk, et al.[11]

As can be clearly seen from figure 2 the agreement between the MC trajectory calculation and the weighted average method is very good. The greatest disagreement between the two calculations is in the higher final rotational states, j'=4 and j'=5. This discrepancy is caused primarily by the higher relative error (~12-20%) in the MC calculation due to the low probability of these states in the initial beam distribution and the low transition probability

into these final rotational states. The spread in translational energy (due to the continuous rotational energy in the classical model) is wider for highly inelastic transitions and this also contributes to the discrepancy between the two methods.

The major benefit of the MC trajectory method with direct trajectory-by-trajectory transformation into the Lab frame is that the theoretical Lab frame DCS can be generated in a single trajectory run. This greatly simplifies the computational effort needed to generate the Lab DCS for comparison to the experimental data. In figures 3-5 we compare the MC trajectory Lab frame DCS calculated from trajectory runs using four different potential energy surfaces for the Ar+HF system.[21,22,23,24] In these figures we also plot the experimental DCS from Rawluk, et al.[11] for each j'.

The agreement between the experimental and theoretical DCS for the mid-j' states is qualitatively quite good. However, quantitative differences are evident. Most notable is the disagreement between the classical and experimental DCS in j'=0, there is also disagreement between the classical and experimental DCS in the higher j'. We will discuss the deviation between the theoretical and experimental DCS in greater detail in the next section. For now we concentrate on the differences between the DCS from each of the potentials.

B. Effects of the potential surface on the scattering dynamics

We now relate some of the potential energy surface features to the scattering dynamics observed for each potential energy surface discussed in Chapter 2. Please refer to this Chapter for further details on the potential energy surfaces. In figure 4 we can see that the scattering dynamics

into the j'=2 (and to some extent into j'=3) are relatively insensitive to the potential energy surface. The greatest sensitivity to the potential for these rotational states is in the angular region where the j'=3 signal increases. On each of the potentials, the j'=3 signal falls off rapidly from the strong forward scattering signal (which is due primarily to elastic forward scattering) to a minimum in the angular range Θ~15-30°. The first potential to show resurgence in the j'=3 signal is the very anisotropic HH M5 surface[21] at Θ~20°. The surface with the least repulsive anisotropy, the NCC,[23] which peaks near Θ~55°, is the last surface to recover from the dip in the j'=3 signal. As we shall show below these features can be related to the repulsive wall anisotropy.

The greatest difference between the DCS on these surfaces is for the j'=0 and j'=5 states. In both cases, the DCS diverge drastically after a scattering angle of Θ~15°. The strongest signal in the j'=0 state for backwards scattering is produced by the NCC surface, the largest signal for back scattering in j'=5 is generated on the HH M5 surface. Again, we see a correlation between the repulsive wall anisotropy and the scattering dynamics.

It is well known from "hard wall" scattering theory[25,26] that repulsive anisotropy leads to higher angular momentum transfer and backscattering in atom-diatom collisions.[25] It has also been shown that in addition to repulsive anisotropy, asymmetry (i.e. difference in the potential with respect to a cut along the diatom center of mass perpendicular to the bond axis) in the potential generates high angular momentum transfer.[27] This type of behavior is displayed in the Ar+HF system. Over 75% of the j'=5 signal in the backscattering region comes from transitions out of j=0 and 1. The large signal for j'=5 for the HH M5 surface comes at the expense of the j'=0 (and j'=1) signal (the lowest in the backscattering

region of all the potentials). Conversely, the low j'=5 signal on the NCC surface is complemented by the highest j'=0 signal of all the surfaces.

In an attempt to quantify these observations, we calculate the total differential cross section, given by

$$\frac{d\sigma_{tot}(\Theta)}{d\Omega} = \sum_{j'=0}^{5} \frac{d\sigma_{j'}(\Theta)}{d\Omega} \qquad (23)$$

for each potential surface. We also calculate the percent contribution of each $\frac{d\sigma_{j'}(\Theta)}{d\Omega}$ to the total at a given Θ. The results, at several values of Θ, for selected j' on each surface are given in Table 3.

From an examination of the expansion coefficients, $V_l(R)$, (Table 2, Chapter 2), we can see that the HH M5 surface does indeed display the most anisotropic characteristics. A measure of the total anisotropy at a given R can be taken as a sum over the $V_l(R)$ (excluding l=0). The asymmetry of the potential surface is determined by the magnitude of the contribution from the odd Legendre polynomials. We correlate the asymmetry of the potential surface with inelasticity in the system by plotting, in figure 6, the fraction of the j'=5 contribution to the total DCS at several angles in the back scattering region against the total odd Legendre coefficients at R=3.0 Å. The plot indeed shows a general relationship between the asymmetry of the surface and the inelasticity of the collisions. This type of correlation may provide information which may be helpful in suggesting changes to the potential in order to provide a better fit to experimental data and an improved potential energy surface.

C. Rainbow Scattering

Reexamining figures 3-5 we see that the DCS calculated from the different potential energy surfaces show qualitatively similar structure. The DCS for lower j' ($j' \leq 2$) exhibit the characteristic strong forward peak of elastic scattering and show a slow decreasing signal in the backscattering region. The DCS for the higher j' show a qualitatively different structure. The strong forward elastic scattering signal is apparent, however after an initial decrease of the signal in the mid-scattering angles, the signal increases in the back scattering region. This type of structure is indicative of a rotational rainbow.[28]

In order to examine this structure more carefully, we calculate the DCS out of initial j=0 at a single collision energy. The DCS for this calculation is plotted in the center of mass frame in figure 7. The forward scattering peak is seen only in the $j'=0$ and $j'=1$ DCS with an impact parameter type rainbow,[29] familiar from atom-atom scattering,[30] apparent in the $j'=1$ DCS. The DCS flattens out in $j'=2$ and then shows a sharp increase in the sideways and back scattering for $j' \geq 3$, clearly indicating a rotational rainbow for these higher j' states.

This progression in rainbow structure, from ℓ-type to rotational rainbow, in rotationally inelastic scattering on an attractive potential energy surface was previously reported by Mayne and Keil.[31] The dip and increase in the DCS for $j' \geq 3$ is also seen in the experimental results of Rawluk, et al.[11] (figures 3-5). The ℓ-type rainbow, seen in the $j'=1$ of figure 3 (fixed total energy), is washed out when the results are averaged over the experimental conditions (see figure 3).

The disagreement between the classical trajectory results and the experimental data (particularly evident in the low j' DCS) limits our ability to conclude from the calculations that the progression in rainbow type has been experimentally observed for this system. However, it may be stated that rotational rainbow structure, normally associated with high energy collisions or strongly repulsive potential surfaces,[32] is evident in the j'≥3 experimental data for a system which exhibits a strongly attractive surface.[14] We now address the differences between the theoretical and experimental DCS in more detail.

IV. Comparison Between Theoretical Models and Experimental Results

As was seen in figure 3 (particularly j'=0), the classical DCS from each of the potential energy surfaces used in this study fail to reproduce the experimental results. There are also marked differences between the classical DCS and the experimental results in the high j' (figure 5) as well. In order to determine if these deviations are caused by the classical approximation to the true scattering dynamics or if they are due to inaccuracies in the potential energy surface themselves, quantum close-coupled[33] (CC) calculations were carried out[14] on each of the potential surfaces discussed above.

CC calculations were implemented using the HIBRIDON scattering package[34] and carried out by Alexander and Rawluk.[14] Details of the these calculations are given in reference 14. The calculations were carried out at a single total collision energy, 24 total energies were required to mimic the experimental conditions of Rawluk et al.[11] The center of mass DCS were then transformed into the Lab frame and averaged to produce a Lab frame differential cross section suitable for comparison with the experimental

results. A statistical analysis[35] of the CC DCS on each of the four Ar+HF surfaces[21-24] compared to the experimental results was performed.[14] From this analysis it was concluded that the Hutson H6 potential[24] best reproduced the experimental results of Rawluk, et al.[14] Our comparisons between the theoretical and experimental DCS below will be made using the Hutson H6 potential energy surface.

In figure 8 we compare the classical, quantum CC and experimental DCS for all final rotational states in the Lab frame. Since the CC DCS were calculated using the 24 total collision energies and averaged over the experimental conditions, we use the classical DCS calculated in the same manner for comparison. The experimental DCS were scaled so as to give the best fit to the CC DCS. This scaling procedure amounts to applying a single factor to all of the experimental data points.

As can be seen in figure 8, while quantitative differences remain between the theory and experiment, the CC DCS reproduce the primary features exhibited in the experimental results. Particular note is made of the agreement between the CC experimental DCS for $j'=0$, and the shoulder in this DCS at $\Theta \sim 30\text{-}40°$. The classical DCS completely fails to reproduce the DCS for this final rotational state.

Another disagreement between the classical and quantum models of note is the too steeply increasing forward scattering DCS in the classical model. In the higher final rotational states the agreement between the classical and CC results, for scattering in the sideways and backwards directions, is quite good. This is seen quite clearly in the DCS for $j'=4$ and $j'=5$. Both the classical and CC DCS are higher than the experimental values for these final states. This discrepancy may indicate that the repulsive part of the

Hutson H6 potential may not be a very accurate description of the actual surface for this system.

Recall that the Hutson H6 surface was fit to spectroscopic measurements on the Ar•HF vdW dimer. This surface is especially sensitive to the attractive part of the potential energy surface, near the attractive minimum. By incorporating spectroscopic data on the internal bending modes,[36] Hutson was also able to obtain an excellent fit to the attractive anisotropy of this surface. However, the spectroscopic measurements are relatively insensitive to the repulsive part of the potential. It is precisely this region of the potential surface which is responsible for the highly inelastic transitions that are the major contributors to the high j' DCS. In light of this it should not come as a surprise that the fit is not as good in the repulsive region.

We now examine the j'=0 DCS. Approximately 95% of the total signal in j'=0 comes from either the j=0 or j=1 initial state. These elastic or slightly inelastic scattering events should be sensitive to the attractive part of the potential. This part of the potential the region best characterized by the spectroscopic measurements. The "exact" quantum scattering treatment of this system using the Hutson H6 surface reproduces the salient experimental features, which rules out the potential energy surface as the source of the deviation seen in the classical DCS. Therefore, it is apparent from the comparison of the classical to the CC results that the classical dynamics fails to reproduce the scattering dynamics into this final rotational state.

To investigate further the differences between the quantum and classical dynamics, we examine state-to-state differential cross sections for this system at a single total energy. Since >95% of the j'=0 signal originates in j=0 or

j=1, we concentrate our efforts on transitions out of initial state j=0 at a collision energy of 134.85 meV.

In figure 9 we plot the center of mass differential cross sections for the transitions j=0→j'=0 and j=0→j'=1. The differences between the quantum CC and classical DCS are spectacular. The CC DCS shows a shoulder located in the center of mass frame a θ~45-60°. (Upon transformation into the Lab frame this corresponds to the shoulder observed at Θ~30-40° in the experimental results of Rawluk, et al.[11]) Concomitant with the shoulder in the j'=0 DCS is a hole in the j=0→j'=1 DCS (this "hole" does not appear in the experimental data due to averaging over experimental conditions). Neither of these features, the shoulder in j'=0 or the hole in j'=1, are evidenced in the classical DCS under the same collision conditions.

The shoulder in the j'=0 DCS cannot be assigned as an impact parameter rainbow. For the well depth and collision energies of this calculation, the rainbow would be predicted to appear near θ~7°, we point out that this feature is observed in the j'=1 DCS. The feature is obviously not attributable to a rotational rainbow since the feature appears in the elastic DCS.

The feature does exhibit rainbow like characteristics, in that the shoulder/hole pair shows a monotonic shift with relative collision energy. The hole feature has been shown[14] to be sensitive to both the repulsive wall and attractive well anisotropy. Indeed, when the potential energy surface was altered to make the attractive well symmetric (i.e. removal of the odd Legendre terms from the expansion in the attractive region) the forward scattering signal for j=0→j'=1 went to zero.[14] The features are also sensitive to the balance between the attractive and repulsive parts of the potential. This sensitivity is demonstrated by a shift in the position

of the hole in the $j=0 \rightarrow j'=1$ DCS to 45° and 75° when the calculations are made using the Douketis and NCC potentials, respectively.[14] Because the features observed here are not attributable to well known scattering features in atom-diatom collision and because the features are observed only in the quantum calculation, we assign the features to new type of quantum interference.[14]

V. Conclusions

We have presented a Monte Carlo trajectory method with trajectory-by-trajectory transformation into the Lab frame. We have shown that this method reproduces the Lab frame DCS calculated using the more traditional method of determining the center of mass DCS for a single total collision energy, transforming this DCS into the Lab frame, then averaging the Lab frame DCS of the single energy calculations over the experimental conditions. For this case a minimum of 24 separate center of mass trajectory calculations were required to simulate the experimental conditions. Whereas with the Monte Carlo simulation of the experiment the Lab frame DCS were generated from a single trajectory run. (To generate the plots of figure 2 a total of $\sim 2 \times 10^5$ trajectories were required for the 24 single total energy runs; $\sim 2 \times 10^4$ trajectories were used in the MC trajectory method.)

The classical calculations were carried out on four recent potential energy surfaces for the Ar+HF system.[21-24] Each of these surfaces exhibit the same general characteristics, i.e. each predict the minimum energy geometry to be in the Ar···HF configuration with a secondary minimum in the Ar···FH configuration; each of these surfaces also exhibits some degree of repulsive wall anisotropy. However the potentials show subtle differences from one another, in that the absolute well depths and the degree of repulsive wall anisotropy and asymmetry differ on each

surface. The DCS from the classical calculations are sensitive to each of these differences. The greatest differences between the surfaces are revealed in the elastic (or nearly elastic) j'=0 and the very inelastic j'=4 and j'=5 DCS.

The DCS into the high j' (i.e. j'= 4 and 5) show the greatest sensitivity to the repulsive wall. We have shown that the inelasticity of the collisions is not only sensitive to the repulsive anisotropy, but is related to the asymmetry of the potential. This sensitivity may be exploited in future studies to suggest improvements to the repulsive part of the potential energy surface, a region of the potential not readily accessible from spectroscopic studies. In this manner scattering experiments provide complementary information to the available spectroscopic data.

We used state-to-state classical calculation at a single collision energy to examine the rainbow structure in the DCS in the center of mass frame. It is evident from the calculations that the progression in rainbow structure from a ℓ-type rainbow to a rotational rainbow occurs in this system. However, the ℓ-type rainbow in j'=1 in washed out when we average the results over the experimental conditions. In order for this rainbow progression to be observed experimentally, better initial state selection, as well as improved angular resolution will be required.

The classical calculations fail to reproduce the scattering dynamics into j'=0. The experimental results show a clear shoulder in the Lab frame DCS centered near Θ=40°. The fully averaged classical DCS show no indication of this shoulder. "Exact" quantum close-coupled calculations were performed[14] in order to determine if this result was due to problems with the potential or the classical approximation to the collision dynamics. The fully averaged CC DCS calculated

with the Hutson H6 potential[24] reproduced all of the salient features observed in the experimental DCS.[11] The classical results on the same surface agree very well with the CC for the high j' DCS. From this it was concluded that the classical mechanics was the source of the deviation in the j'=0 DCS and that the repulsive wall of the Hutson potential requires additional fitting in order to bring the theoretical (quantum) results in line with the experiment.

In order to investigate the source of the shoulder in the j'=0 DCS, we examined state-to-state center of mass differential cross sections at a single collision energy. These calculations reveal a novel shoulder/hole feature in the CC DCS for the transitions $j=0\rightarrow j'=0/j=0\rightarrow j'=1$. These features were completely absent from the classical DCS. This shoulder/hole feature was found to show rainbow like qualities, but could not be assigned as a rotational or ℓ-type rainbow. The feature was found to be sensitive to the both the repulsive and attractive anisotropy of the potential surface. In light of these findings the shoulder/hole features was assigned as a new quantum scattering feature.[14] In our continuing work we will investigate the exact nature of this new quantum feature.

References

1. M. Karplus, R. N. Porter and R. D. Sharma, J. Chem. Phys., **43**, 3259 (1965)

2. C. L. Brooks, III, M. Karplus and B. M. Pettitt, Adv. Chem. Phys., **71**, 1 (1988)

3. G. C. Schatz and A. Kuppermann, J. Chem. Phys., **65**, 4668 (1976);
   M. Baer, H. R. Mayne, V. Khare and D. J. Kouri, Chem. Phys. Lett., **72**, 269 (1980);
   H. Kornweitz, A. Perksy and M. Baer, J. Chem. Phys., **94**, 5524 (1991)

4. P. Kollman, Ann. Rev. Phys. Chem., **38**, 303 (1987);
   D. G. Truhlar, ed., *Resonances in Electron-Molecule Scattering, van der Waals Complexes and Reactive Chemical Dynamics Calculations*, ACS Symp. Ser. 263., Am. Chem. Soc., Washington, DC, (1984), 552;
   G. C. Schatz, Ann. Rev. Phys. Chem., **39**, 317 (1988)

5. J. C. Light, *Atom-Molecule Collision Dynamics*, ed. R. B. Bernstein Plenum, NY (1979) Chap. 6;
   D. Secrest, *ibid*, Chap. 8

6. K. Rudolph and J. P. Toennies, J. Chem. Phys., **65**, 4483 (1976);
   D. A. V. Kliner, D. E. Adelman and R. N. Zare, J. Chem. Phys., **95**, 1648 (1991)

7. D. Wang and J. M. Bowman, J. Chem. Phys., **96**, 8906 (1992);
   D. J. Kouri, *Atom-Molecule Collision Dynamics*, ed. R. B. Bernstein Plenum, NY (1979) Chap. 9

8. R. T Pack, J. Chem. Phys., **60**, 633 (1974);
   G. A. Parker and R. T Pack, J. Chem. Phys., **68**, 1585 (1978)

9. H. J. Korsch and R. Schinke, J. Chem. Phys., **75**, 3850 (1981)

10. G. C. Schatz, Top. Curr. Phys., **33**, 25 (1983);
    J. A. Harrison and H. R. Mayne, J. Chem . Phys., **88**, 7424 (1988)

11. L. J. Rawluk, Y. B. Fan, Y. Apelblat and Keil, J. Chem. Phys., **94**, 4205 (1991)

12. L. J. Rawluk and M. Keil, J. Opt. Soc.Am. B, **6**, 1278 (1989);
    Y. B. Fan, L. J. Rawluk and M. Keil, J. Opt. Soc.Am. B, **8**, 1218 (1991)

13. Potential energy surfaces used in this study are discussed in detail in Chapter 2 of this dissertation.

14. L. J. Rawluk, M. Keil, M. H. Alexander, H. R. Mayne and J. J. C. Barrett, Chem. Phys. Lett., **202**, 291 (1993)

15. C. W. Gear, *Numerical Initial Value Problems in Ordinary Differential Equations*, Prentice Hall, Englewood Cliffs, NJ (1971)

16. L. M. Raff and D. L. Thompson, *Chemical Reaction Dynamics*, ed M. Baer, CRC Press, Boca Raton, FL (1985), pp.14-23

17. L. M. Raff, D. L. Thompson, L. B. Sims and R. N. Porter, J. Chem. Phys. **56**, 5998 (1972)

18. G. D. Barg, G. M. Kendall and J. P. Toennies, Chem. Phys., **16**, 243 (1976)

19. A. F. Wagner and A. C. Wahl, J. Chem. Phys., **69**, 3756 (1978);
A. Metropoulos and D. M. Silver, J. Chem. Phys., **81**, 1682 (1984);
Reference 16, p. 41

20. T. T. Warnock and R. B. Bernstein, J. Chem. Phys., **49**, 1878 (1968) For a "flux detector" the signal is independent of the particle velocity. For a "density detector" the signal is inversely proportional to the final particle velocity.

21. J. M. Hutson and B. J. Howard, Mol. Phys., **45**, 791 (1982)

22. C. Douketis, J. M. Hutson, B. J. Orr and G. Scoles, Mol. Phys., **52**, 763 (1984)

23. D. J. Nesbitt, M. S. Child and D. C. Clary, J. Chem. Phys., **90**, 4855 (1989)

24. J. M. Hutson, J. Chem. Phys., **96**, 6752 (1992)

25. D. Beck, U. Ross and W. Schepper, Z. Phys., **A293**, 107 (1979)

26. S. Bosanac, Phys. Rev. A, **22**, 2617 (1980)

27. J. J. Barrett and H. R. Mayne, Chem. Phys. Res., **1**, 85 (1990)

28. R. Schinke and J. M. Bowman, *Molecular Collision Dynamics*, ed. J. M. Bowman, Springer, Berlin (1982), Chapter 4

29. H. J. Loesch, Adv. Chem. Phys., **52**, 421 (1980);
R. Schinke, H. J. Korsch and D. Poppe, J. Chem. Phys., **77**, 6005 (1982)

30. R. A. Aziz, *Inert Gases: Springer Series in Chemical Physics*, ed. M. L. Klein, Springer, Berlin (1984) **34**, Chap. 2

31. M. Keil and H. R. Mayne, Chem. Phys. Lett., **85**, 456 (1982)

32. R. Schinke and H. J. Korsch, Chem. Phys. Lett., **74**, 449 (1980)

33. W. A. Lester, Jr., Meth. Comput. Phys., **10**, 211 (1971), and references therein.

34. HIBRIDON is a package of programs for the time-independent treatment of inelastic collisions and photodissociation written by M. H. Alexander, D. E. Manolopoulos, H.-J. Werner, and B. Follmeg, with contributions by P. F. Vohralik, D. Lemoine, G. Corey, B. Johnson, T. Orlikowski, W. Kearney, A. Berning, A. Degli-Esposti, C. Rist and P. Dagdigian

35. L. J. Danielson and M. Keil, J. Chem. Phys., **88**, 851 (1988)

36. C. M. Lovejoy and D. J. Nesbitt, J. Chem. Phys., **91**, 2790 (1989)

Table 1. Beam velocity distribution from Rawluk, et al. refence 11.

	Mean velocity [km s^{-1}]	FWHM [km s^{-1}]
HF	1.21	0.241
Ar	0.559	0.0414
Relative	1.333	0.218

Table 2. Collision energy and initial rotational state weighting used in calculating the Lab frame DCS from 24 single total energy trajectory runs.

Relative Collision Energy [meV]	Weight	Initial Rotation State	Weight
82.43	0.0223	0	0.280
107.04	0.4120	1	0.370
134.85	0.5206	2	0.210
165.88	0.0451	3	0.100
Total	1.0000	4	0.032
		5	0.008
		Total	1.000

Table 3. Total differential cross section and fractional contribution of j' DCS to the total at several values of Θ. All cross section in Å^2/sr. Column headings $f_{j'}=\frac{\partial\sigma_{j'}(\Theta)/\partial\Omega}{\partial\sigma_{tot}(\Theta)/\partial\Omega}$.

Hutson H6				
Θ [degree]	$\frac{\partial\sigma_{tot}(\Theta)}{\partial\Omega}$	f_0	f_2	f_5
12	76.4	0.25	0.22	0.02
62	3.94	0.10	0.31	0.03
72	3.35	0.09	0.25	0.07
92	2.31	0.10	0.23	0.12
HH M5				
Θ [degree]	$\frac{\partial\sigma_{tot}(\Theta)}{\partial\Omega}$	f_0	f_2	f_5
12	65.9	0.31	0.19	0.01
62	4.39	0.04	0.22	0.27
72	3.51	0.04	0.25	0.27
92	2.42	0.03	0.23	0.37
Douketis				
Θ [degree]	$\frac{\partial\sigma_{tot}(\Theta)}{\partial\Omega}$	f_0	f_2	f_5
12	88.3	0.28	0.18	0.01
62	4.18	0.11	0.25	0.06
72	3.59	0.13	0.23	0.11
92	2.36	0.12	0.24	0.19
NCC				
Θ [degree]	$\frac{\partial\sigma_{tot}(\Theta)}{\partial\Omega}$	f_0	f_2	f_5
12	81.2	0.28	0.19	0.01
62	4.04	0.23	0.24	0.01
72	3.57	0.25	0.26	0.02
92	2.40	0.27	0.17	0.05

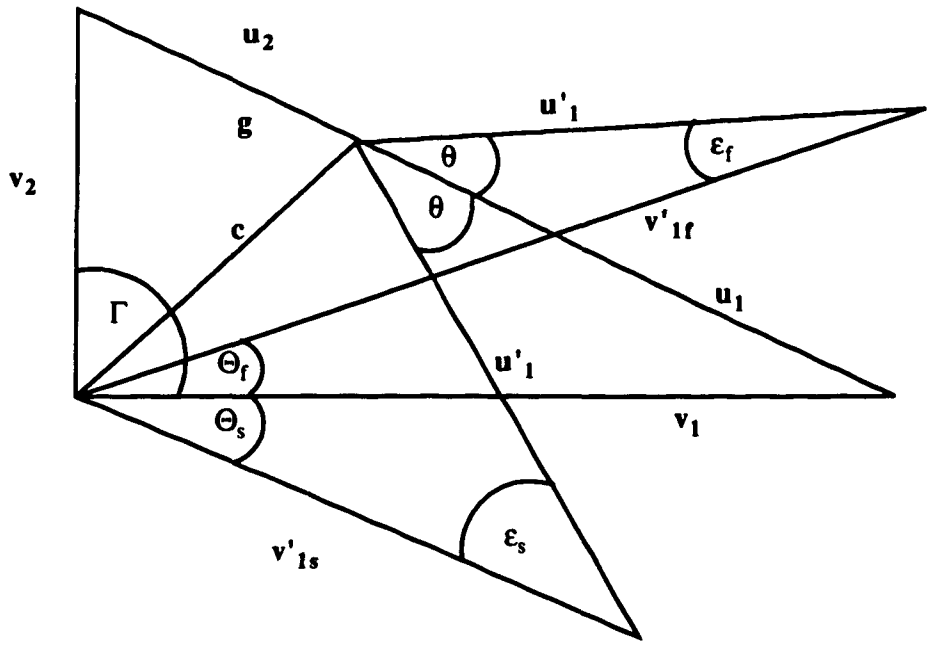

Figure 1. Newton diagram relating the CoM and Lab frames. Subscripts 1 and 2 represent the primary (detected) and secondary collision particles. The particle velocity vectors are labled with **v** or **u** indicating the Lab or CoM frame, respectively. Final velocity vectors are primed. The vector **c** is the system center of mass velocity. Due to cylindrical symmetry about the relative velocity vector, $\mathbf{g}(=\mathbf{v}_1-\mathbf{v}_2)$, a final CoM vector with scattering angle, θ, may result in two Lab frame vectors with Lab frame scattering angles, Θ. The subscripts f and s refer to the "fast" and "slow" final Lab frame velocities. The angle between **u'** and **v'** is ε.

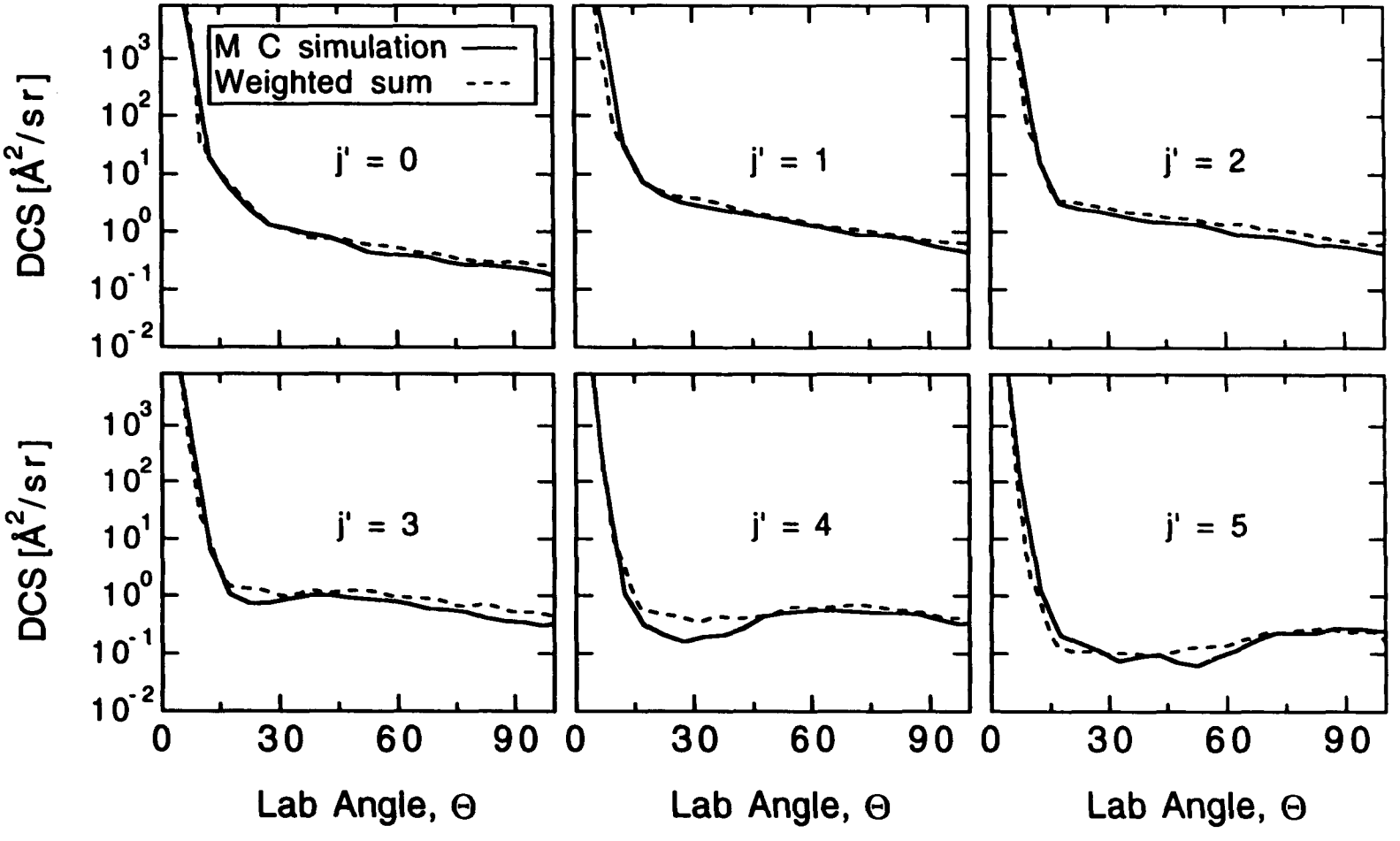

Figure 2. Comparison of classical Lab frame differential cross sections using the MC simulation method and the DCS from a weighted sum of 24 single energy trajectory calculations. Trajectory conditions selected to mimic the Rawluk, et al. experiment of reference 11.

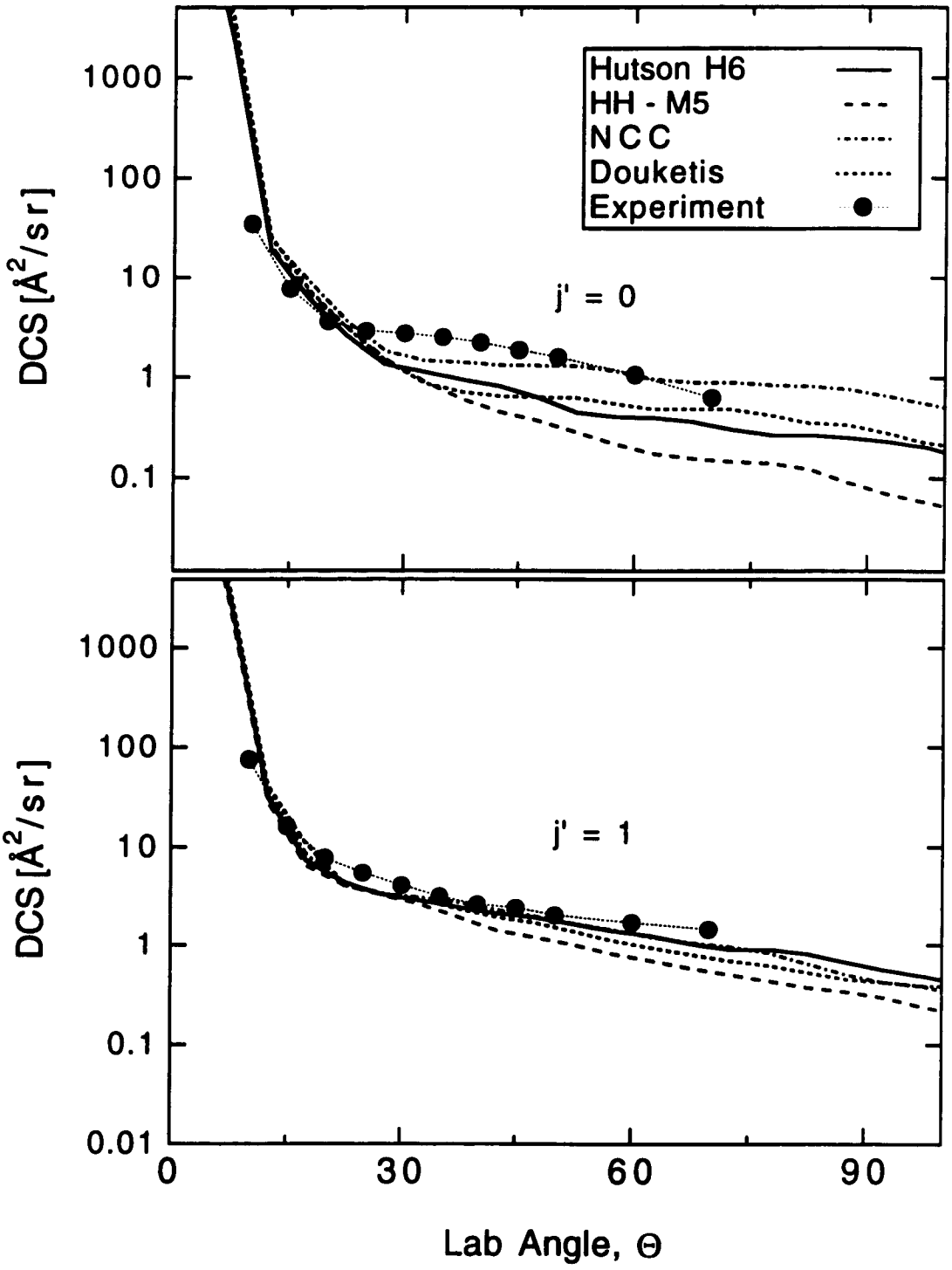

Figure 3. Comparison of Lab frame differential cross sections calculated on each potential energy surface using the MC simulation method. Trajectory conditions are selected to mimic the experiment of Rawluk, et al., reference 11. Also show are the experimental differential cross section of reference 11. The experimental cross sections are adjusted as discussed in reference 14.

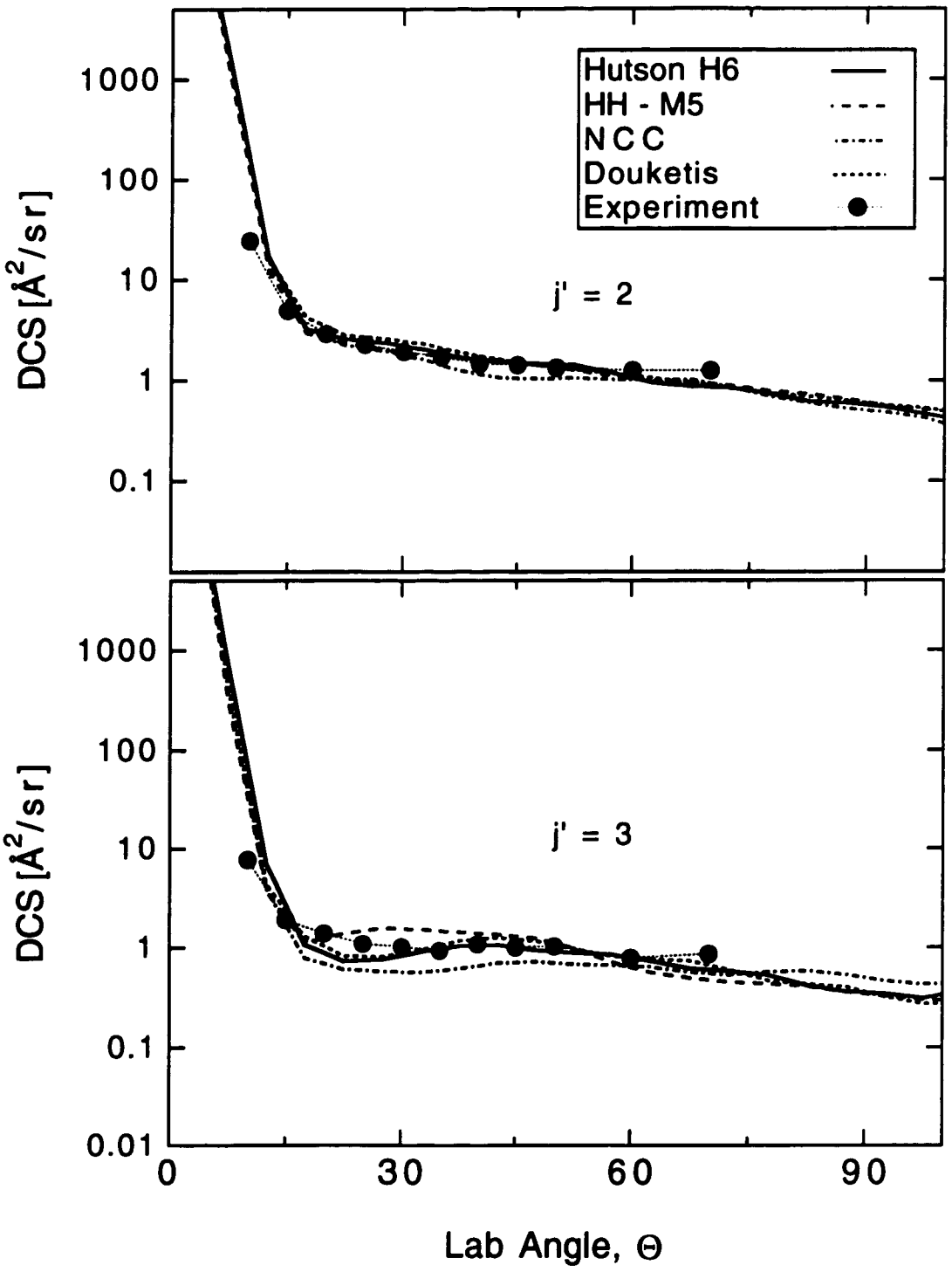

Figure 4. Same as figure 3 except for final j as indicated.

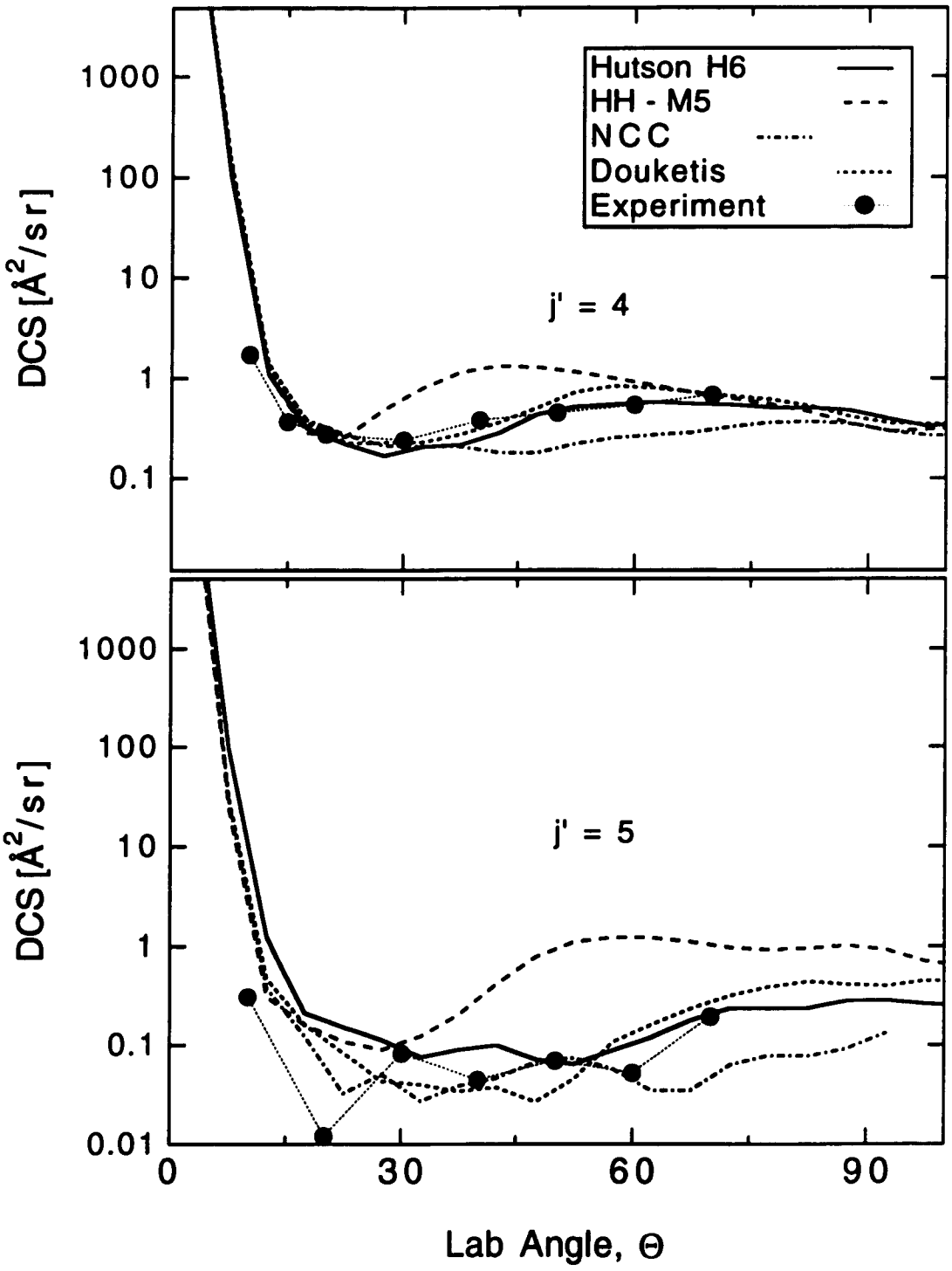

Figure 5. Same as figure 3 except for final j as indicated.

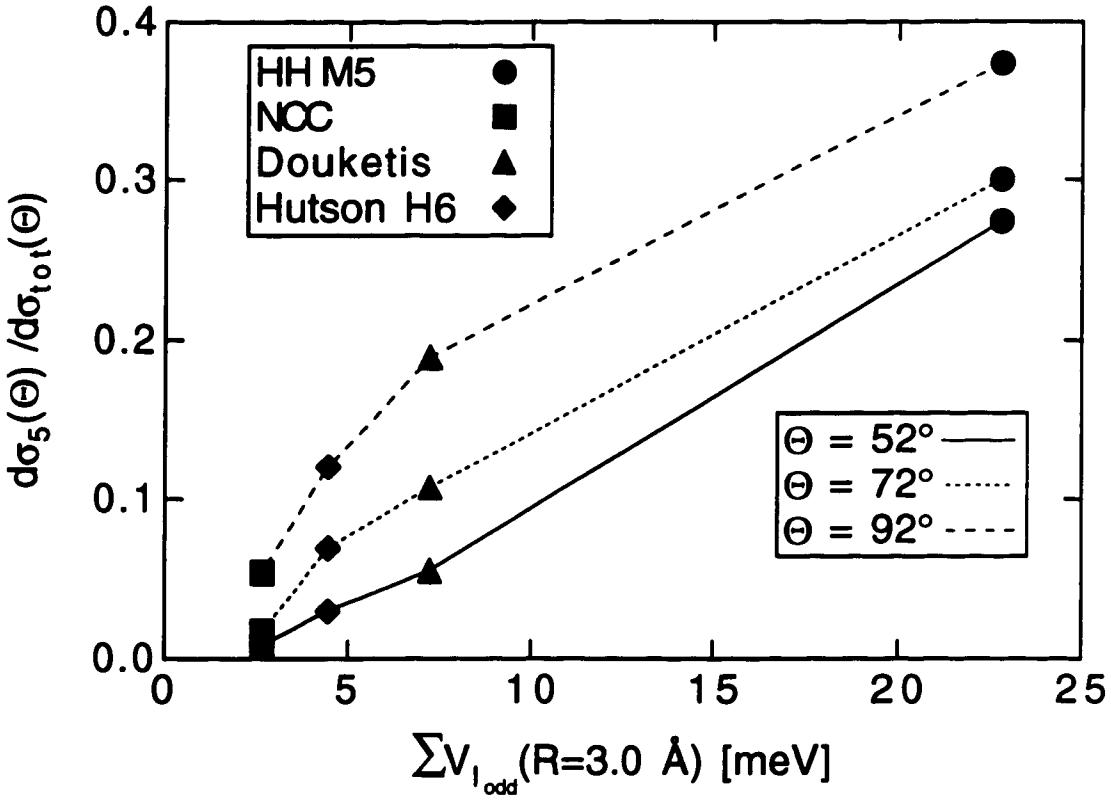

Figure 6. Comparison of the relative inelasticity of each surface verus the asymmetry of the of the potential at several Lab frame scattering angles.

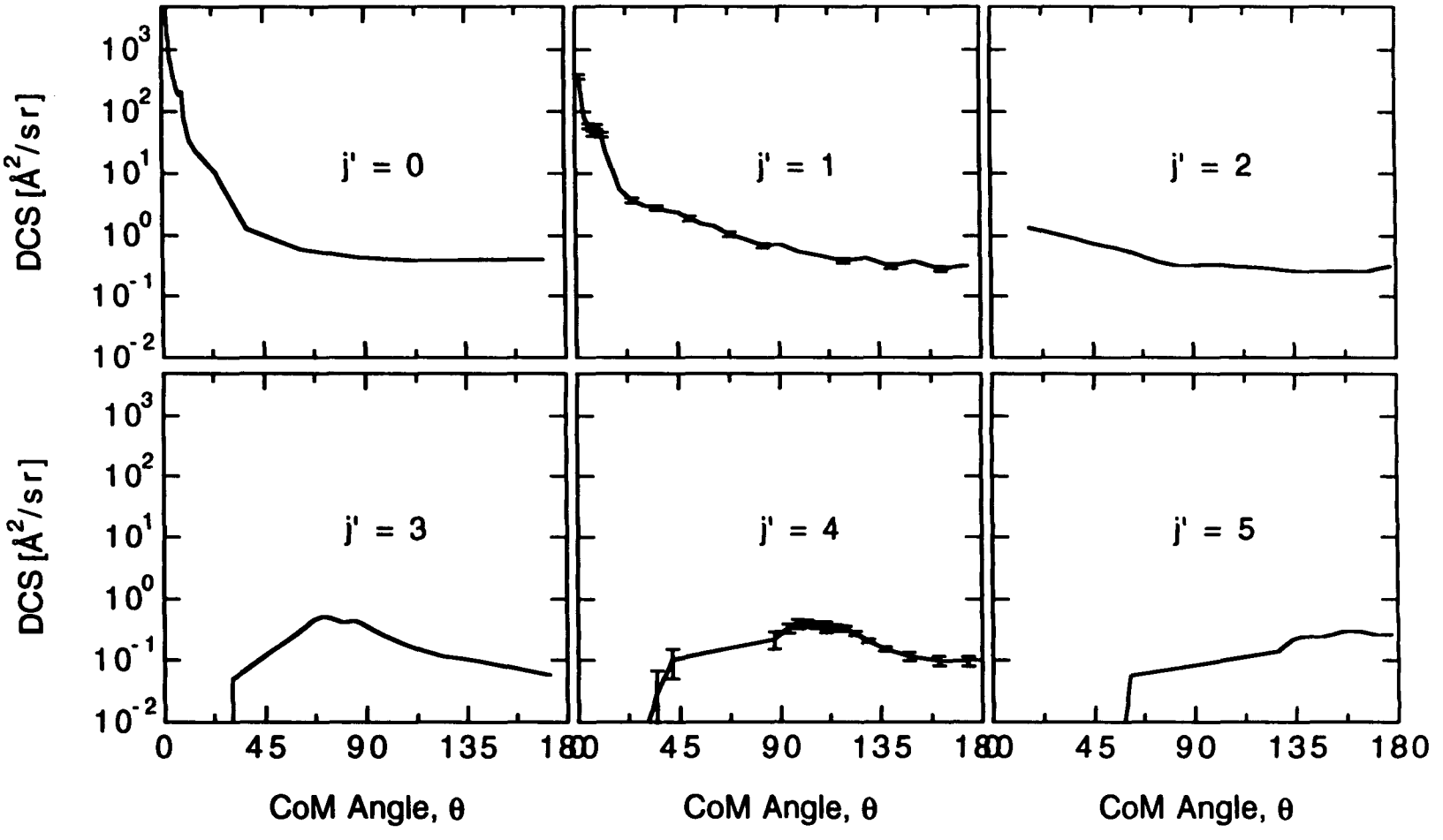

Figure 7. Classical center of mass differential cross sections calculated on the Hutson H6 potential. Initial j = 0; collision energy is 135 meV. Error bars on j'=1 and j'=4 are representative of the other j'.

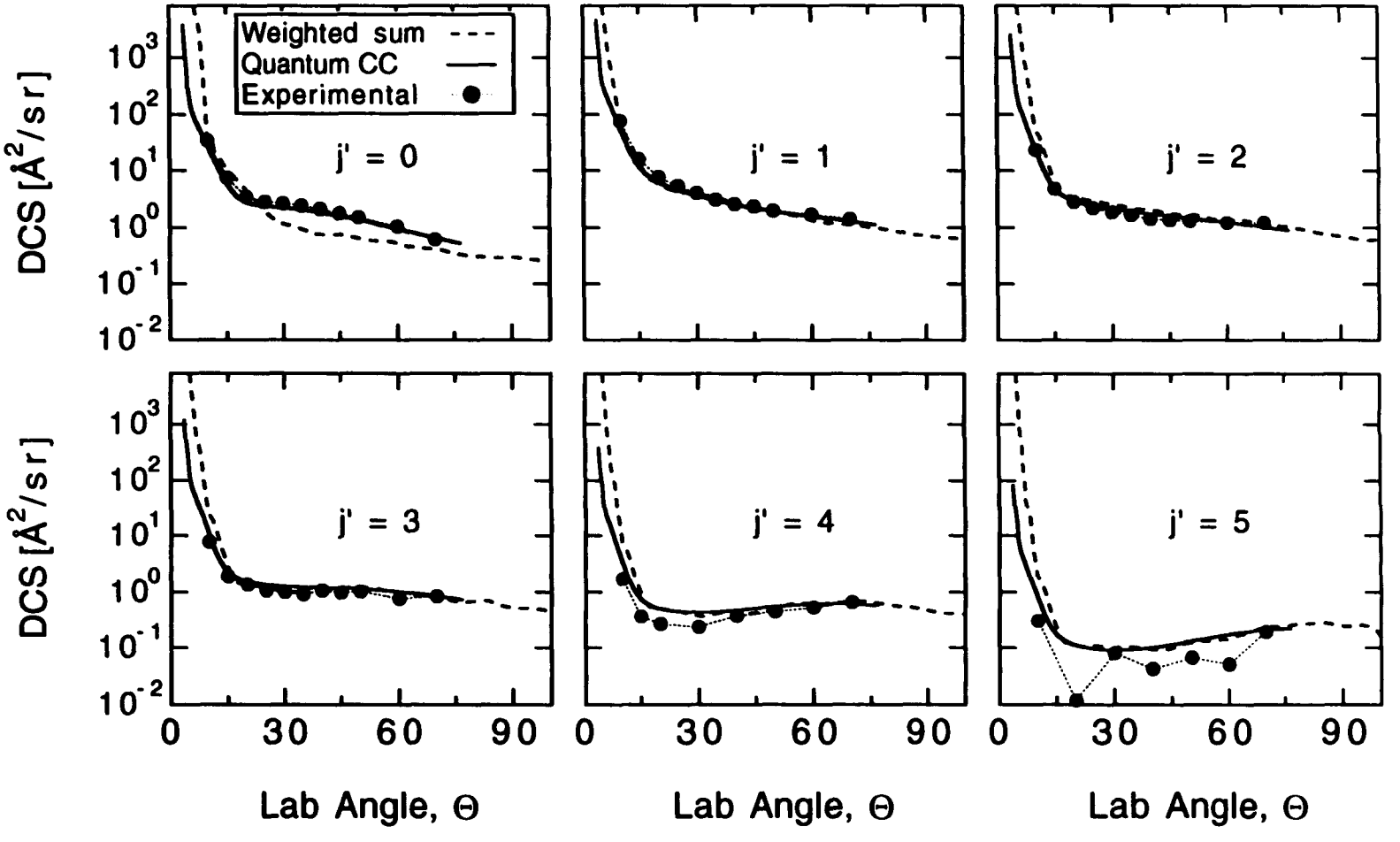

Figure 8. Comparison of classical and quantum Lab frame differential cross sections to the expermential DCS of Rawluk, et al., reference 11. Expermential DCS adjusted as discussed in reference 14.

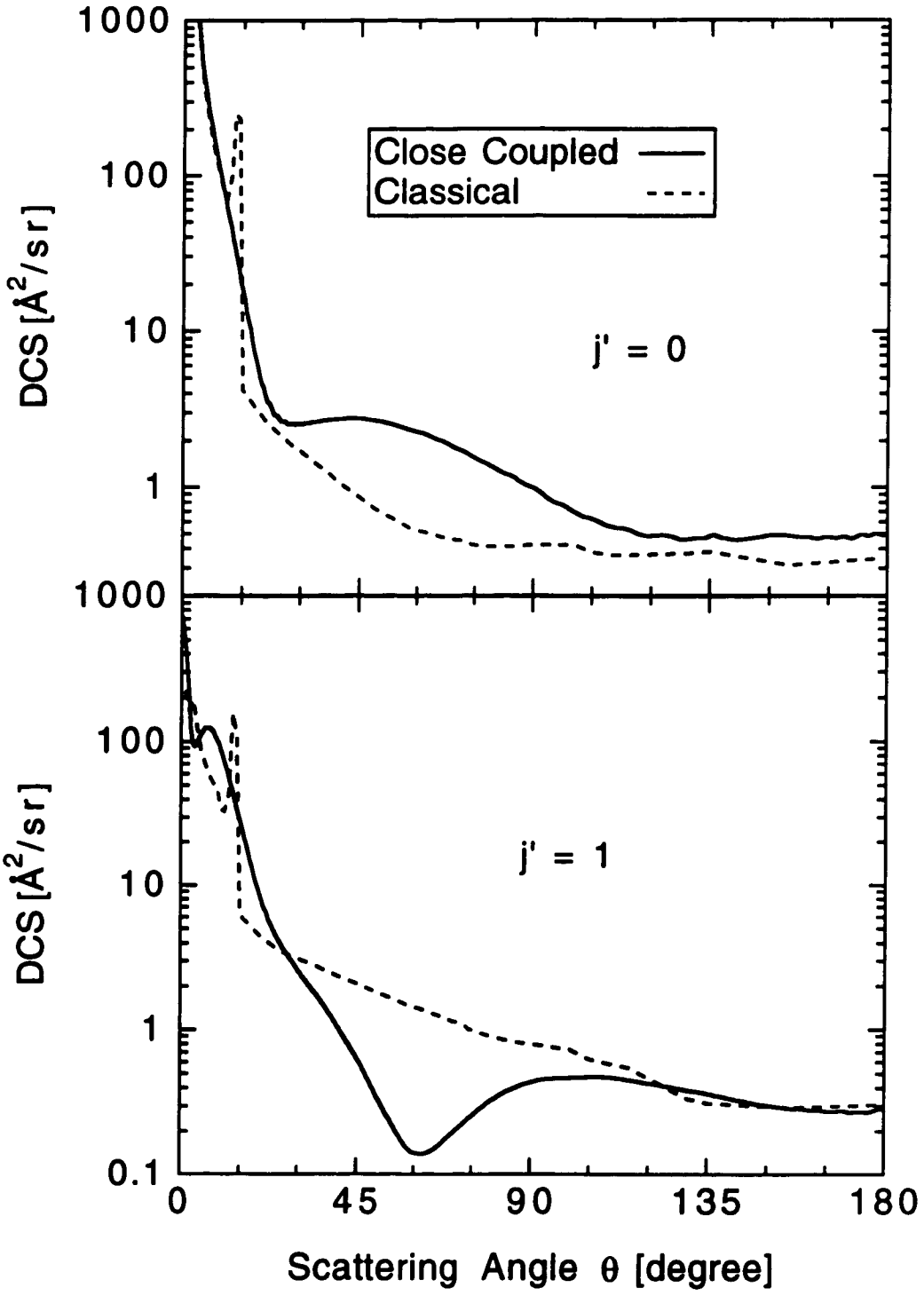

Figure 9. Comparison of classical and quantum center of mass differential cross sections calculated on the Hutson H6 potential. Initial j = 0; collision energy is 135meV.

Chapter 5

Quantum Effects in Ar+HF Rotationally Inelastic Scattering A Semiclassical Interpretation

I. INTRODUCTION

Recent experimental[1] and computational[2] studies of rotationally inelastic scattering of HF by Ar show several unexpected and previously unobserved features. These features apparently have a quantum mechanical origin, as illustrated by their complete absence from corresponding classical calculations.[2] The computationally converged state-to-state "exact" quantum differential cross sections (DCS) also show pronounced isotope effects when compared to Ar+DF scattering. The realistic nature of these calculations, carried out on a potential energy surface fitted to spectroscopic precision for the Ar•HF van der Waals molecule,[3] is strongly substantiated by good reproduction of experimental DCS measurements for state-resolved Ar+HF scattering.[2] Despite numerous computational investigations, however, the physical origin of the quantum features was not fully elucidated by our recent study.

Earlier investigations into the origin of quantum features observed for rotationally inelastic scattering focussed on systems with no substantial attractive anisotropy[4] (unlike Ar+HF). As an example, the Ne+Na_2 system, having almost the same reduced mass as Ar+HF, can be interpreted on the basis of rotational rainbow structure[5] using the infinite-order sudden approximation (IOSA) and hard-shell models.[6] However, Ar+HF scattering appears to be significantly more complicated than systems examined previously. For example, no recognizable rainbow structure, attractive or repulsive, has yet been resolved for Ar+HF scattering.[1,2,7] Furthermore, the large rotational energy spacing for HF violates the energy sudden component of the IOSA.[8] Our earlier work[2] showed that the IOSA, while giving DCS qualitatively similar to the exact results, was quantitatively inaccurate. We have investigated the origin of this discrepancy in a separate study,[9] and find that the energy sudden approximation is, indeed, the culprit. Thus, in order to investigate this system, we must abandon the IOSA, with its computational simplicity, and use a more appropriate dynamical method.

Our earlier computational work showed that at least some of the observed features of the DCS are due to the attractiveness of the potential energy surface for Ar+HF, and to its substantial anisotropy.[2] The goal of our present study is to further elucidate the origin of the most pronounced DCS features, and to investigate how such features probe specific regions of the potential energy surface for Ar+HF scattering. In particular, it would be very helpful if some of the novel quantum features found in our earlier study could be connected to specific regions of the potential energy surface, much as rotational rainbow structure has been connected to the repulsive wall in such systems as Ne+Na_2.[6]

As in our earlier work,[2] we focus attention on the elastic $j=0\rightarrow j'=0$ and the weakly-inelastic $j=0\rightarrow j'=1$ DCS. At

a collision energy of 135 meV, chosen to mimic the experimental measurements,[1] the $j=0\rightarrow j'=0$ DCS shows a broad shoulder centered at a scattering angle of $\theta\approx 60°$ in the center-of-mass (CoM) frame. In the same region, the $j=0\rightarrow j'=1$ DCS shows a sharp minimum that is very sensitive to the potential surface.[2] In the present work, we use only Hutson's "H6" surface for HF in its ground vibrational state, $v=0$.[3]

The quantum close-coupling (CC) calculations reported here were performed using the Hibridon scattering package,[10] as discussed in our earlier work.[2] The CC calculations show rapid quantum diffraction oscillations[11] having periods of $<2°$, which we remove (using a 2°-wide smoothing function) simply to avoid obscuring broader DCS features.

In this paper we present semiclassical (classical path) calculations in an attempt to investigate the novel scattering features seen earlier. In order to elucidate the quantum origin of the effects, we compare these semiclassical results with their classical limit. Both semiclassical and classical methods are described in Section II. Results from these calculations are discussed in Section III, and lead us to consider a time-dependent model calculation in Section IV. Finally, we summarize the insights gained from the semiclassical and model calculations in Section V. We devote close attention to connecting our understanding of the scattering features to particular aspects of the potential surface and discuss the utility of these connections for improving the potential surface.

II. CALCULATIONS

A. Semiclassical Method

We use the traditional Jacobi coordinates to treat the dynamics. The HF bond vector is **r**, the displacement of the Ar atom to the HF center of mass is **R**. Because of the relatively

light HF reduced mass, we treat the rotational states of the diatom quantum mechanically by expansion in a rigid rotor (spherical harmonic) basis set over $\hat{\mathbf{r}}$. Taking advantage of the heavy collisional reduced mass, we treat the translational motion in **R** classically using a self-consistent field approach.[12] The Ar+HF potential is made time-dependent through the translational coordinate, $V(\mathbf{R}(t),\mathbf{r})$. The time evolution of the system is calculated using the method of variation of parameters.[13] The approach is very similar to the traditional Impact Parameter method proposed by Mott[14] and by Bates.[15] However, we make no simplifying assumption for the classical trajectory. Such "classical path" models have been used extensively in the past and several excellent reviews of the subject are available.[16]

While the disadvantages of a mixed dynamics approach are well known,[16,17] we feel they are outweighed by the advantages for this particular case. Since the energy spacing of the HF(j=0) and HF(j=1) states is relatively small (41.12 cm^{-1}) compared with the translational energy (1089 cm^{-1}), the lack of energy conservation in the classical coordinate was not found to be of great significance. While the translational degree of freedom could certainly have been treated using wavepacket methods, it is not clear that the considerable increase in computational effort would have significantly affected the outcome of the full calculation. Finally, we did attempt a fully consistent calculation using the Miller-Marcus semiclassical S-matrix theory.[18,19] However, the difficulties involved in incorporating the necessary phase information were formidable. (A very recent study[20] has, in fact, used this approach to explain quantum effects in Ar + HBr inelastic scattering.) Therefore, while the current approach has known deficiencies, we feel its computational ease, in combination with the dynamical insight yielded, outweighs these concerns. It should be noted that similar methods have been employed recently with great success in

surface scattering[21] and in predissociation of van der Waals complexes.[22] Mixed dynamics methods have also been used to calculate state-to-state differential cross sections for vibrationally inelastic collisions,[23] and to study fine structure transitions in atom-atom scattering.[24] In considering the validity of the semiclassical model later in this paper (Section III), we will compare the results of the semiclassical dynamics to those from the exact quantum calculations which we carried out earlier.[2]

The classical (Hamilton's) equations of motion of Ar relative to the HF center of mass are given in Cartesian coordinates by:

$$\dot{\mathbf{R}} = \frac{\mathbf{P_R}}{M} \quad ; \quad \dot{\mathbf{P}}_\mathbf{R} = -\left\langle \nabla_\mathbf{R} V(\hat{\mathbf{R}},\hat{\mathbf{r}}) \right\rangle \tag{1}$$

where M is the reduced mass of the collision system and the expectation value is over the angular coordinates of $\mathbf{r} = (r_e,\theta,\phi)$, for HF at a fixed $\mathbf{R}$. The quantum mechanical equations of motion are

$$i\hbar\dot{c}_k(t) = \sum_l c_l(t) V_{kl}(t) \exp\left(i\omega_{kl}t\right) \tag{2}$$

where |l> and |k> denote the rigid rotor states |j,m> and |j',m'>, respectively, $\omega_{kl} = (E_k - E_l)/\hbar$, and $c_l(t) = \left\langle l|\Psi(t)\right\rangle = \left\langle Y_{jm}|\Psi(t)\right\rangle$ are the expansion coefficients. The potential matrix elements, V_{kl}, are given by

$$V_{kl} = \left\langle k\left|V\left(\hat{\mathbf{R}},\hat{\mathbf{r}}\right)\right|l\right\rangle \tag{3}$$

This becomes $V_{kl}(t)$ through the time dependence of $\mathbf{R}$ from eq.(1).

In this study we focus on transitions from initial state j=0, m=0 to final states j'. Since we are concerned only with

level-to-level transitions, the probability of scattering into the j' rotational level, as a function of time, is given by

$$P_{j'}(t) = P_{0\rightarrow j'}(t) = \sum_{m'=-j'}^{j'} \left| \langle j'm' | \Psi(t) \rangle \right|^2 \qquad (4)$$

At a given impact parameter, b, a classical trajectory was started at large distance from the diatom and allowed to evolve to large times. For each b, the final scattering angle, θ, given by $\theta=\arccos(\mathbf{P}_R(t=0)\cdot\mathbf{P}_R(t=\infty))$, is obtained along with the level-to-level quantum mechanical transition probability, $P_{j'}(t\rightarrow\infty;b)$. Since we are dealing with heavy scattering particles, differential cross sections are calculated using the classical deflection function, $\theta(b)$, and $P_{j'}(b)$ using the equation

$$\frac{d\sigma_{j'}(\theta)}{d\varpi} = \frac{1}{\sin\theta} \sum_i b_i \left| \frac{d\theta}{db} \right|_{b_i}^{-1} P_{j'}(b_i) \qquad (5)$$

As in the standard classical treatment of elastic scattering,[25] the sum is over all impact parameters which contribute to the same value of θ. $P_{j'}(b_i)$ is the quantum mechanical probability of finding the system in the final rotational state, j' for each such impact parameter b_i. The errors involved in this approximation have been discussed previously.[26] In particular, the greatest sacrifice is the loss of interference information between the partial waves at each orbital angular momentum. For instance, rainbow scattering will be represented by, at best, a primitive semiclassical picture, in which the DCS at the rainbow angle shows a singularity.[27] Furthermore, such features as diffraction oscillations will not be observed. Since the latter phenomenon is not yet experimentally resolvable, its loss is not significant for the present analysis. As will be

shown in Section III, the quantum features observed in the DCS for j'=0 and 1 do not arise from this type of interference.

B. Classical Mean Field Trajectory Method

In order to compare the purely classical time evolution of the system with that of the semiclassical method just discussed, we use the classical mean field technique.[28] Rather than computing several trajectories with random initial orientation individually and averaging to obtain the desired scattering data,[29] a "swarm" of trajectories are run simultaneously at a single impact parameter. This swarm randomly samples the initial diatom orientation space, as required for an atom-rigid rotor collision. The equations of motion for the mean field trajectories are

$$\dot{\mathbf{p}}_{\mathbf{r}_i} = -\nabla_{\mathbf{r}} V(\hat{\mathbf{R}}, \hat{\mathbf{r}}_i) \quad ; \quad \dot{\mathbf{r}}_i = \mathbf{p}_{\mathbf{r}_i}/\mu \qquad (6a)$$

$$\dot{\mathbf{P}}_{\mathbf{R}} = -\left\langle \nabla_{\mathbf{R}} V(\hat{\mathbf{R}}, \hat{\mathbf{r}}) \right\rangle_{\mathbf{r}} \quad ; \quad \dot{\mathbf{R}} = \mathbf{P}_{\mathbf{R}}/M \qquad (6b)$$

where the subscript i denotes the i^{th} classical trajectory. The symbol $\langle\rangle_{\mathbf{r}}$ in eq.(6b) denotes the ensemble average over each trajectory in the swarm. As before, M is the collisional reduced mass and μ is the diatom reduced mass. The vectors $\mathbf{r}_i$ and $\mathbf{p}_{\mathbf{r}_i}$ are the diatom displacement and momentum, respectively. By propagating the relative motion in the mean field of the potential, we ensure that the only difference between the dynamics of the mean field trajectory and the semiclassical methods is the quantum nature of the rotational state evolution.

During the course of integrating the trajectory swarm, the current "rotational state" of the diatom may be calculated for each of the individual trajectories by the

relation

$$\hbar\tilde{\mathbf{j}}_i = \mathbf{r}_i \times \mathbf{p}_{r_i} \tag{7}$$

where $\tilde{\mathbf{j}}_i$ is the continuous rotational angular momentum of the diatom of the i^{th} trajectory. By using an appropriate binning method, one can determine the rotational state probability of the classical system at any time, t. The i^{th} trajectory contributes to the j^{th} rotational bin if $j-\frac{1}{2} \le \left|\tilde{\mathbf{j}}_i\right| < j+\frac{1}{2}$. The classical rotational state probability, $\mathcal{P}_j^{cl}$, is given by

$$\mathcal{P}_j^{cl}(t;b) = \frac{N_j(t)}{N} \tag{8}$$

where N is the total number of trajectories in the swarm at a given b (typically N=100) and $N_j(t)$ is the number of trajectories in the j^{th} bin at some time, t.

The classical opacity function is given by $\mathcal{P}_j^{cl}(t;b)$ as $t\rightarrow\infty$. The classical DCS are calculated by eq.(5), just as are the semiclassical DCS, only now we use the classical opacity function, $\mathcal{P}_j^{cl}(b)$. This permits a direct comparison between the classical and semiclassical models of the scattering dynamics.

III. RESULTS AND DISCUSSION

Classical and semiclassical deflection functions and opacity functions for j'=0, 1, and 2 are shown in figure 1. The classical and semiclassical deflection functions are so close that any differences in the corresponding DCS must be due almost exclusively to their opacity functions. The lower two panels of figure 1 do indeed show striking differences between them. The semiclassical results show weak probabilities into $j' \ge 2$, so that the j'=0 and j'=1

probabilities are almost "mirror images" of each other. This is most clearly seen in the oscillatory structure for the impact parameter range of b~3-8 bohr. In contrast, the classical results show no such strong coupling between the j'=0 and j'=1 states, and there is no similar oscillatory structure at all; the classical opacity function for j'=0 shows essentially a monotonic increase of $\mathcal{P}^{cl}(b)$ for b>4 bohr.

The semiclassical cross sections obtained from equation 5 are shown in figure 2. They are also compared with the purely classical calculations, and with the "exact" quantum close-coupled DCS obtained earlier.[2] It is immediately clear that the semiclassical DCS qualitatively reproduce all features of the close-coupled DCS except for the j=0→j'=1 DCS below θ=20°. We will discuss the DCS in this angular region later in this section. We now concentrate on the j=0→j'=0 "shoulder" and the j=0→j'=1 "hole" features near θ=60°, which we identified in an earlier publication as quantum mechanical in origin[2]. From figure 1, we can see that this scattering angle corresponds to an impact parameter of b~4.5 bohr. This is just where the semiclassical 0→0 probability goes through a local maximum, with a corresponding minimum in the 0→1 probability. The 0→0 shoulder and 0→1 hole therefore are seen to be complementary features that are present in the CC and semiclassical dynamics, but altogether absent at the fully classical level. The order-of-magnitude difference between the classical and close-coupled DCS of figure 2 is a consequence of the divergence of the classical and semiclassical opacity functions in the narrow range of impact parameters near b~4.5 bohr.

Using the classical relation ℓ=Mvb (where ℓ is the orbital angular momentum and v is the collision velocity), the range of impact parameters near b~4.5 bohr corresponds to ℓ~70$\hbar$. Because so little angular momentum is due to the HF rotation, the region of greatest interest is for total

angular momenta near $J=70\hbar$. This is just where the CC calculations show their greatest sensitivity to the potential energy surface.[2] The quantum effects identified earlier also arise from this J range.[2] The correspondence between the CC and semiclassical results in this range of J's and b's arises because of the quantum treatment of the HF rotor in the semiclassical model. This suggests that the potential surface, in its role of coupling the rotational states, makes significant contributions to both the existence and location of these quantum features. Conversely, such features in the DCS should provide valuable information on the exact nature of the potential energy surface.

Returning now to the region of scattering angles below $\theta=20°$, we see virtually perfect agreement between the semiclassical and CC results for the $j'=0$ DCS, in contrast to a very strong peak in the classical DCS at $\theta=13°$. The latter is clearly identified with the minimum seen for the classical deflection function in figure 1(a), yielding a classical rainbow infinity due to the $\left|d\theta/db\right|^{-1}$ factor in equation 5. Although the semiclassical calculation shares this minimum in the deflection function, the $0\rightarrow0$ probability in figure 1(b) is so low that the rainbow is quenched, beautifully reproducing the close-coupled DCS. A consequence of the $0\rightarrow0$ minimum in the semiclassical probability is the $0\rightarrow1$ maximum, which therefore produces a pronounced maximum in the semiclassical $j'=1$ DCS. The inelastic $0\rightarrow1$ rainbow has essentially completely quenched the elastic $0\rightarrow0$ rainbow, thus preventing observation of a strong rainbow in the rotationally unresolved DCS experiments of Vohralik, et al.[7] That this rainbow is shifted to a larger scattering angle relative to the close-coupled DCS is known from other comparisons of primary rainbows in classical and quantum mechanics.[30]

The above discussion allows assignment of the feature near $|\theta|=10°$ as an ℓ-type rainbow.[6,31] The sudden drop of signal from the "bright" to the "dark" side of the rainbow beyond $|\theta|=13°$ in the classical and semiclassical DCS is also well known.[27] It is due to three impact parameter contributions to equation 5 for $|\theta|<13°$ switching to only one contribution for $|\theta|>13°$.

In our earlier publication,[2] we also gave close-coupled DCS for scattering of Ar+DF(j=0)→Ar+DF(j'=0,1) for comparison to the HF scattering. Figure 3 displays such a comparison for the present semiclassical results. Away from the rainbow region, we find again that the semiclassical results are very similar to the CC cross sections (not shown here). In particular, the striking dissimilarities between Ar+DF and Ar+HF scattering are reproduced faithfully. The "shoulder" at $\theta=60°$ for HF(j'=0) is replaced by a "dip" near $\theta=30°$ for DF; similarly the HF(j'=1) dip becomes a shoulder for DF(j'=1). We seek an explanation for these changes in the opacity functions for Ar+DF scattering.

Figure 4 shows a comparison of Ar+DF and Ar+HF opacity functions. Since the translational reduced mass is hardly affected by the H→D isotopic substitution, there is relatively little change in the classical deflection function, which remains indistinguishable from that shown in figure 1(a). Examination of the opacity functions reveals them to be qualitatively similar to the HF results. The probabilities for Ar+DF are also oscillatory and the 0→0 and 0→1 opacity functions still mirror each other, despite larger probabilities for Ar+DF(j'≥2). However, the 0→0 maximum has shifted to lower impact parameters, from b~4.5 to b~3.6 bohr, and has broadened, moving the Ar+DF shoulder substantially outward in scattering angle (and significantly weakening it). Simultaneously, there is very little 0→0 probability in the entire impact parameter range of b~5-7 bohr, corresponding to

the DCS minimum seen near θ~30°. The Ar+DF 0→1 opacity function no longer has a minimum at b~4.5 bohr, so there is no "hole" like that seen in the DCS for Ar+HF scattering. Instead, the monotonic 0→1 probability for b in the range 3.0-7.0 bohr fills in the entire DCS for Ar+DF scattering from θ~30°-90°. It is seen that shifts in the details of the opacity functions for Ar+DF scattering are sufficient to completely alter the DCS shown in figure 3.

Excellent agreement between the semiclassical (classical path) results and close-coupled DCS (Figure 2) justifies the use of the former approach. We now utilize the time-dependent aspect of these calculations to investigate the role played by the potential in producing the DCS shown in figures 2 and 3. To that end, we introduce a model calculation for the insight it yields into the details of the collision dynamics.

IV. THE ROLE OF THE INTERMOLECULAR POTENTIAL: MODEL CALCULATION

To exploit the full power of the semiclassical method, we now utilize the time-dependent aspect of the calculation to explore the scattering dynamics. In figure 5 we show the quantum mechanical time evolution of $P_{j'}$ for various impact parameters. It is clear that there is strong coupling between the j=0 and 1 states at all times; indeed it is the $t\rightarrow\infty$ manifestation of this coupling which is observed in the semiclassical opacity functions of figure 1. At high impact parameter, this coupling is not surprising since, as observed above, states with j'>1 have little probability; that is, P_0 and P_1 sum to approximately unity. At low impact parameter, higher j' states are populated, but the sum of their probabilities is essentially decoupled from the j'=0 and 1 probabilities. For clarity, the probabilities into other

states are not shown in figure 5. However, no obvious coupling pattern was observed for these higher rotational states.

Noting the coupling between the j=0 and 1 rotational states, we attempt to examine the dynamics of the rotational energy exchange using a simplified two-state model. We choose these states to be |0,0> and |1,0>. The justification for this choice will be given in some detail later. The potential matrix elements $\left\langle 0,0\left|V\left(\mathbf{R}(t),\hat{\mathbf{r}}\right)\right|0,0\right\rangle = V_{00}(t)$ and $\left\langle 0,0\left|V\left(\mathbf{R}(t),\hat{\mathbf{r}}\right)\right|1,0\right\rangle = V_{01}(t)$ are shown in figure 6 for several impact parameters. Since all the diagonal matrix elements, <k|V(t)|k>, are similar (not shown in figure 6), we set $V_{11}=V_{00}$ in our model calculation. Also, since $V_{01}(t)$ is much less than $V_{00}(t)$, but qualitatively similar in form, we model $V_{01}(t)$ as $\varepsilon V_{00}(t)$, where ε is a constant less than 1. Finally, we impose the energy sudden approximation by setting $\omega_{01}=0$, corresponding to degenerate rotational energy levels. In this model the quantum equations of motion, given for the full system in equation 2, reduce to

$$i\hbar\dot{c}_0(t) = V_{00}(t)\left[c_0(t) + \varepsilon c_1(t)\right] \tag{9a}$$

$$i\hbar\dot{c}_1(t) = V_{00}(t)\left[\varepsilon c_0(t) + c_1(t)\right] \tag{9b}$$

These simplifications allow us to examine several different coupling cases (weak, intermediate and strong) through the variation of a single parameter, ε, which is a measure of the potential energy coupling between the rotational states. We employ the initial conditions $c_0(0)=1$ and $c_1(0)=0$. The relative collision energy is 135 meV, as was used in the full treatments. The $V_{00}(t)$ are taken from these runs.

Using this two-state model the internal state dynamics

reduces to the time evolution of the coefficients, $c_0(t)$ and $c_1(t)$. We plot trajectories of these expansion coefficients in the complex plane in figures 7-9 for various values of b and ε. In order to gain insight into the meaning of these plots, we note first that for $\varepsilon=0$ (i.e. no coupling between j=0 and 1) the equations of motion, eqs.9, become

$$\dot{c}_i = \frac{-ic_i V_{00}}{\hbar} \qquad (i = 0,1) \tag{10}$$

By writing $c_i=|c_i|\exp(i\phi_i)$, where $\phi_i=\arg(c_i)$, substituting into eq.10, and equating the real and imaginary parts we obtain:

$$\frac{d}{dt}|c_i| = 0 \quad ; \quad \frac{d}{dt}\phi_i = \frac{-V_{00}}{\hbar} \tag{11}$$

with the explicit result that

$$c_i(t) = c_i(0)\exp\left(-i\int_0^t dt' V_{00}(t')/\hbar\right) \tag{12}$$

gives the time-evolution for the states. The integral in eq.12 is known as the action integral. Thus motion in the $\varepsilon=0$ case is pure rotation in the complex plane. A negative V_{00} leads to counter-clockwise rotation in the complex plane; a positive V_{00} gives clockwise rotation.

Consider next the effect of the off-diagonal terms in eq.(9). In general, if c_i is itself negligible, then the time evolution of c_i is governed by the present value of c_j ($j\neq i$). The equations of motion reduce to

$$\dot{c}_i(t) = (i\hbar)^{-1}\varepsilon\, V_{00}(t)c_j(t) \qquad (j\neq i) \qquad (13)$$

or

$$\delta c_i(t) = \dot{c}_i(t)\delta t = \left(\delta t\hbar^{-1}\varepsilon\, V_{00}(t)\left|c_j(t)\right|\right)\exp\left[i\left(\phi_j - \pi/2\right)\right]$$
$$= \left\{\delta t\hbar^{-1}\varepsilon\left|V_{00}(t)\right|\left|c_j(t)\right|\right\}\exp\left[i\left(\phi_j - \frac{\text{sign}(V_{00}(t))\pi}{2}\right)\right] \qquad (14)$$

The term within the braces{} is always positive. Thus, the change in c_i due to a nonzero c_j is a complex number rotated $\pi/2$ from c_j either clockwise or counter-clockwise depending on the sign of V_{00}. The amplitude of δc_i is, of course, governed by ε.

The easiest plots to analyze are those for the large impact parameter case. For b≥6 bohr, V_{00} is never positive (see figure 6), and therefore the sense of rotation in the complex plane is always counter-clockwise. This is clearly shown for b=6.0 bohr in figure 7-9(c). Here $c_0(0)=(1,0)$ and c_0 spirals inward as a function of time. Simultaneously, c_1 spirals outward from (0,0). Since $V_{00}(t)$ is always negative, the rotation is counter-clockwise. The points on the figures are sampled at evenly-spaced time steps. Thus, the separation of points indicates the rate of rotation in the complex plane, and hence, the magnitude of V_{00}. At first closely spaced, the points become more widely spaced as the classical trajectory samples the most attractive part of the potential. Then the spacing closes up as $|V_{00}|$ approaches zero near the classical turning point. The attractive well region is traversed again as the particles separate, resulting in acceleration and finally, as R becomes large, deceleration of the angular motion in the complex plane. At this impact parameter, it can also be seen that the classical turning point occurs near $c_0=(-1,0)$ for the low (ε=0.1) and intermediate (ε=0.2) coupling cases.

The effect of changing ε can be seen be comparing the

panels for ε=0.1, 0.2, and 0.5 at the same value of b. The effect is particularly obvious at high b (figures 7-9(d)). Clearly ε controls the radial velocity at which c_1 spirals out from (0,0). Note that at times near t=0, when $c_0 \approx (1,0)$ that δc_1 lies along (0,1); that is, δc_1 is rotated $\pi/2$ radians counter-clockwise from c_0, as predicted by eq.(14).

As is clear from figure 6, the magnitude of $V_{00}(t)$ decreases as the impact parameter increases from 6 bohr to 10 bohr. The role of the V_{00} potential in the dynamics is seen by examination of figures 7-9, panels (c) and (d). The smaller the magnitude of $V_{00}(t)$, the less c_0 rotates from its starting value of (1,0). Therefore, for b=10 bohr, we see c_0 rotates only 60°, compared with the 350° rotation attained for b=6 bohr, in the weak and intermediate coupling cases. (The pattern in the strong coupling case, ε=0.5, is as might be expected, more complicated and will be discussed later.)

Since the sense of rotation of c_1 is also governed by V_{00},
it is not surprising that the modulus of c_1 is influenced by the magnitude of V_{00}; the more "time" available for rotation in the complex plane, the farther c_1 can spiral out from the origin. In both the ε=0.1 and ε=0.2 cases, this can be seen by comparing panels (c) and (d) of figures 7-9. In the b=6 bohr case, c_1 has "time" to spiral outward, and reach a significant nonzero value of $|c_1|$; for b=10 bohr, this is not the case. Thus, the magnitude of the V_{00} potential is a significant factor in determining the transition probability. The ability to rotate about the origin is a measure of the strength of the potential. It is closely related to the action, $\int V_{00}(t)\,dt$. In Table 1 we compare this measure of the rotation, $\arg(c_0(\infty))$, and the action. (Note that the arguments given in Table 1 are not modulo 2π; rotation in the complex plane often goes onto neighboring Riemann sheets. The branch cut is

along the real axis.) Clearly, both these measures diminish as b increases past 8 bohr. As can be seen from figure 10 this is precisely the range of b values for which the $0 \rightarrow 1$ transition probability monotonically decreases.

These panels also illustrate the effect of increasing ε. Clearly from eq.(14), ε gives a measure of the radial component of the motion. For b=10 bohr, for example, the "total rotation" (action) is the same in all cases, but the magnitude of the radial motion clearly scales with ε.

Examination of the opacity functions (figure 10) for varying values of ε illustrates the effect of ε in coupling the two states as $t \rightarrow \infty$. As ε is increased, the strength of the coupling between $|0\rangle$ and $|1\rangle$ is increased. This coupling appears as an oscillation in the opacity functions. The weakly coupled system (ε=0.1), shows only a slight oscillation in the opacity functions. By the time we get to the very strong coupling case (ε=0.5) the opacity functions are oscillating wildly. The origin of this strong oscillation can be gleaned from the figures 7-9. In particular, consider figure 9(c). As in figures 7(c) and 8(c), V_{00} controls the angular motion and ε controls the radial motion. In this particular case, though, the coupling is so strong that c_0 initially spirals very rapidly toward the origin. As the counter-clockwise rotation continues, it loops back on itself in the upper half of the plane, and spirals back out to a large $|c_0|$. Clearly, then for large ε, such closed loops will lead to a dynamics highly sensitive to the exact details of the potential.

Let us now examine the evolution of $c_0(t)$ and $c_1(t)$ at the lower impact parameters. It can be seen in figures 7-9(a) and (b) that for b<6.0 bohr, the rotation of $c_0(t)$ reverses its direction during the collision. This is evidently the result of encountering the repulsive part of the potential.

This reversal, as we pass from the attractive region to the repulsive on the incoming part of the trajectory, and the retracing of its path on the outgoing part, has the effect of bringing $c_1(t)$ back toward the origin. That is, at lower values of b the repulsive part of the potential favors the transition 0→1, but the attractive part of the potential after the turning point forces the system back into j'=0. However, as b becomes sufficiently large, V_{00} has no repulsive component. There is therefore no reversal of direction; hence no tendency for c_1 to reverse back toward the origin. At these intermediate impact parameters (b=5-7 bohr) the attractive part of the potential favors the 0→1 transition, and we see the continuing outward spiral of the $c_1(t)$ coefficient.

The actual average value of V_{01}/V_{00} for the H6 potential (see figure 6) is near 0.2, where the opacity function behaves much less dramatically than in the ε=0.5 case. In fact, the model calculations for ε=0.2 nicely reproduce many of the features seen in the opacity functions for the full calculation. Therefore, we will use the model data for ε=0.2 to discuss the opacity functions of figure 1(b). The opacity function of figure 10(b) is qualitatively similar to that for the semiclassical data in figure 1(b). This semi-quantitative agreement between the asymptotic results of the two-state model and the full run is our justification (albeit empirical) for the use of the model. By following detailed dynamics in several cases, we have established that the model is reasonable in the sense that $P_0(t)$ in the model and full calculations are qualitatively similar for the appropriate choice of coupling parameter.

The reason for the peak in the opacity function for j'=0 at b=4.0 bohr in the model calculation can be understood by examination of figure 8(b). It can be seen from this figure that the $c_0(t)$ returns to (1,0) twice during the collision. In fact it is clear that the net action for this

trajectory is almost exactly zero. That is, at this impact parameter the attractive and repulsive parts of the potential exactly balance each other on the incoming and outgoing portions of the classical path. We can see that initially $c_0(t)$ rotates counter-clockwise until the repulsive part of the potential is reached. At this point $V_{00}(t)$ becomes positive and $c_0(t)$ retraces its initial path. The rotation of $c_0(t)$ continues to a point conjugate to the position where the repulsive part of the potential was entered. As the trajectory goes back into the attractive part of the potential, the cycle is completed by $c_0(t)$ retracing its path once more back to (1,0). It is this balancing between the attractive and repulsive parts of the potential (and the consequent peak in P_0) that is responsible for the quantum feature seen near θ=30-60° in the DCS for the full system. The generality of this zero action trajectory is apparent from examination of the $c_0(t)$ for ε=0.1 and 0.5 (Figures 7 and 9 (b)). In all cases the balance between the attractive and repulsive part of the potential is observed and the trajectory retraces itself and returns to its t=0 value.

Although the model calculation with ε=0.2 reproduces the full semiclassical data reasonably well at the level of the opacity function (figure 10(b)), requiring that the full calculation and the model agree as a function of time is more demanding. We therefore compare coefficients from a full run using eq.(2) (figure 11) with those from the model calculation (figure 8). Clearly, from figures 8 and 11 (c) and (d), one difference is that $c_1(t)$ "rotates" farther in the full calculation. This is due to the presence of the ω_{01} term in the latter. Rewriting eq.(2) for a two-level system yields:

$$i\hbar\dot{c}_0(t) = c_0(t)V_{00}(t) \qquad +c_1(t)V_{01}(t)\exp\left(i\omega_{01}t\right)$$

(15a)

$$i\hbar\dot{c}_1(t) = c_0(t)V_{01}(t)\exp\left(-i\omega_{01}t\right) + c_1(t)V_{11}(t)$$

(15b)

Following our earlier analysis, for $V_{01}=0$ we find that, $c_i(t) = c_i(0)\exp\left(-i\int_0^t dt' V_{ii}(t')/\hbar\right)$. Therefore, the overall rates of rotation in the complex plane are not affected by the ω_{01} term.

On the other hand, if the effect of the diagonal terms is ignored, then the eqs.(15) simplify to :

$$i\hbar\dot{c}_0(t) = c_1(t)V_{01}(t)\exp\left(i\omega_{01}t\right)$$

(16a)

$$i\hbar\dot{c}_1(t) = c_0(t)V_{01}(t)\exp\left(-i\omega_{01}t\right)$$

(16b)

yielding a change, δc_i, (*c.f.* eq.(14)):

$$\delta c_i(t) = \left\{\delta t\hbar^{-1}\left|V_{01}(t)\right|\left|c_j(t)\right|\right\}\exp\left[i\left(\phi_j - \text{sign}\left(V_{01}(t)\right)\frac{\pi}{2} \pm \omega_{01}t\right)\right] \qquad (17)$$

where the plus(minus) sign applies for i=0(1). One effect of this is to change the initial sense of rotation of $c_1(t)$. The initial motion of $c_1(t)$ is now no longer along (0,1), but pushed somewhat into the second quadrant. This explains why c_1 "rotates" farther in the full dynamics. This is confirmed by comparing figures 8 and 11. On the whole, while it is clear that reinstating all the terms in the dynamics produces quantitative changes, the qualitative behavior - even at this detailed level - is still very similar.

Clearly, the model calculation has simplified the true inter-state coupling and neglected the ω_{01}. However, the insight gained from this model has exciting implications. The

potentials $V_{00}(t)$ and $V_{01}(t)$ can be parameterized. (In fact they are often known extremely accurately for the attractive part of the potential.) If the $V_{00}(t)$ potential is known, then the elastic scattering problem can be solved by standard methods,[32] yielding both $\theta(b)$ and $R(t)$ for each impact parameter. The traditional route to inversion of potentials in elastic scattering[33] is to first assume a parameterized $\theta(b)$, then to use semiclassical methods to obtain the differential cross section. The classical deflection function is then optimized to give the best fit to the observed DCS. Finally, the $\theta(b)$ is inverted to obtain the potential. Our approach reduces the many-state problem to a series of elastic problems. Inverting eq.(5) allows one to extract the opacity functions for each j state, at least for θ values beyond the rainbow. The parameterized potentials can then be optimized to obtain the best fit to the experimental data using eqs.(9a) and (9b). The insight gained from the use of eqs.(9) can guide the adjustment of the parameters. The advantage of this method for potential inversion is that each coupling element can be adjusted independently of all others. Clearly, the advantage of such a semiclassical framework for inversion is that the coupling can be optimized at each separate θ. A recalculation of the DCS using close coupling methods would require a new global solution of the DCS for each change in the potential. Furthermore, an inspection of the time evolution of the system is intuitively appealing, and the contribution of each part of the potential can be readily assessed.

V. CONCLUSIONS

We have used a semiclassical (classical path) approximation to investigate the quantum dynamics of Ar + HF($j=0\rightarrow j'=0,1$) on the Hutson H6 potential.[3] We were able to reproduce previous DCS obtained from close-coupled calculations. The time-dependent approach is readily

implemented using the semiclassical approximation offering an intuitive appeal which is often more difficult to cull the time-independent CC calculations. (Recent work by Alexander[34] has suggested a new representation of time-independent data which could probably furnish most of the mechanistic details described here.) In particular, it is often easier to visualize the influence of the potential on the dynamics when its contributions are localized in time. In an earlier publication,[2] we were only able to analyze whether a given potential feature was important or not by comparing CC calculations in the presence of and in the absence of that feature. For instance, by artificially making the repulsive wall isotropic, it was observed that the dip in the $0 \rightarrow 1$ DCS disappeared. From this it could be inferred that the repulsive anisotropy was crucial for the observation of all aspects of the quantum features, but the extent of the competing contributions of the repulsive and attractive anisotropy could not be clearly gauged. In contrast, the time-dependent picture allows us to "see" how the potential affects the dynamics. In particular, plots of the expansion coefficients, $\left\langle Y_{jm} \middle| \Psi(t) \right\rangle$, in the complex plane seem to represent a significant step forward in allowing us to determine the exact nature of the contribution of each region of the surface to the scattering dynamics.

Furthermore, for this particular system, it was found that all the qualitative features of the dynamics could be reproduced by considering the dynamics of two rotor states only: $|0,0\rangle$ and $|1,0\rangle$. Thus the effect of the potential could be reduced to that of the coupling matrix elements V_{00} and V_{10}. Using this two-state model, we were able to rationalize the features observed in our previous paper.[2] Essentially, the quantum feature seen previously is due to the existence of an impact parameter for which the trajectory experiences an

overall balance between the attractive and repulsive parts of the potential, resulting in a net zero action. For this trajectory, the collision is found to be asymptotically elastic, returning all flux to $j'=0$. Therefore, at this impact parameter, the $0\rightarrow 0$ probability (and consequently the differential cross section) goes through a maximum. Probability conservation, of course, ensures a minimum probability into all other channels - particularly $0\rightarrow 1$ at this impact parameter.

This has implications for the "inversion" of a potential surface from experimental scattering data. A clear intuitive grasp of the role played by each part of the potential is a great aid in guiding the adjustment of a parameterized potential in order to improve agreement with experimental input. In particular, it seems that the technique we have explored here shows very distinctively the contrasting effects of attraction and repulsion. While the attractive region of the potential energy surface of van der Waals molecules is often well characterized by potentials derived from spectroscopic data,[3] the repulsive wall is usually much more obscure, and often obtained by extrapolation of bound state data.[3,35] However, we envisage being able to employ the techniques explored here to systematically investigate the effect of small changes in the repulsive wall, with the goal of improving qualitative agreement with scattering data. Used in conjunction with converged close-coupled results, this could prove a promising approach to obtaining accurate global potential energy surfaces for van der Waals molecules.

REFERENCES

1. L. J. Rawluk, Y. B. Fan, Y. Apelblat, and M. Keil, J. Chem. Phys., **94**, 4205 (1991)

2. L. J. Rawluk, M. Keil, M. H. Alexander, H. R. Mayne, and J. J.C. Barrett, Chem. Phys. Lett., **202**, 291 (1993)

3. J. M. Hutson, J. Chem. Phys., **96**, 6752 (1992)

4. U. Buck, Comments At. Mol. Phys., **17**, 143 (1986)

5. P. L. Jones, U. Hefter, A. Mattheus, J. Witt, K. Bergmann, W. Müller, W. Meyer, and R. Schinke, Phys. Rev. B, **26**, 1283 (1982);
   P. L. Jones, E. Gottwald, U. Hefter, and K. Bergmann, J. Chem. Phys., **78**, 3838 (1983), and references therein.

6. R. Schinke and J. M. Bowman, in *Molecular Collision Dynamics*, edited by J. M. Bowman (Springer, Berlin, 1982), Chap. 4.

7. P. F. Vohralik, R. E. Miller and R. O. Watts, J. Chem. Phys., **90**, 2182 (1989)

8. G. A. Parker and R. T Pack, J. Chem. Phys., **68**, 1585 (1978)

9. J. J.C. Barrett, H. R. Mayne, M. Keil and L. J. Rawluk, Can. J. Chem., (in press, 1994)

10. HIBRIDON is a package of programs for the time-independent quantum treatment of inelastic collisions and photodissociation written by M. H. Alexander, D. E. Manolopoulos, H.-J. Werner, and B. Follmeg, with contributions by P. F. Vohralik, D. Lemoine, G. Corey, B. Johnson, T. Orlikowski, W. Kearney, A. Berning, A. Degli-Esposti, C. Rist, and P. Dagdigian.

11. L. Beneventi, P. Casavecchia, F. Vecchiocattivi, G. G. Volpi, D. Lemoine, and M. H. Alexander, J. Chem. Phys., **89**, 3505 (1988)

12. R. B. Gerber and R. Alimi, Israel J. Chem., **31**, 383 (1991)

13. P.A. M. Dirac, *The Principles of Quantum Mechanic*" (Oxford University Press, 1947), pp.113-125

14. N. F. Mott, Proc. Camb. Phil. Soc. Math. Phys. Sci., **27**, 553 (1931)

15. D. R. Bates, *Atomic and Molecular Processes*, (Academic Press, 1962), Chap.4

16. G. D. Billing, Comp. Phys. Rep., **1**, 237 (1984); W. R. Gentry, *Atom-Molecule Collision Theory*, ed. R. B. Bernstein, (Plenum Press, New York, 1979) pp. 397-401; A. S. Dickinson, Comp. Phys. Comm., **17**, 51 (1979), and references therein.

17. W. H. Miller and S. Shi, J. Chem. Phys., **75**, 2258 (1981)

18. W. H. Miller, Adv. Chem. Phys., **25**, 69 (1974)

19. R. A. Marcus, Chem. Phys. Lett., **7**, 525 (1970); R. A. Marcus, J. Chem. Phys., **59**, 5135 (1973)

20. B.B. Grayce, R.T. Skodje and J.M. Hutson, J. Chem. Phys., **98**, 3929 (1993).

21. B. Jackson, J. Phys. Chem., **93**, 7699 (1989)

22. A. García-Vela and R. B. Gerber, J. Chem. Phys., **97**, 3297 (1992)

23. R. Schinke, H. Krüger, V. Hermann, H. Schmidt, and F. Linder, J. Chem. Phys., **67**, 1187 (1977); C. F. Geise and W. R. Gentry, Phys. Rev., **A10**, 2156 (1974)

24. L.J. Kovalenko, S.R. Leone and J.B. Delos, J. Chem. Phys, **91**, 6948(1989).

25. R. D. Levine and R. B. Bernstein, *Molecular Reaction Dynamics and Chemical Reactivity*, (Oxford University Press, New York, 1987), p. 861

26. M. S. Child, *Molecular Collision Theory*, (Academic Press, London, 1974), pp. 143-144

27. M. V. Berry and K. E. Mount, Rep. Prog. Phys., **35**, 315 (1972)

28. K. Haug and H. Metiu, J. Chem. Phys., **97**, 4781 (1992)

29. M. Karplus, R. N. Porter and R. D. Sharma, J. Chem. Phys., **43**, 3259 (1965)

30. ref. 26, pp. 66-67

31. H. R. Mayne and M. Keil, J. Phys. Chem., **88**, 883 (1984)

32. ref. 25, pp. 141-148

33. U. Buck, Adv. Chem. Phys. **30**, 313 (1975); U. Buck, Rev. Mod. Phys., **46**, 369 (1974)

34. M. H. Alexander, J. Chem. Phys. **95**, 8931 (1991);
ibid **96**,6672 (1992).

35. D. J. Nesbitt, M. S. Child and D. C. Clary, J. Chem. Phys., **90**, 4855 (1989)

Table 1. Comparison of the action along the classical path, $\int V_{00}dt$, and final value of the argument of the c_0 coefficient in the complex plane. Note the "balanced" trajectory, at b=4.0 bohr, has an action and $\arg(c_0)$ of ~0.

b [bohr]	$\int V_{00}dt$ [$\hbar$]	$-\arg(c_0(\infty))$ [radian]
0	0.2676	5.356
2	0.2037	4.192
4	0.0092	0.2161
6	-0.3065	-6.128
8	-0.1882	-3.761
10	-0.0478	-0.9550
12	-0.0167	-0.3314

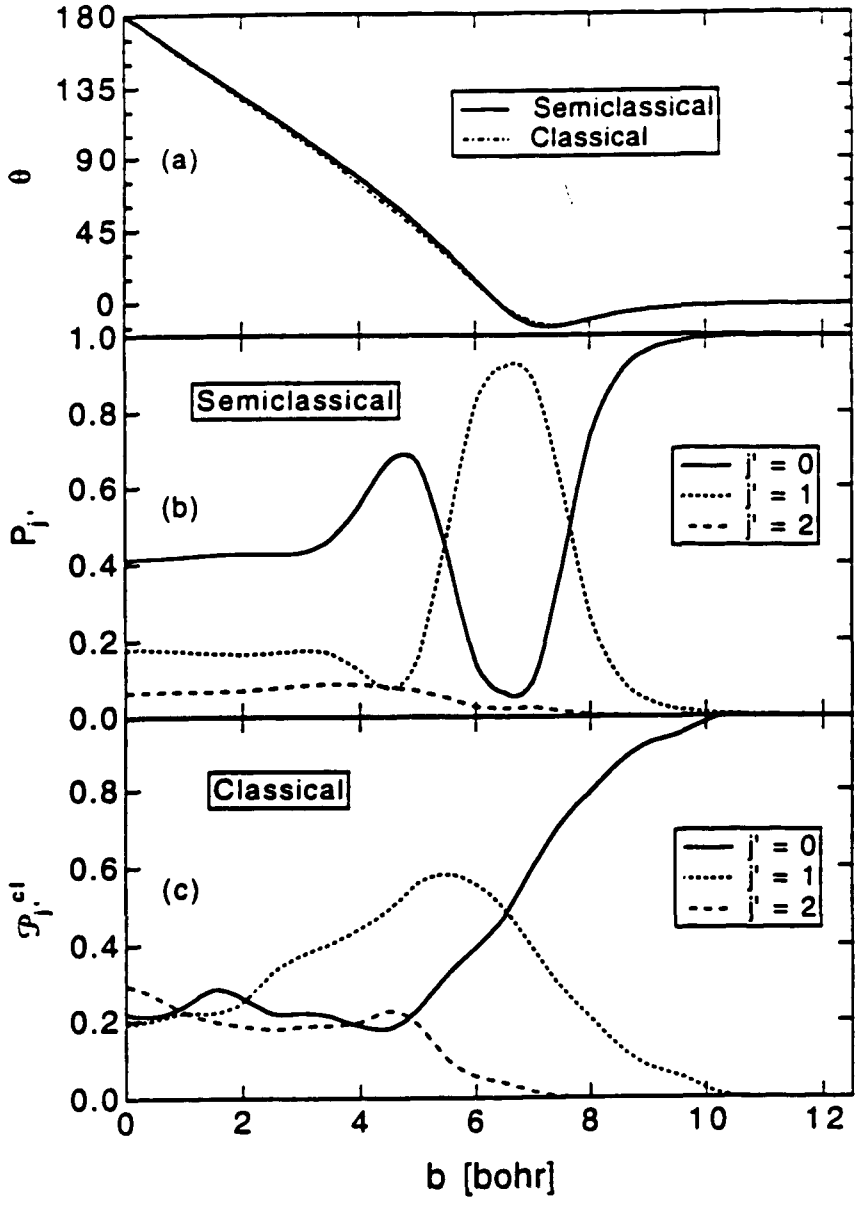

Figure 1. Deflection and opacity functions from semiclassical and classical trajectory calculations. Plotted are: (fig 1(a)) the scattering angle, θ ; (fig 1(b)) semiclassical final rotational state probability, $P_{j'}$; and (fig 1(c) classical final rotational state probability $\mathcal{P}_{j'}^{cl}$, as a function of the impact parameter, b. The initial rotational state is $|j=0, m=0\rangle$. Relative collision energy is 135 meV.

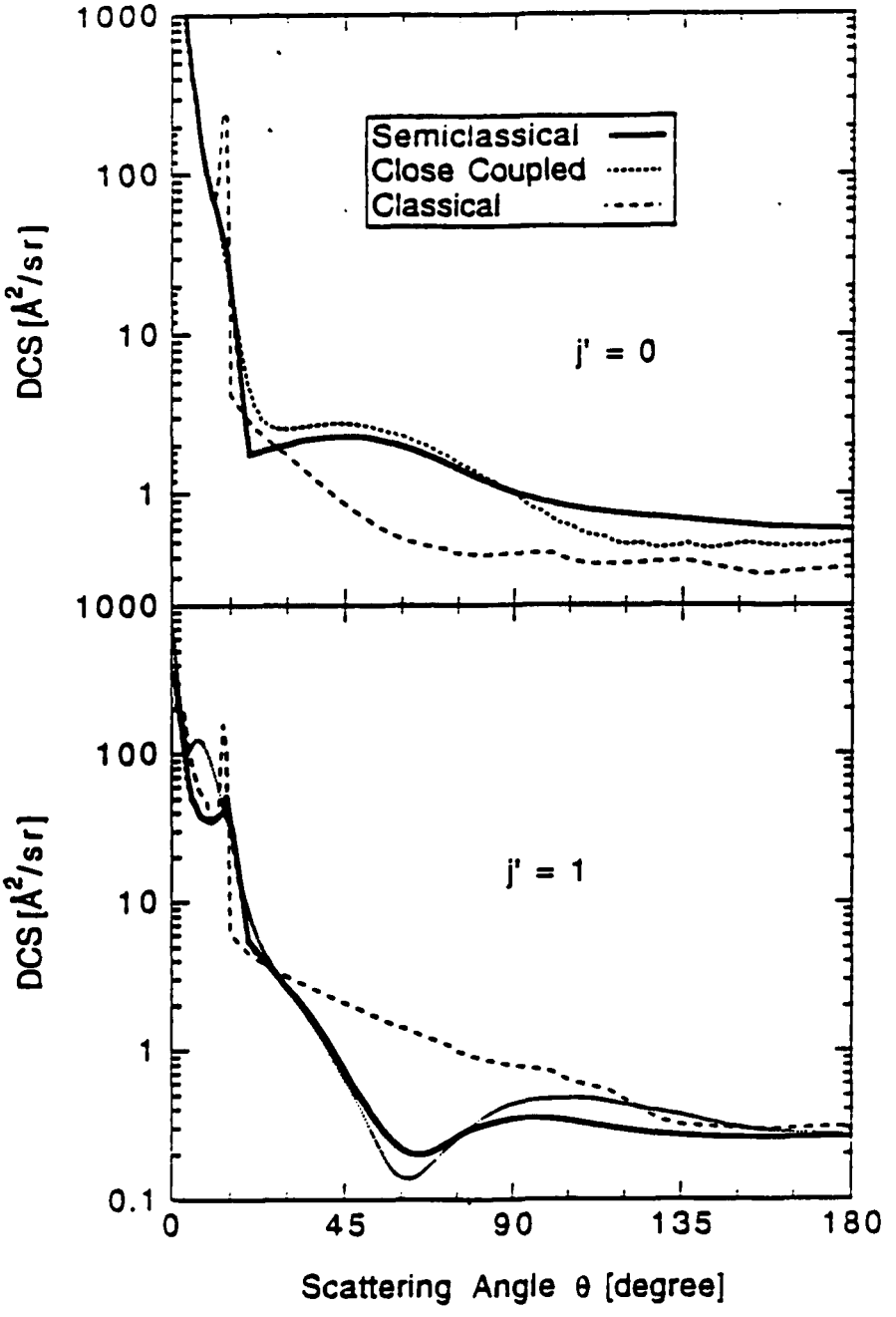

Figure 2. Differential cross section (DCS) from converged close coupled (reference 2), semiclassical, and classical calculations for final rotational states j'=0 and j'=1.

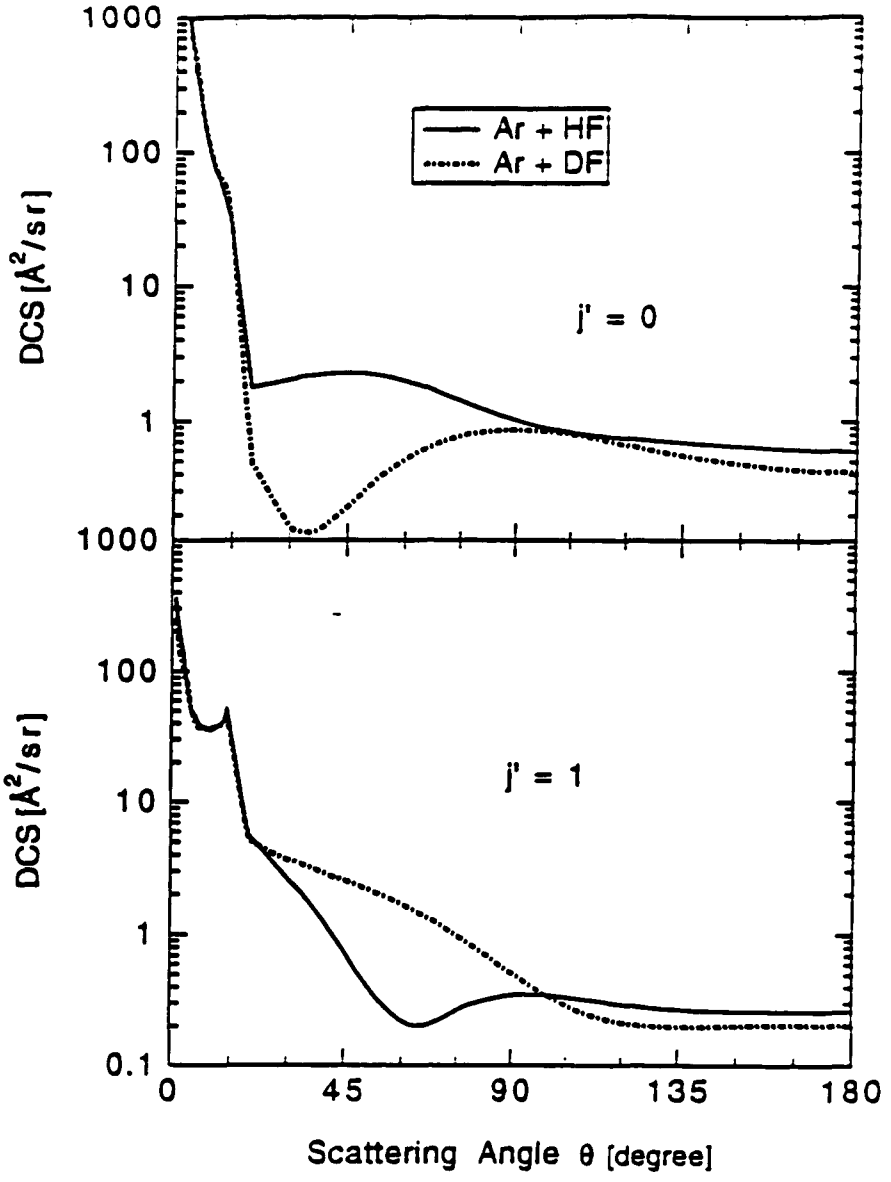

Figure 3. Differential scattering cross sections for Ar+HF and Ar+DF. Initial rotational state and collision energy are the same as those in figure 1. Only the semiclassical results are shown.

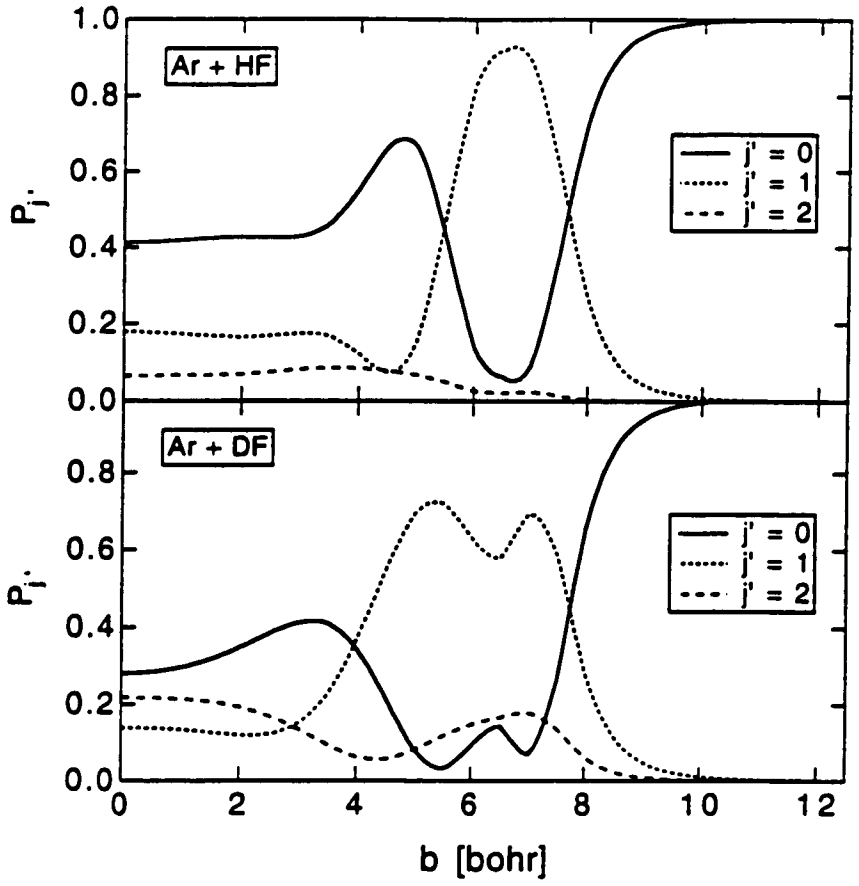

Figure 4. Opacity functions for Ar+HF and Ar+DF.

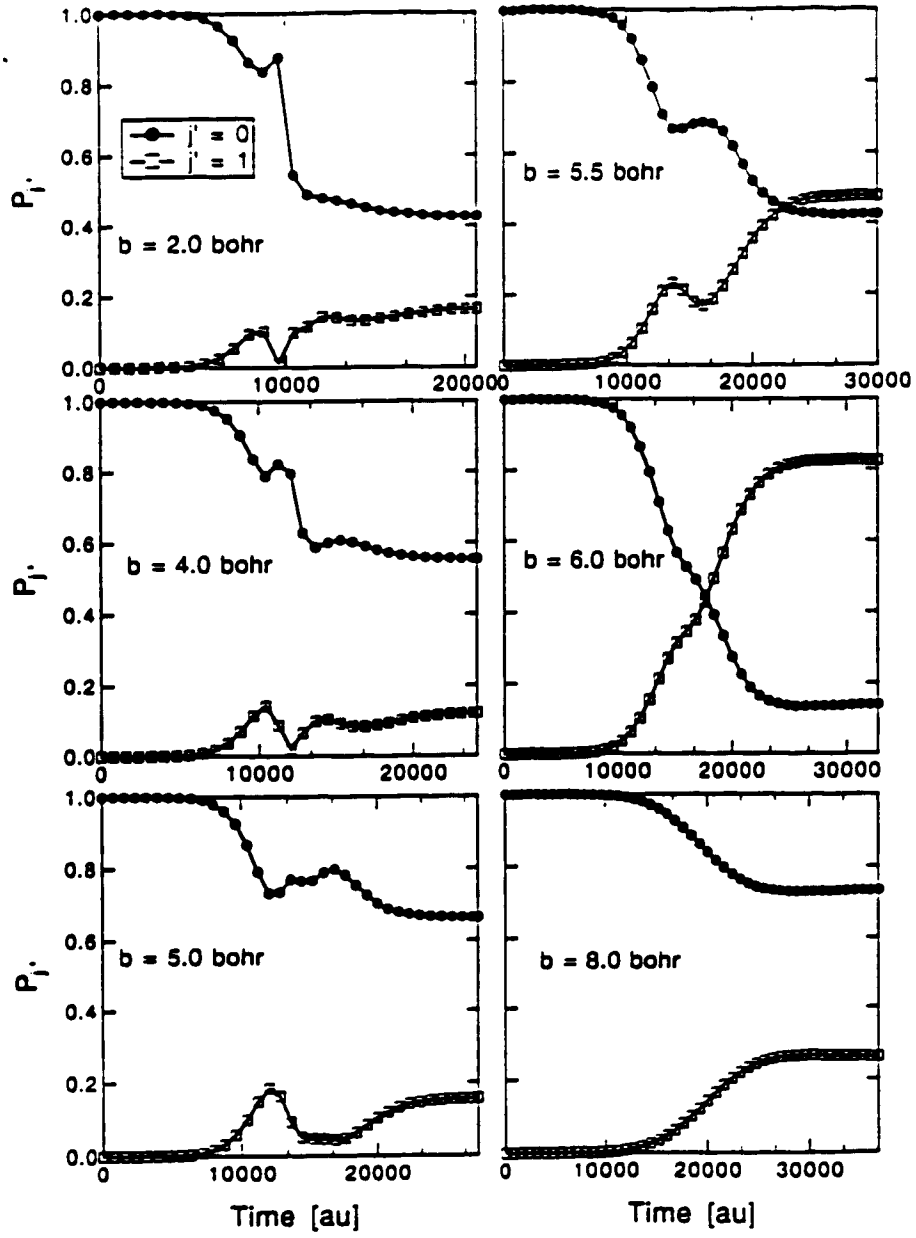

Figure 5. Time-dependent rotational state probabilities from semiclassical calculation at several impact parameters, b. Initial rotational state is j=0; relative collision energy is 135 meV. Note that the time scales in figures 5 and 6 vary with b. This is done to locate the turning point in the translational motion, near the mid-point of the time axis (figure 5) and to emphasize the symmetry of the time-dependent potential (figure 6).

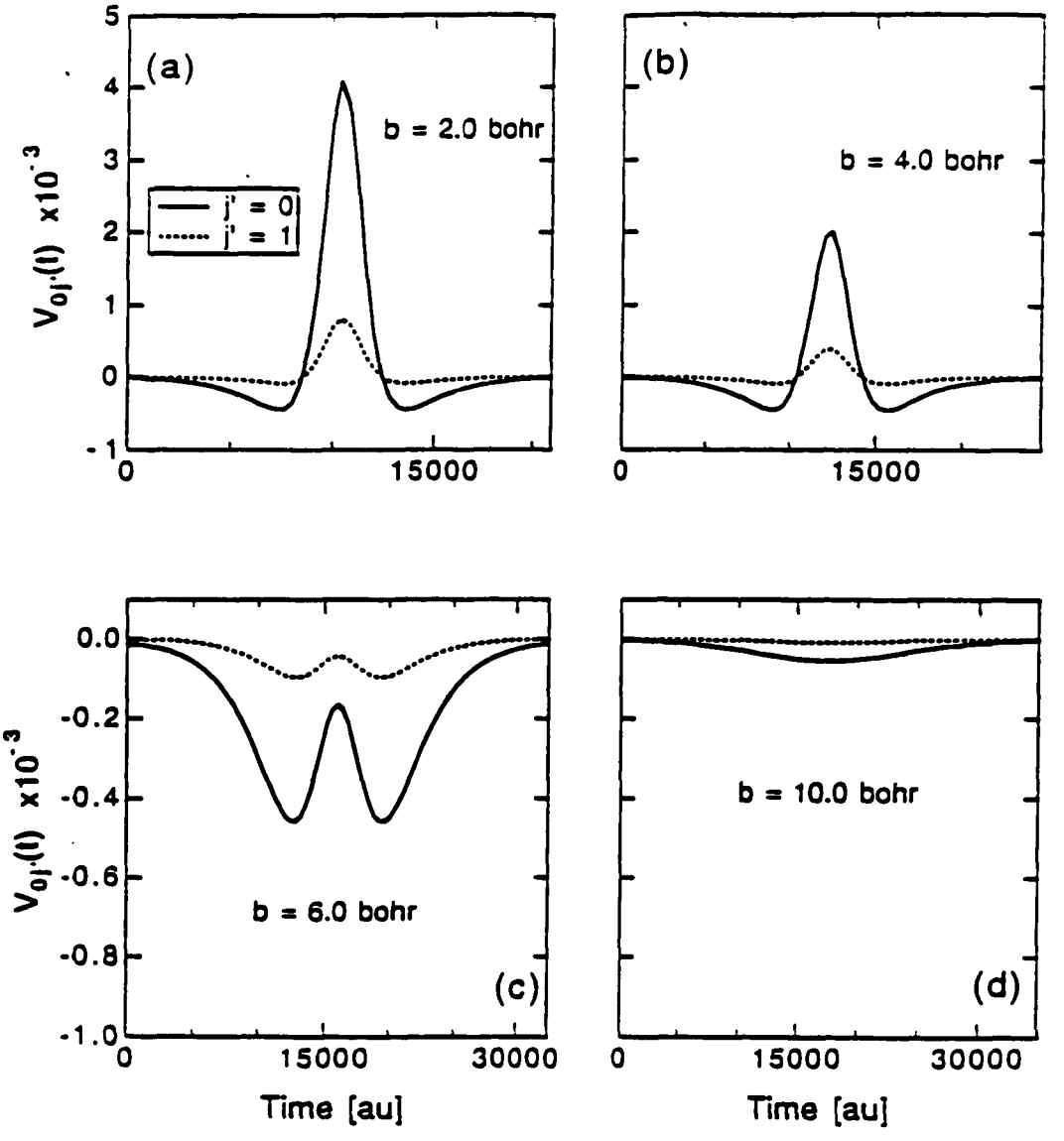

Figure 6. Time-dependent coupling elements $V_{00}(t)$ and $V_{01}(t)$ at several impact parameters, b.

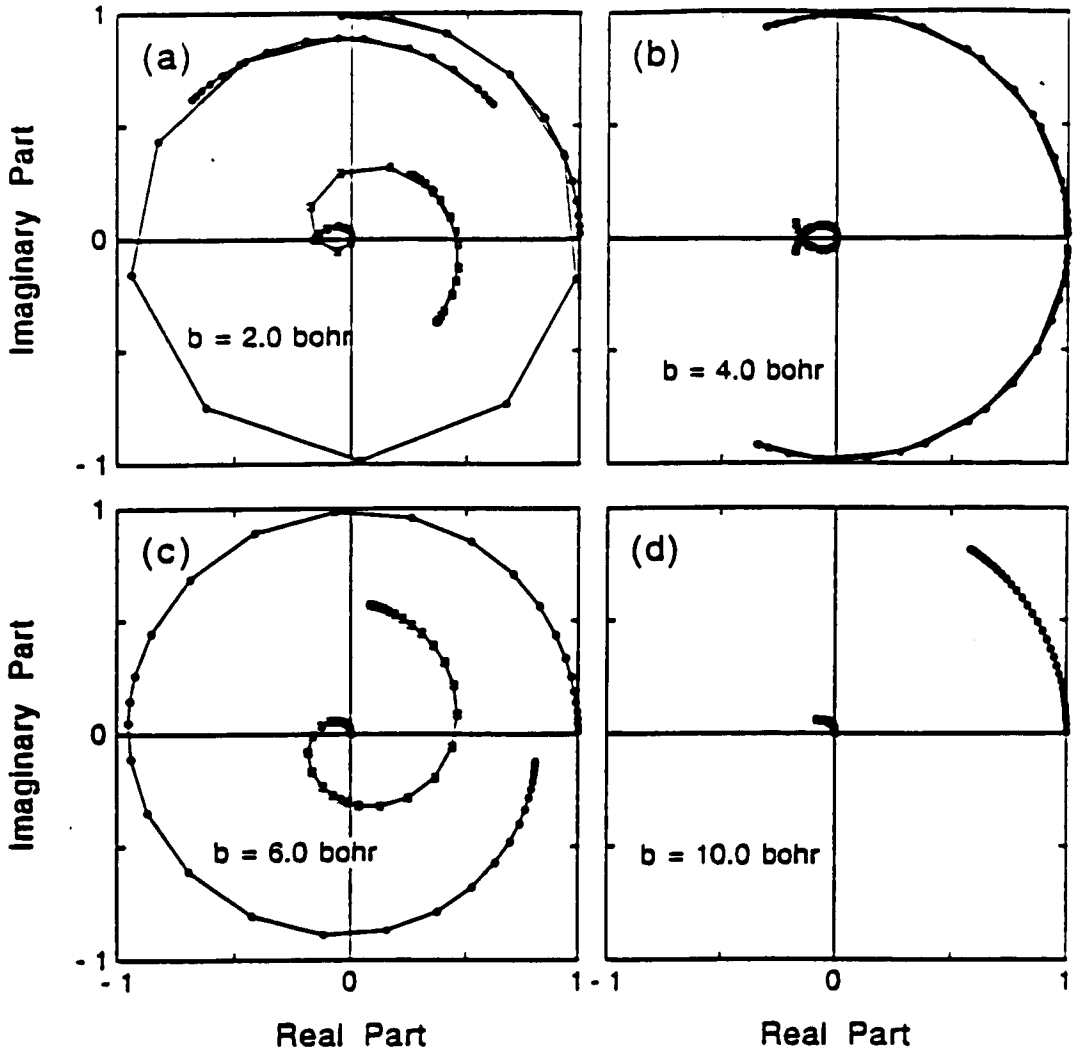

Figure 7. Plot of time-dependent expansion coefficients c_0 (filled circles) and c_1 (open squares) in the complex plane for two-state model calculation, ε=0.1. At time t=0, c_0=(1,0) and c_1=(0,0). The initial sense of motion is a spiral in the counterclockwise direction. Sampling rate for positive potential elements (that is, for clockwise rotation -- see text) is four times that for negative coupling elements.

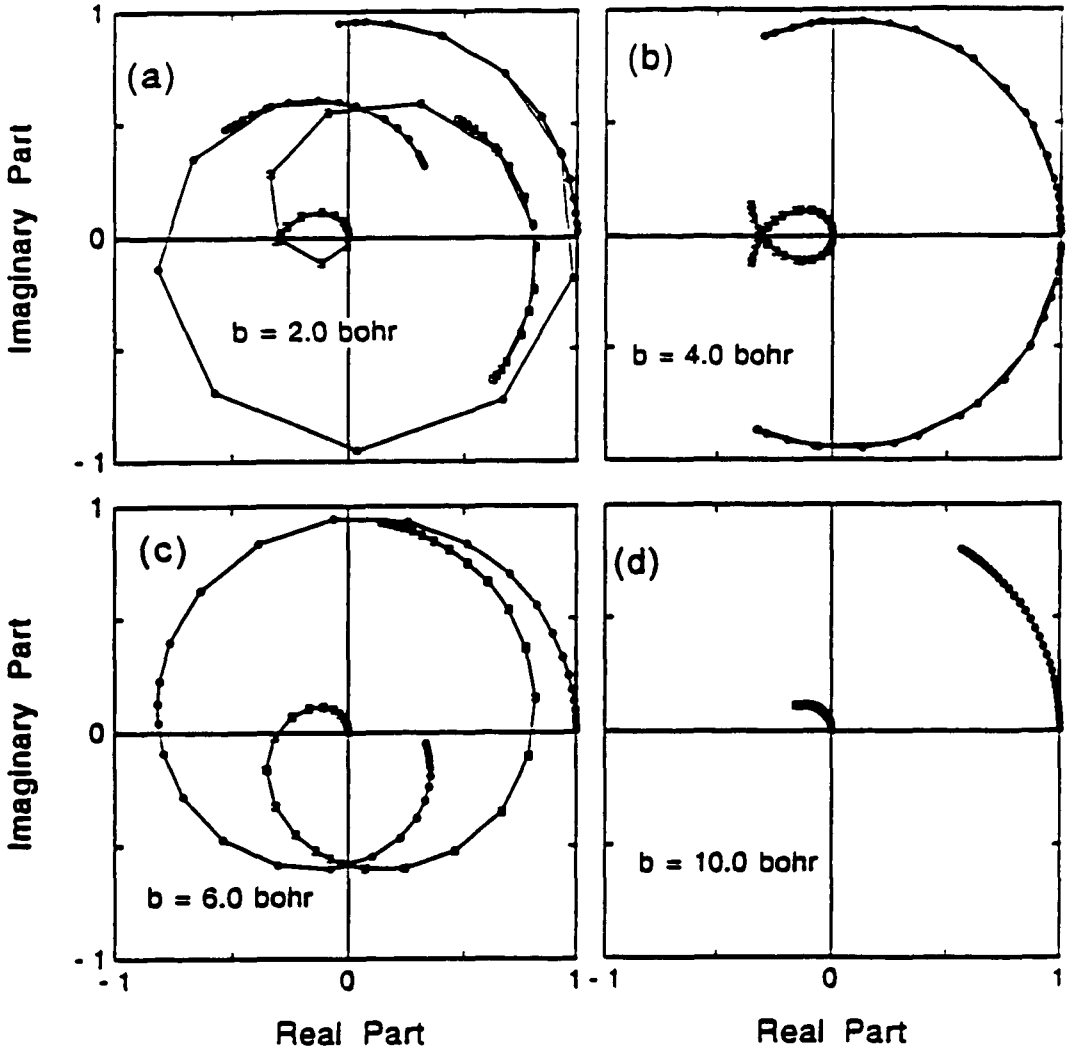

Figure 8 Same as figure 7 except ε=0.2.

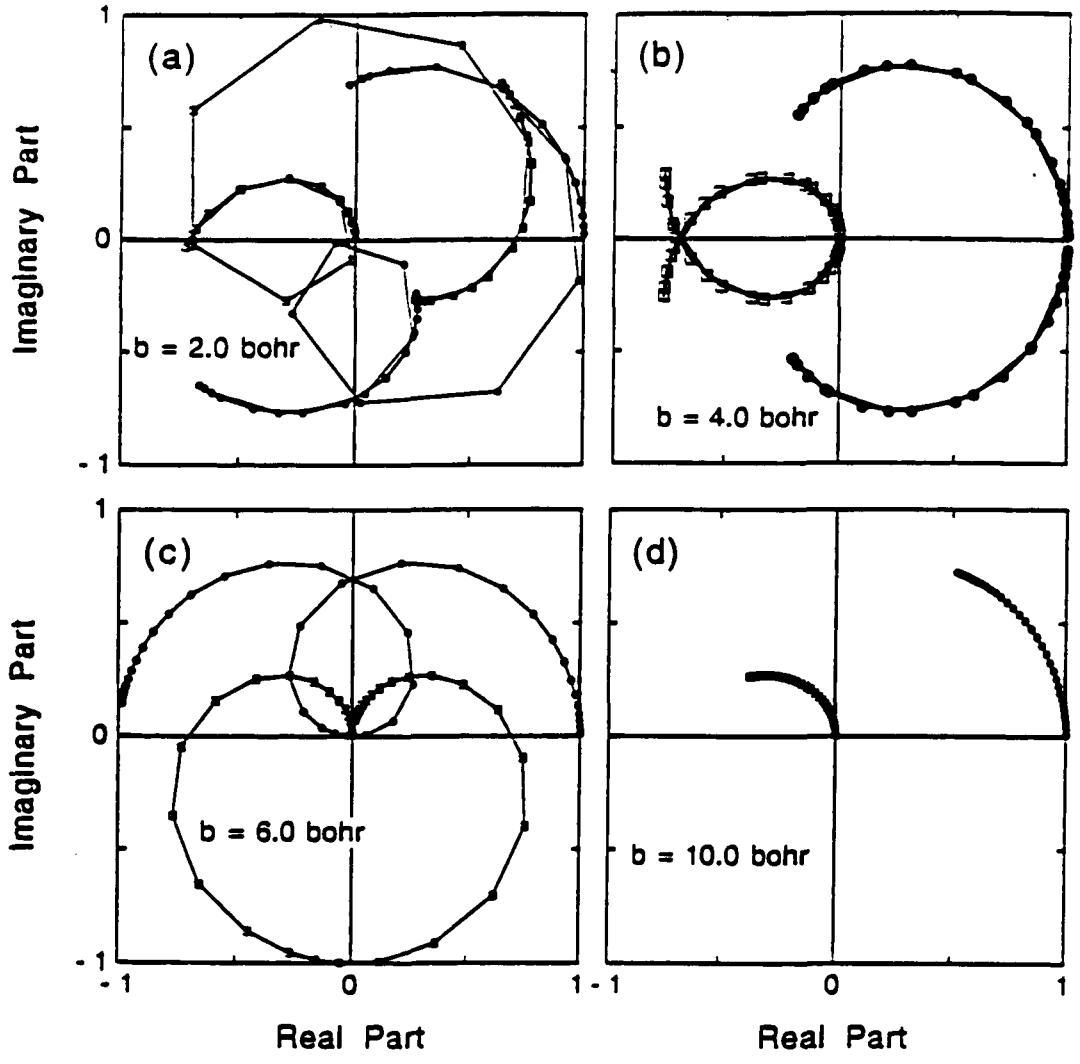

Figure 9 Same as figure 7 except ε=0.5.

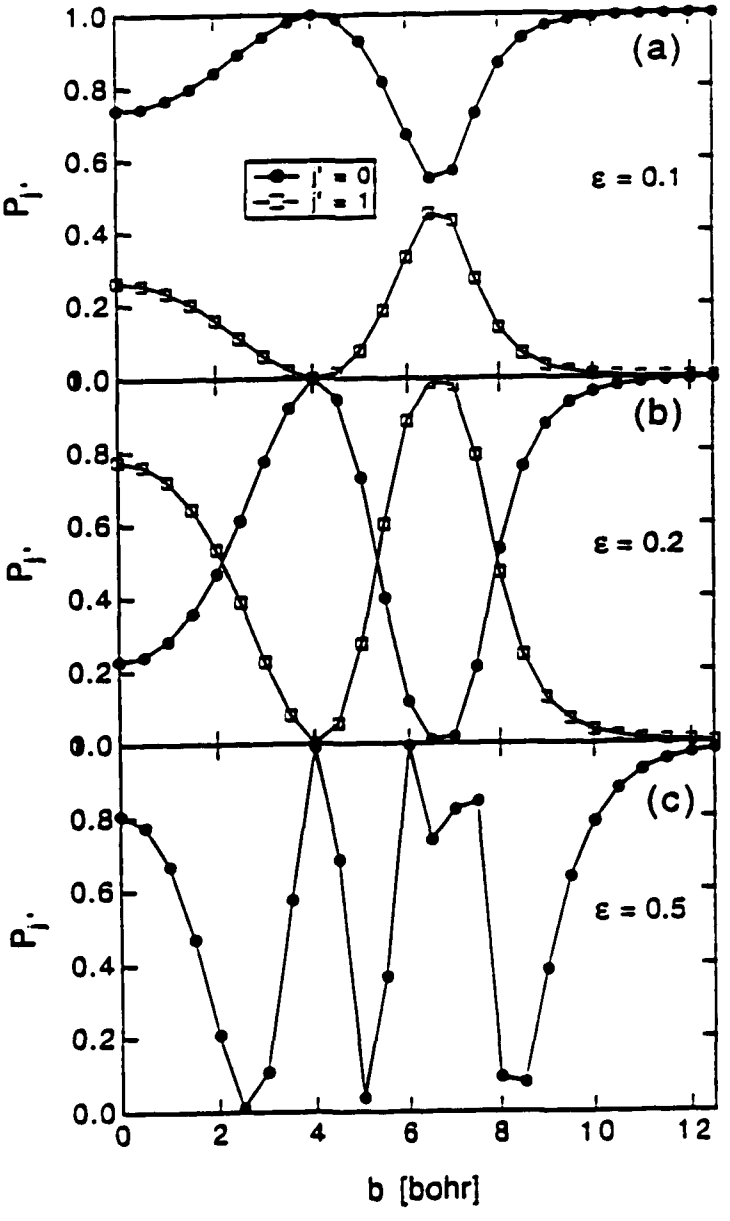

Figure 10. Opacity functions from two-state model calculation for ε=0.1, 0.2 and 0.5. In figure 10(c) only the opacity function for j'=0 is shown for clarity, the opacity function for j'=1 is the complement of that shown.

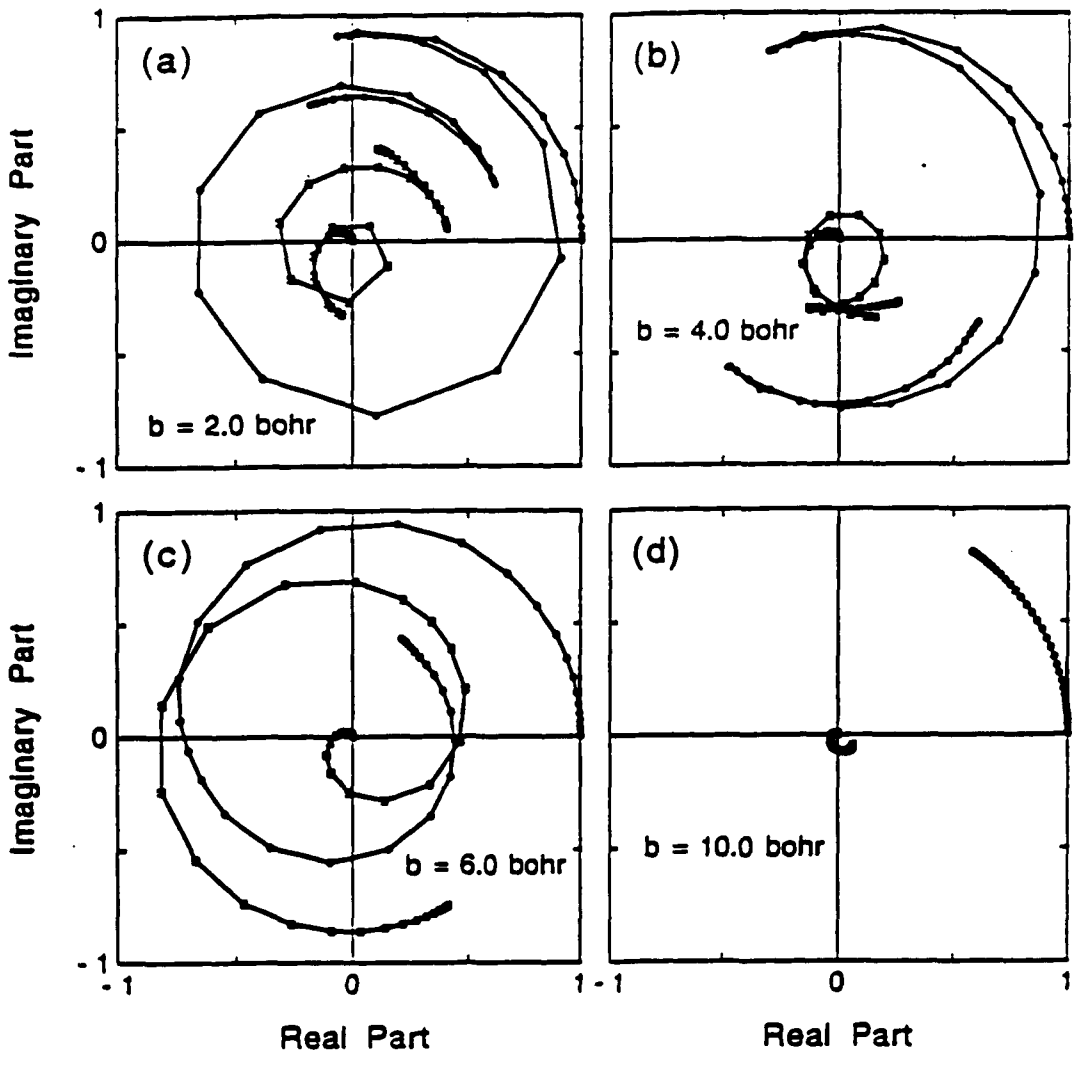

Figure 11. Plot of expansion coefficients in the complex plane from full semiclassical model for states $|j'=0,m'=0\rangle$ and $|j'=1, m'=0\rangle$ at same impact parameters as those in figures 7-9. Initial state is $|j=0, m=0\rangle$; relative collision is 135 meV.

Chapter 6

Semiclassical Study of the Sudden Approximations in Rotationally Inelastic Scattering of Ar+HF

I. Introduction

One of the first attempts to systematize rate constants for state-to-state rotational relaxation was made by Polanyi and Woodall over two decades ago,[1] as a by-product of measuring state-resolved populations in chemiluminescent reactions producing hydrogen halide products. The early success of their "exponential gap" scaling rule lay in its ability to correlate rate constants for a wide variety of systems. More detailed measurements however, especially differential cross sections, could not be explained by a two-parameter empirical model. Instead, these more detailed studies began to reveal the dynamical role of the potential energy surface for rotational energy transfer.

In the last decade, scattering studies have been joined by high-resolution spectroscopic studies on weakly-

bound van der Waals molecules. Whenever it has been accessible, experimental high resolution spectroscopy has always provided the most accurate source of information on intermolecular forces, including those for van der Waals molecules.[2] In particular, accurate potential energy surfaces have been obtained using these techniques for weakly-bound rare gas+hydrogen halide systems.[3,4] However, such measurements are sensitive primarily to those parts of the potential capable of supporting bound states. Repulsive regions of the potential surface can only be obtained by rather extensive extrapolations of the spectroscopic information. In contrast, state-to-state scattering experiments, especially differential cross sections (DCS), probe the repulsive wall of the potential directly.[5,6] Such experiments can help characterize the potential for purely repulsive or very weakly attractive systems.[6]

It is clear from the above that scattering measurements and spectroscopy tend to provide complementary information on the potential. Spectroscopic data[7] for the Ar+HF system have been used by Hutson[3] to obtain a potential of excellent quality in the attractive region, hereafter referred to as the "Hutson H6" potential. Scattering data, in the form of final state selected DCS from crossed molecular beam experiments on Ar+HF, have also recently been obtained.[8] In order to analyze these experiments, "Exact" quantum mechanical close-coupled (CC) inelastic scattering calculations have been carried out[9] using the Hutson H6 potential energy surface.[3] When the results were transformed to the laboratory scattering frame, and averaged over the experimental conditions, the agreement was found to be quite good for the low final rotational states, $j' \leq 2$. The comparison of the CC results with the experimental DCS for the higher rotational states was poor.[9] This is not surprising, since large Δj transitions are due primarily to collisions which sample the repulsive wall of the

potential,[10,11] and this is the portion of the potential not directly probed by the spectroscopic studies. Again it is clear that spectroscopic and scattering results are best combined to determine attractive and repulsive regions of the potential surface.

Nevertheless, scattering results are not necessarily insensitive to the attractive portions of the potential. In the earlier study,[9] we conducted calculations to determine the sensitivity of the scattering to various features of the potential. It was found that the state-to-state DCS, particularly for the $j=0\rightarrow j'=0$ and $j=0\rightarrow j'=1$ transitions, displayed novel features with interference characteristics of quantum mechanical origin.[9] Using the CC method, it was shown that these DCS were very sensitive to changes in the repulsive wall. Further work on this system using a semiclassical approach[12] showed that the features were due to the combined influence of both the attractive and repulsive regions of the potential.

For predominantly repulsive systems, the theoretical technique most successful in extracting information on the potential energy surface has been the infinite order sudden approximation (IOSA).[13,14] This approximation has also been invaluable in obtaining a physical understanding of rotational excitation due to scattering from a hard anisotropic core.[11,15] The success of the IOSA in fitting repulsive potentials is due to the following: the method is computationally fast; and, in conjunction with an additional semiclassical approximation,[11,16] it links the local surface topography with the dynamics. Unfortunately, it is likely that the IOSA performance is poorest for precisely those rare gas+hydrogen halide (HX) van der Waals systems best characterized spectroscopically. Not only is the energy sudden criterion violated by the large HX rotational spacings, but the centrifugal sudden criterion must also be

regarded as suspect because of the attractiveness of the potential energy surface.

Accordingly, calculations on the Hutson H6 Ar+HF potential were carried out using the IOSA and compared with CC data.[9] The results were disappointing poor, at least quantitatively, in the sense that they failed to reproduce the "exact" CC results at the state resolved level, thus prohibiting the use of the IOSA in systematically improving the repulsive region of the potential. Since the IOSA is such a frequently used tool in the analysis of rotationally inelastic scattering[11] it would be beneficial to better understand these discrepancies between the IOSA and CC results. In particular, we use here previously developed semiclassical methods[12,17] to understand the origins of these deviations. There have previously been a few systematic studies of decoupling approximations within a time-dependent framework.[17,18,19] Perhaps the most comprehensive such work was that on the classical limit of decoupling.[20]

In section II, we present the computational methods employed in this study. In particular, we detail the semiclassical method together with the decoupling and sudden approximations used. In section III, we compare the semiclassical CC and IOSA results. We further relate features in the CC and IOSA DCS to oscillations in the semiclassical opacity functions. This leads us to introduce a two-state model of the semiclassical method. This simplification elucidates shortcomings of the IOSA occurring even for low impact parameters (i.e. repulsive collisions). Finally, we examine the time-dependent evolution of the system to explain the failure of the IOSA for high impact parameters. Concluding remarks are made in section IV.

II. Calculations

A. Time-Independent Methods

The time-independent close-coupled (CC) calculations using the HIBRIDON package of molecular scattering programs have been described elsewhere in detail.[9,21] The infinite order sudden approximation (IOSA) calculations are carried out using the standard ℓ-initial convention.[13,14]

B. Time-Dependent Methods

The time-dependent methods employed here are less standard than the time-independent methods. We therefore describe the time-dependent semiclassical (or classical path) method in some detail. In addition, we give explicit formulations for a hierarchy of approximations leading ultimately to the semiclassical version of the IOSA. The methods have been reviewed previously.[17,19,22]

In the semiclassical approximation for rotationally inelastic collisions[23] we take advantage of the mass discrepancy between the translational and internal coordinates of the collision system. In this case we are scattering a hydrogenic diatom (HF) from a heavy rare gas atom (Ar). In this problem the translational reduced mass, given by

$$M = \frac{m_{Ar}(m_F + m_H)}{m_{Ar} + m_F + m_H} \quad , \tag{1}$$

is large. Therefore, the relative motion can reasonably be treated classically. Conversely the rotational degrees of freedom of the hydrogenic HF must be treated quantum mechanically to give accurate dynamics.[9]

The motion for the translational coordinate is governed by Hamilton's equations of motion. In Cartesian coordinates these are given by

$$\dot{\mathbf{R}} = \frac{\partial H_{cl}}{\partial \mathbf{P}} \quad ; \quad \dot{\mathbf{P}} = -\frac{\partial H_{cl}}{\partial \mathbf{R}} \tag{2}$$

where $\mathbf{R}$ is the displacement of the atom from the diatom center of mass, and $\mathbf{P}$ is its conjugate momentum. The classical Hamiltonian for the translational motion is given by

$$H_{cl} = \frac{P^2}{2M} + \langle V(\mathbf{R}) \rangle \tag{3}$$

where $\langle V(\mathbf{R}) \rangle$ is an appropriate average of the potential energy over the internal coordinates.[24]

Propagation of the rotational degrees of freedom is achieved by solving the time-dependent Schrödinger equation for the internal state wave function[25]

$$i\hbar \frac{d|\Psi(t)\rangle}{dt} = \hat{H}_q |\Psi(t)\rangle \tag{4}$$

where $\hat{H}_q$ is the quantum Hamiltonian for a rigid rotor in a time-dependent external field, $\hat{V}(t)$. The time dependence of $\hat{H}_q$ arises from the external field as

$$\hat{H}_q = \hat{H}_0 + \hat{V}(t) \quad , \tag{5}$$

where $\hat{H}_0$ is the zeroth order Hamiltonian for an unperturbed rigid rotor. We expand the wave function for the system in an appropriate basis set (i.e. the eigenstates of $\hat{H}_0$, the spherical harmonics) so that

$$\left|\Psi(t)\right\rangle = \sum_l c_l(t)\left|l\right\rangle \exp\left(-{}^{iE_l t}/_{\hbar}\right) \tag{6}$$

with $c_l(t)$ being the time-dependent expansion coefficient for the l^{th} rotational state, $|jm\rangle$, and E_l is the energy associated with the j rotational level of the l^{th} state. The time-dependent quantum equations of motion are then given by

$$i\hbar\dot{c}_k = \sum_l c_l V_{kl}(t)\, \exp\left(i\omega_{kl}t\right) \tag{7}$$

where

$$V_{kl}(t) = \left\langle k\left|\hat{V}(t)\right|l\right\rangle \tag{8}$$

and

$$\omega_{kl} = \frac{E_k - E_l}{\hbar} \tag{9}$$

We shall refer to eq.7 as being the "full" semiclassical treatment, or simply "SC". The integral in eq.8 is given by

$$V_{kl}(t) = \int d\hat{\mathbf{r}}\, Y^*_{j'm'}(\hat{\mathbf{r}})\, \hat{V}(\mathbf{R}(t),\hat{\mathbf{r}})\, Y_{jm}(\hat{\mathbf{r}}) \tag{10}$$

where $\mathbf{R}(t)$ is the atom-diatom displacement vector as a function of time from the classical part of the calculation and $\hat{\mathbf{r}}$ is the diatom bond unit vector. The classical and quantum degrees of freedom are propagated simultaneously.

The potential energy operator, $\hat{V}$, taken as the interaction potential, $V(R,\gamma)$, is a function of R and γ only. R is the length of the vector $\mathbf{R}(t)$ and γ is the angle between $\hat{\mathbf{r}}$ and $\mathbf{R}(t)$. In the classical trajectory, $\mathbf{R}$ is described in

space-fixed coordinates.[26] In this study $V(R,\gamma)$ is taken as the Hutson H6 potential for Ar+HF(v=0).[3] This potential is selected over several other surfaces[27] because it has been shown in previous work[9] to best reproduce scattering features experimentally observed in rotationally resolved differential cross sections.[8] It has also been very useful in extending further spectroscopic studies.[28]

The time-dependent probability of finding the system in some rotational state, k, is given by

$$P_k(t) = |c_k(t)|^2 \tag{11}$$

The final probability is taken as $t \rightarrow \infty$. In our semiclassical treatment a trajectory is started at some impact parameter, b, and run until the final rotational state probability is constant to three decimal places. Since we are not concerned with resolving the m-sublevels, the quantum opacity function for a given final rotational level, $P_{j'}(b)$, is given as the sum

$$P_{j'}(b) = \sum_{m'=-j'}^{j'} |c_{j'm'}|^2 \tag{12}$$

The scattering angle, θ, for a trajectory is given as the angle between the initial and final classical relative momentum vectors, $\mathbf{P}$ and $\mathbf{P}'$, respectively. The classical deflection function, $\theta(b)$, is obtained from a set of trajectories calculated for an elastic collision between the Ar and HF. The $\langle V(R) \rangle$ used in the classical trajectory calculation is taken as the spherical average of the H6 potential. It has been suggested that an "Ehrenfest" average of the potential,[22,23] given by

$$\langle V(R(t)) \rangle = \langle \Psi(t) | V(\mathbf{R}(t), \hat{\mathbf{r}}) | \Psi(t) \rangle \tag{13}$$

be used in the classical trajectory. We have employed this method in our calculations and find that using the spherical average of the potential shows no significant difference between the deflection or opacity functions from an Ehrenfest average calculation, but with a substantial savings in computational time.

From the quantum opacity function and the classical deflection function we calculate the DCS using

$$\frac{d\sigma_{j'}(\theta)}{d\varpi} = \frac{1}{\sin\theta}\sum_i b_i P_{j'}(b_i)\left|d\theta/db\right|_i^{-1} \qquad (14)$$

where b_i is the impact parameter leading to the particular scattering angle, θ. In the sum over i, there is one trajectory for $\theta > |\theta_r|$, whereas three trajectories contribute for $\theta \leq |\theta_r|$, where θ_r is the classical rainbow angle.[29] The problems associated with using this classical definition of the DCS are well known;[30] however we find this method to be sufficient in our application.

The first of the approximations to the full SC dynamics that we introduce is the "energy sudden" approximation.[31,32] This approximation is based on the assumption that all rotational energy levels are degenerate, i.e. $E_k = E_l$. In this case, $\omega_{kl} = 0$ and eq.7 reduces to

$$i\hbar\dot{c}_k = \sum_l c_l V_{kl}(t) \quad . \qquad (15)$$

We will refer to this as the semiclassical energy-sudden approximation (SC-ES). While this approximation does not lead to a significant savings in computational time, we will see in the following section that the SC-ES does allow for the investigation of the exact nature of any differences between the IOSA and a fully coupled calculation of the scattering

dynamics.

In order to implement the decoupling approximations, we introduce body-fixed (BF) coordinates,[33] in which the BF vector, $\hat{\mathbf{z}}$, is chosen to lie along the internuclear separation vector, $\mathbf{R}$. In this case, the time-dependent equations of motion are given by

$$i\hbar\,\dot{c}_{j'm}(t) = \sum_{j} c_{jm}(t)\left\langle j'\,m\middle|V(t)\middle|jm\right\rangle \exp(i\omega_{j'j}t) \quad . \qquad (16)$$

(Note that due to the axial symmetry of the potential, only $\Delta m=0$ transitions are allowed.) Because of the similarity of this method to the time-independent coupled-states approximation,[34] we shall denote the results from eq.16 as the semiclassical coupled-states (SC-CS) approximation. Essentially, the approximation involved in going from the full semiclassical theory to the SC-CS approximation, in which the m-sublevels are decoupled, is equivalent to the "centrifugal sudden" approximation.[13,35]

The final approximation required to produce a coupling scheme in the time-dependent, semiclassical regime equivalent to the IOSA is to incorporate the energy sudden approximation into eq.16. Thus, the time-dependent equivalent of the IOSA is given by

$$i\hbar\,\dot{c}_{j'm}(t) = \sum_{j} c_{jm}(t)\left\langle j'\,m\middle|V(t)\middle|jm\right\rangle \quad . \qquad (17)$$

We shall refer to this result as the SC-IOS approximation. In all of the semiclassical methods the time-dependent equations are solved using a standard fourth-order Runge-Kutta integrator. We concentrate our efforts in this paper on the

transitions out of an initial state |j=0,m=0> at a single collision energy of 135 meV, the nominal collision energy of the scattering experiment.[8,9]

III. Results and Discussion

The DCS calculated using the "exact" CC, IOSA and full semiclassical methods at a collision energy of 135meV are shown in figure 1. The most notable features of the CC DCS have been discussed elsewhere.[9,12] To summarize: (1) the rainbow, expected at 7°, in the elastic 0→0 DCS is suppressed whereas this feature is present in the 0→1 DCS; (2) there is a broad shoulder in the 0→0 DCS at θ~40-70° with a concomitant dip in the 0→1 DCS centered near θ~60°. It has been shown[9] that these features have a quantum mechanical origin. Away from the rainbow angle, there is good agreement between the semiclassical DCS and the CC results indicating that the full semiclassical model provides an reasonable description of the collision dynamics.[12]

The IOSA DCS shows features qualitatively similar to those in the CC DCS. For instance, the rainbow in the 0→0 DCS is suppressed in this approximation, whereas the 0→1 DCS does show a rainbow. In addition, there is a shoulder in the 0→0 DCS, but in the IOSA the feature has shifted out to scattering angles near θ~90°. The accompanying dip in the 0→1 DCS is also shifted to the same region.

In figure 2 we compare the full semiclassical calculations of the DCS with those using the SC-CS and the SC-IOS approximations. It is seen that the full and CS semiclassical results are in very good agreement, so that the SC-CS approximation reproduces the CC DCS rather well for this case. In contrast, the SC-IOS differs markedly from the SC results. The shoulder/dip features in the SC-IOS DCS are shifted to higher scattering angles. In fact, the SC-IOS

greatly resembles the results from the time-independent IOSA calculation. To emphasize the similarity, we compare the DCS from the IOSA with those from the SC-IOS treatment in figure 3. The agreement is very good, with the exception of an indication of the rainbow in the SC-IOS elastic DCS. (In the rainbow region, a "primitive" semiclassical approximation like eq.14 is expected to fail catastrophically.[36])

We now examine the collision dynamics within each of the approximations more closely. We take advantage of the time-dependent semiclassical framework, in which we can examine the contributions from individual impact parameters and the role of the potential as the trajectory evolves in time. We use these attributes to analyze the discrepancies between the fully-coupled SC and the SC-IOS calculations and relate these back to the differences between the quantum CC and IOSA results.

We first examine opacity functions from the full SC calculation and from each of the more approximate methods, shown in figures 4a-d. The opacity functions for the full SC (figure 4a) and the SC-CS (figure 4b) are almost identical, with the most marked difference being a somewhat smaller $P_1(b)$ near the maximum at b=7 bohr in the SC-CS. This translates into the excellent agreement between the full SC and SC-CS DCS of figure 2. Comparing the opacity functions from the SC-ES (figure 4c) and SC-IOS (figure 4d) with figure 4a, we immediately see a dramatic difference attributable to the ES approximation.

The most obvious difference between the SC-ES and the full SC opacity functions is in the impact parameter region, 5.5<b<8.0 bohr. However, the far more noticeable effect on the observed DCS comes from the more subtle difference in the range, 3.5<b<5.5 bohr, as we shall explain below. In this region, the peak and dip seen, respectively, in the $P_0(b)$ and

$P_1(b)$ functions are shifted to a slightly lower b in the SC-ES (and SC-IOS) opacity functions. To highlight this shift we plot, in figure 5, the opacity functions for $j'=0$ only. We also show the deflection function in this plot to indicate the scattering angles at which the features in the opacity functions manifest themselves in the DCS. The DCS is obtained from the opacity and deflection functions using eq.14. It is clear that a maximum in the opacity function, in the region where $\theta(b)$ is single valued, will account for a peak or "shoulder" in the DCS. (Scattering angles less than the rainbow angle, θ_r, result from impact parameters b>6 bohr. In this region the effect of changes in the $P_{j'}(b)$ on the DCS is less obvious since three impact parameters contribute to the DCS.) From figure 5 we recognize that the shift of the $P_0(b)$ peak to lower impact parameter will cause the "shoulder" feature in the $j'=0$ DCS to shift out to higher scattering angles. The shift in the $P_0(b)$ peak from b=4.5 bohr to b=4.0 bohr is responsible for the shift of the shoulder in the $0\rightarrow0$ DCS in the IOSA of figure 1. Note that, although the $P_0(b)$ has a larger value in the SC-IOS, it occurs at a lower b value. This reduced b-weighting (see eq.14) compensates for the increased peak height and the shoulders are seen to have comparable intensities.

Complementary arguments are used to explain the more dramatic dip in the $0\rightarrow1$ DCS observed between the CC and the IOSA. In figure 6 we plot the opacity functions for $j'=1$ from each of the SC approximations. As with the peak in $P_0(b)$, the dip in $P_1(b)$ is shifted to lower impact parameters in the SC-IOS as compared to the dip in the full SC opacity function. We can also see in figure 6 that the dip in the SC-IOS $P_1(b)$ is deeper than in the SC model. The combination of these two features – the shift to lower impact parameter and the smaller $P_1(b)$ – result in the deep hole observed for the $0\rightarrow1$ IOSA DCS in figure 1.

We have now established a connection between the opacity functions calculated from the various SC approximations and the features observed in the CC and IOSA DCS. We now go on to discuss the origins of the differences observed in the opacity functions calculated using the SC and SC-ES methods. Looking at figures 5 and 6 we see that there are two distinct regions in the opacity functions. In the low impact parameter region, b<5.5 bohr, the SC and SC-ES results are qualitatively similar. However, in the high impact parameter region, b>5.5 bohr, the opacity functions differ quite dramatically. We take this impact parameter, b=5.5 bohr, as the division point for our discussion because of the qualitative difference between the opacity functions in these regions.

Further investigation of the dynamics reveals that a qualitative change in the coupling potential, $V_{kl}(t)$, occurs in the region of the dividing point, b=5.5 bohr. This is illustrated for $V_{00}(t)$ and $V_{01}(t)$ in figure 7. The $V_{kl}(t)$ changes from a function which has attractive and repulsive portions to one which is solely attractive. We discuss the scattering dynamics in these two impact parameter regions in the sections below.

A. Low Impact Parameter Region

As stated above, the shift in the shoulder/hole feature to higher scattering angles in the IOSA is caused by a related shift of the peak in the $P_0(b)$ to lower impact parameters in the SC-IOS calculations. In a previous publication Barrett, et al.[12] employed a "two-state model" to suggest that the shoulder/hole feature in the j'=0 and 1 DCS was due to a balance between the repulsive and attractive parts of the potential energy surface. A two-state model was justified in the previous study by noting that: (1) There is a strong coupling between the j=0 and j=1 states, denoted by

the near mirror imaging of the $P_0(b)$ in the $P_1(b)$; that is, as the $P_0(b)$ increases or decreases, the $P_1(b)$ displays a complementary decrease or increase; (2) The transition probabilities for the system are dominated by the transitions $0\rightarrow0$ and $0\rightarrow1$; these two final states comprise 70% or more of the total transition probability at all impact parameters.

The equations of motion for the two-state model, within the SC-CS approximation, are given by

$$i\hbar\,\dot{c}_0(t) = c_0(t)V_{00}(t) + c_1(t)V_{01}(t)\exp(i\omega_{01}t) \qquad (18a)$$

$$i\hbar\,\dot{c}_1(t) = c_0(t)V_{01}(t)\exp(i\omega_{10}t) + c_1(t)V_{11}(t) \quad . \qquad (18b)$$

Note that $V_{10}(t)=V_{01}(t)$. By recognizing[12] that the $V_{00}(t)$ and $V_{11}(t)$ are very similar during the course of the time evolution and by further recognizing[12] that the $V_{01}(t)$ has roughly the same functional form as $V_{00}(t)$, but with a smaller magnitude, we make the following simplifications to eqs.18: (1) We substitute $V_{00}(t)$ for $V_{11}(t)$; (2) We employ a parameter to determine the coupling between the 0 and 1 states. In doing this we replace $V_{01}(t)$ with $\varepsilon V_{00}(t)$, where ε is the coupling parameter less than 1. Using these simplifications in eqs.18 we obtain

$$i\hbar\,\dot{c}_0(t) = V_{00}(t)\left(c_0(t) + \varepsilon c_1(t)\exp(i\omega_{01}t)\right) \qquad (19a)$$

$$i\hbar\,\dot{c}_1(t) = V_{00}(t)\left(\varepsilon c_0(t)\exp(i\omega_{10}t) + c_1(t)\right) \qquad (19b)$$

as the basic equations for the fully coupled two-state model. As in a previous work[12] we use, as a reasonable estimate to the true coupling potential, an ε value of 0.2 to analyze the scattering dynamics of the fully coupled system.

We may further simplify the two-state model by incorporating the ES approximation into eqs.19 to obtain

$$i\hbar\dot{c}_0(t) = V_{00}(t)\left(c_0(t) + \varepsilon c_1(t)\right) \qquad (20a)$$

$$i\hbar\dot{c}_1(t) = V_{00}(t)\left(\varepsilon c_0(t) + c_1(t)\right) \qquad (20b)$$

as the "energy sudden" two-state model. We now use the simplified two-state models of eqs.19 and 20 to explore the effects of the ES approximation on the scattering dynamics. In figure 8 we plot the opacity function for j'=0 from the two-state model with and without the ES approximation. It is evident that the $P_0(b)$ are similar up to b~5.0 bohr. The only significant difference is a slight shift of the energy sudden curve to lower impact parameters. Qualitatively, this is just what is observed in figure 5: both methods which employ the energy sudden approximation have their first maximum in $P_0(b)$ at lower b values than those calculations which have non-zero energy spacings. This shift to lower b in that impact parameter region where the scattering is sideways is just what is required to shift the shoulder in the $0\rightarrow0$ DCS to higher scattering angles, as was observed in the IOSA of figure 1. Thus the two-state model reproduces this trend very well. We analyze this shift further below.

One advantage of the two-state model is that it is simple to analyze. In particular, there are only two state coefficients to consider, $c_0(t)$ and $c_1(t)$, and the scattering dynamics reduce to the time-evolution of these two states. We plot trajectories of these coefficients in figure 9. The upper panel shows the time-evolution of the system using the energy sudden formulation (eqs.20); the lower panel shows the evolution of the full two-state model (eqs.19). In order to explain the motion in these plots we note that for $\varepsilon=0$ (i.e. no coupling between the states) the equations of motion are

$$\dot{c}_i = \frac{-ic_i V_{00}}{\hbar} \qquad (i = 0,1) \quad . \qquad (21)$$

By writing $c_i=|c_i|\exp(i\phi_i)$, where $\phi_i=\arg(c_i)$, substituting into eq.21, and equating the real and imaginary parts we obtain:

$$\frac{d}{dt}|c_i| = 0 \qquad ; \qquad \frac{d}{dt}\phi_i = \frac{-V_{00}}{\hbar} \quad . \tag{22}$$

Thus motion in this case is pure rotation in the complex plane. A negative coupling potential leads to counter-clockwise rotation in the complex plane; a positive V_{00} gives clockwise rotation. Furthermore, for the $\varepsilon=0$ case, the equations may be solved explicitly to give

$$c_i(t) = c_i(-\infty)\exp\left(-i\int_{-\infty}^{t} dt' V_{00}(t')/\hbar\right) \tag{23}$$

as the time-evolution for the states. The integral in eq.23 is known as the action integral.[17,22]

We consider next the effect of c_j ($j\neq i$) on c_i when c_i is negligible. In this case we have

$$i\hbar\,\dot{c}_i(t) = c_j(t)\varepsilon V_{00}(t)\exp(\pm i\omega_{01}t) \tag{24}$$

where the +(-) applies to i=0(1). An alternative expression for eq.24 gives the change in c_i, δc_i, as

$$\begin{aligned}\delta c_i(t) = \dot{c}_i(t)\delta t &= \left(\delta t\hbar^{-1}\varepsilon V_{00}(t)\left|c_j(t)\right|\right)\exp\left[i\left(\phi_j - \pi/2 \pm \omega_{01}t\right)\right] \\ &= \left\{\delta t\hbar^{-1}\varepsilon\left|V_{00}(t)\right\|c_j(t)\right|\right\}\exp\left[i\left(\phi_j - \mathrm{sign}(V_{00}(t))\pi/2 \pm \omega_{01}t\right)\right].\end{aligned} \tag{25}$$

The term within the braces{} is always positive. Thus, when ω_{01} is zero (i.e. in the ES approximation), the change in c_i due to a nonzero c_j is a complex number rotated $\pi/2$ from c_j on the clockwise or counter-clockwise side depending on the sign of V_{00}.

The two-state model was utilized in an earlier study[12] to explain the presence of the shoulder in the 0→0 DCS. We briefly reiterate some of our earlier findings to explain the difference between the two-state model with and without the ES approximation. Referring to the upper panel of figure 9, we see that the $c_0(t)$ returns to its initial value of (1,0) twice during the collision. In fact, it is clear that the net action for this trajectory is almost exactly zero. That is, at this impact parameter the attractive and repulsive parts of the potential exactly balance each other on the incoming and outgoing portions of the classical path. We can see that initially $c_0(t)$ rotates in a counter-clockwise sense until the repulsive part of the potential is reached. At this point the potential becomes positive and $c_0(t)$ retraces its initial path. Note that during this trajectory, the c_1 term always remains small and the evolution of the states is essentially governed by the simplification given in eq.21. The rotation of $c_0(t)$ continues to a point conjugate to the position where the repulsive part of the potential was entered. As the trajectory goes back into the attractive part of the potential, and V_{00} goes negative, the cycle is completed by $c_0(t)$ retracing its path once more back to a point near (1,0). It is this balancing between the attractive and repulsive parts of the potential – which leads to the zero action – that is responsible for the quantum feature seen near θ=40-70° in the CC DCS in figure 1.

Now examine the lower panel of figure 9. The motion begins as in the two-state energy sudden case, however instead of the change in c_1 being directed along a vector $\frac{\pi}{2}$ to the direction of c_0, the motion is pushed further in the counter-clockwise direction due to the presence of the ω_{01} term. This motion is exemplified by eq.25. When the potential becomes positive, instead of retracing itself, as with the ES

model, the c_1 in the full model is pulled out further. That is, the rotation rate in the clockwise direction is slowed by the non-zero ω_{01}. As the particles separate on the outgoing path of the trajectory, the c_1 is again pulled in the counter-clockwise direction and spirals toward the origin. The trajectory once more produces a nearly null action; however, the inclusion of the non-zero frequency, ω_{01}, has slightly shifted the phase of the coefficients. Thus the overall trend of the $c_i(t)$ motion is similar in the two models, but the asymptotic values of the c_i are slightly shifted. This accounts for the shift of the shoulder/hole feature observed in the CC and IOSA DCS.

B. High Impact Parameter Region

We now discuss the scattering dynamics in the impact parameter range, 5.5<b<8.0 bohr. Because this impact parameter range lies in the rainbow scattering region, changes in the opacity functions have a less obvious effect on the shape of the DCS, but have a large effect on the integral cross section. This region also shows the greatest difference between the opacity functions of the full SC calculation and the SC-IOS, and understanding this difference is important to identifying any shortcomings in the IOS approximation.

At the higher impact parameters (b>5.5 bohr) the potential is attractive during the full time-evolution of the system. That is, the trajectory never encounters the repulsive part of the potential. Examination of figure 8 shows that the two-state model does not reproduce the trends in the opacity functions of the SC or SC-IOS. This is very intriguing because in this impact parameter range the asymptotic values of the expansion coefficients, (that is, the opacity functions of figure 4a) show that >90% of the total probability is in the j'=0 and 1 rotational states if

the full dynamics are employed. In addition, figure 4d reveals that for the SC-IOS ~50% of the final state probability is in $j' \geq 2$. In light of this, we see that the two-state model is inappropriate for an understanding of the energy sudden dynamics in this impact parameter region. Accordingly, we set it aside and return to the multi-state methods.

Examination of figures 4a and 4b shows that at impact parameters greater than 5.5 bohr, transitions to the higher rotational states (i.e. $j' \geq 2$) do not occur when ω_{k1} is non-zero. This is due to the energetic separation of the states which manifests itself through the $\exp(i\omega_{k1}t)$ term, which is included in the full SC and in the SC-CS. The effect of the frequency term is most easily seen, perhaps, if one considers the first order perturbation theory limit[37] of the time-dependent scattering:

$$P_{j'} = \left| \int_{-\infty}^{\infty} dt\, V_{0j'}(t) \exp(i\omega_{0j'}t) \right|^2 \hbar^{-2} \qquad (26)$$

This has the form of the Fourier transform of the interaction potential. In general, for simple $V_{0j'}(t)$, this term will decrease as $\omega_{0j'}$ increases; that is, the low frequency terms will dominate. Since in the impact parameter region of interest here – high b – $V_{0j'}(t)<0$ for all time, this is expected to hold. Clearly, the sudden approximation of setting $\omega_{0j'}$ to zero removes this frequency dependence, and the probabilities of all transitions become solely a function of the action integral for the $0 \rightarrow j'$ transition.

Figures 4c and 4d show that a substantial component of the total transition probability is in $j' \geq 2$ for the SC-ES and SC-IOS approximations. We also see from figure 4 that the major differences between the SC and the SC-IOS in the high impact parameter region result from making the ES

approximation. Because of this, we focus on the differences between the full SC and SC-ES methods.

In figure 10 we plot the rotational state probability as a function of time, $P_{j'}(t)$, for the SC and SC-ES models at several impact parameters. At the lower impact parameters the time-dependent probability for $j'=0$ and $j'=1$ are quite similar in both models, as expected from our previous analysis. The summed probabilities into rotational states $j' \geq 2$ are also similar; however, the SC-ES overestimates the probability into $j'=2$. As we move to higher impact parameters (e.g. b=5.0 bohr), again the $j'=0$ and 1 probabilities are similar in the two methods, but it is now becoming clear that the SC-ES is greatly overestimating the transition probability into the higher rotational states.

By b=6 bohr, the dynamics exhibited by the SC and the SC-ES are quite different. The reason for this should be clear from the above discussion. In this impact parameter interval, the interaction potentials (see figure 7) are purely non-positive. Thus, the "sudden" action can accumulate monotonically along the trajectory. This is not necessarily the case for all $V_{0j'}$, but it certainly explains the generally poor performance of the SC-ES in this region. For instance, in the SC method the $P_1(t)$ increases steadily from its initial value of zero to become the dominant transition. In the SC-ES the $P_1(t)$ increases on the incoming part of the trajectory, as in the full SC method, however the $P_1(t)$ reaches its asymptotic value by the mid-point of the trajectory. In both methods the $P_2(t)$ increases steadily and reaches a maximum near the turning point of the trajectory, then falls off to $P_2(t)<0.1$. The difference between the methods is that in the full SC the $P_2(t)$ (along with the continued decrease in $P_0(t)$) relinquishes much of the flux to $P_1(t)$. In the SC-ES, however, because of the removal of the $\exp(i\omega_{k1}t)$ term the states $j'>2$ begin to dominate the total transition probability.

This is the impact parameter region where the IOS approximation performs most poorly. By overestimating the transition probability into the higher rotational states, the IOS approximation no longer provides an adequate representation of the true collision dynamics. It is generally accepted that the IOSA is poor when the scattering is dominated by a strongly attractive potential.[11] Our time-dependent pictures provide a rather striking illustration of this.

IV. Conclusions

In this paper we have explored the collision dynamics for Ar+HF using several computational approaches. We presented time-independent quantum mechanical CC and IOSA results calculated on the Hutson H6 potential for the Ar+HF(v=0) system at a collision energy of 135meV out of an initial rotational state, $|j=0,m=0\rangle$. The differential cross sections obtained using the IOSA differ markedly from the CC differential cross sections. The origin of this discrepancy was investigated using several time-dependent semiclassical methods. With this approach, the effect of each of the decoupling approximations on the dynamics was explored. The intuitive advantage of the time-dependent methods over the the time-independent methods, is that the local (rather than the global) effects of the potential on the scattering dynamics can be observed.

From this work it was found that the biggest deviation of the IOSA from the "exact" CC calculations is due to the inclusion of the energy sudden approximation. Further, it was found that the energy sudden approximation "failed" differently for different impact parameter regions. For $b<5.5$ bohr, in which the repulsive part of the potential is sampled and backwards and sideways scattering dominate, the opacity

functions obtained from the SC-IOS are qualitatively similar to those obtained using the fully coupled SC method. While this qualitative agreement is encouraging, the quantitative differences are sufficiently great to shift features in the DCS by as much as 30°.

An analysis of the time dependence of the dynamics in this low impact parameter region was facilitated by the use of a two-state model calculation. The model data agreed well with the SC calculations, and revealed the same trends on the inclusion of the ES approximation. The model revealed that at one impact parameter in this range the net action along the the classical trajectory will be zero. In the model with the energy sudden approximation included it was found that the zero action trajectory leads to a transition probability for $0 \rightarrow 0$ of essentially unity - necessarily a maximum. With the ES approximation absent, the trend is similar but the maximum shifts slightly to higher impact parameters.

In the impact parameter range b>5.5 bohr, the SC-ES method performs badly when compared to the full SC. The two-state model is no longer appropriate in this region to study the sudden approximation, since it is clear that the energy sudden approximation allows access to higher product rotational states than occur in the full calculation. At these higher impact parameters, the trajectory experiences exclusively an attractive potential. It is the presence of the attractive potential and the energy sudden approximation that artificially couples the system to high j' states in the IOSA; this does not occur to as great an extent for a repulsive encounter.

Finally, we make some remarks on the universality of our findings. As its name implies, the accuracy of the "sudden" approximation depends on the time scales involved during the collision. At the collision energy used here, the

collision time is on the order of 2×10^4 au. This is comparable with the classical rotational period for an HF molecule in its j=1 state, 3.354×10^4 au. Therefore, for the system at hand, the IOSA is unlikely to be accurate, even for the $j=0\rightarrow j'=1$ transition, at collision energies less than 1 eV. Similarly, one would expect the sudden approximation to perform better in calculations with lighter rare gas atoms, but worse with heavier ones. Our findings here and previously[9] indicate that the IOSA is unlikely to prove a useful tool in improving potential surfaces for rare gas+hydrogen halide scattering for the experimental conditions presently accessible.

References

1. J. C. Polanyi and K. B. Woodall, J. Chem. Phys., **56**, 1563 (1963)

2. J. M. Hutson, Ann. Rev. Phys. Chem., **41**, 123 (1990), and references therein.

3. J. M. Hutson, J. Chem. Phys., **96**, 6752 (1992)

4. C. M. Lovejoy and D. J. Nesbitt, J. Chem. Phys., **91**, 2790 (1989);
   J. M. Hutson and B. J. Howard, Mol. Phys., **45**, 769 (1982);
   ibid., 791 (1982); *ibid.*, **43**, 493 (1981).

5. M. Faubel, K. H. Kohl, J. P. Toennies, K. T. Tang and Y. Y. Yung, Faraday Disc., **73**, 205 (1982).

6. S. D. Jones, J. E. Shirley, M. T. Vonk, C. F. Giese and W. R. Gentry, J. Chem. Phys., **97**, 7831 (1992);
   A. G. Suits, L. S. Bontuyan, P. L. Houston and B. J. Whitaker, J. Chem. Phys., **96**, 8618 (1992);
   P. L. Jones, E. Gottwald, U. Hefter and K. Bergmann, J. Chem. Phys., **78**, 3838 (1983);
   U. Hefter, P. L. Jones, A. Mattheus, J. Witt, K. Bergmann and R. Schinke, Phys. Rev. Lett., **46**, 915 (1981);
   K. Bergmann, U. Hefter, A. Mattheus and J. Witt, Chem. Phys. Lett., **78**, 61 (1981);
   J. A. Serri, A. M. Morales, W. Moskowitz, D. E. Pritchard, C. H. Becker and J. L. Kinsey, J. Chem. Phys., **72**, 6304 (1980);
   K. Bergmann, U. Hefter and J. Witt, *ibid.*, 4777 (1980)

7. M. A. Dvorak, S. W. Reeve, W. A. Burns, A. Grushow and K. R. Leopold, Chem. Phys. Lett., **185**, 399 (1991);
   J. T. Farrell, Jr., O. Sneh, A. E. W. Knight, and D. J. Nesbitt, (Unpublished results)

8. L. J. Rawluk, Y. B. Fan, Y. Apelblat and M. Keil, J. Chem. Phys., **94**, 4205 (1991)

9. L. J. Rawluk, M. Keil, M. H. Alexander, H. R. Mayne and J. J.C. Barrett, Chem. Phys. Lett., **202**, 293 (1993)

10. H. R. Mayne and M. Keil, J. Phys. Chem., **88**, 883 (1984)

11. R. Schinke and J. M. Bowman, in "Dynamics of Molecular Collisions", ed. J. M. Bowman (Springer, Berlin, 1982), Chap. 4

12. J. J.C. Barrett, H. R. Mayne and M. Keil, J. Chem. Phys. (in press, 1994)

13. R. T Pack, J. Chem. Phys., **60**, 633 (1974)

14. G. A. Parker and R. T Pack, J. Chem. Phys., **68**, 1585 (1978)

15. H. J. Korsch and R. Schinke, J. Chem. Phys., **75**, 3850 (1981)

16. H. J. Korsch and R. Schinke, J. Chem. Phys., **73**, 1222 (1980)

17. A. S. Dickinson, Comp. Phys Comm., **17**, 51 (1979)

18. A. P. Clark, A. S. Dickinson and D. Richards, Adv. Chem. Phys., **36**, 63 (1977)

19. G. G. Balint-Kurti, *International Review of Science, Physical Chemistry*, Ser. 2, ed. W. Byers Brown, Butterworth, London; vol. 1, 285 (1975)

20. T. Mulloney and G. C. Schatz, Chem. Phys., **45**, 213 (1980)

21. HIBRIDON is a package of programs for the time-independent treatment of inelastic collisions and photodissociation written by M. H. Alexander, D. E. Manolopoulos, H.-J. Werner, and B. Follmeg, with contributions by P. F. Vohralik, D. Lemoine, G. Corey, B. Johnson, T. Orlikowski, W. Kearney, A. Berning, A. Degli-Esposti, C. Rist and P. Dagdigian

22. G. D. Billing, Comp. Phys. Rep., **1**, 237 (1989)

23. R. B. Gerber and R. Alimi, Israel J. Chem., **31**, 383 (1991)

24. A. E. DePristo, J. Chem. Phys., **78**, 1237 (1983)

25. D. Bohm, *Quantum Theory*, Dover Publication, Inc., New York, 1989, Chap. 18, 407-409

26. A. M. Arthurs and A. Dalgarno, Proc. Roy. Lond. A, **256**, 540 (1960)

27. J. M. Hutson and B. J. Howard, Mol. Phys., **45**, 791 (1982);
C. Douketis, J. M. Hutson, B. J. Orr and G. Scoles, Mol. Phys., **52**, 763 (1984);
D. J. Nesbitt, M. S. Child, and D. C. Clary, J. Chem. Phys., **90**, 4855 (1989)

28. J. M. Hutson, Private communication to MK (1993)

29. R. D. Levine and R. B. Bernstein, *Molecular Reaction Dynamics and Chemical Reactivity*, (Oxford University Press, 1987), p. 861

30. M. S. Child, *Molecular Collision Theory*, Academic Press, New York (1974), pp. 141-148

31. D. Chase, Phys. Rev., **104**, 838 (1956)

32. J. M. Bowman and S. C. Leasure, J. Chem. Phys., **66**, 288 (1977)

33. C. F. Curtiss and F. T. Adler, J. Chem. Phys., **20**, 249 (1952);
G. Gioumousis and C. F. Curtiss, J. Math. Phys., **2**, 96 (1961);
L. W. Hunter and C. F. Curtiss, J. Chem. Phys., **58**, 3884 (1973);
M. Pattengill, J. Chem. Phys., **66**, 5042 (1977)

34. P. McGuire, Chem. Phys. Lett., **23**, 575 (1973);
P. McGuire and D. J. Kouri, J. Chem. Phys., **60**, 2488 (1974);
Y. Shimoni and D. J. Kouri, J. Chem. Phys., **65**, 706 (1976);
D. J. Kouri in *Atom-Molecule Collision Theory*, ed. R. B. Bernstein, Plenum Press, NY, (1979), Chap. 9

35. D. Secrest, J. Chem. Phys., **62**, 710 (1975)

36. M. V. Berry and K. E. Mount, Rep. Prog. Phys., **35**, 315 (1972)

37. G. C. Schatz and M. A. Ratner, *Quantum Mechanics in Chemistry*, Prentice Hall, Engelwood Cliffs, NJ, (1993), p. 60

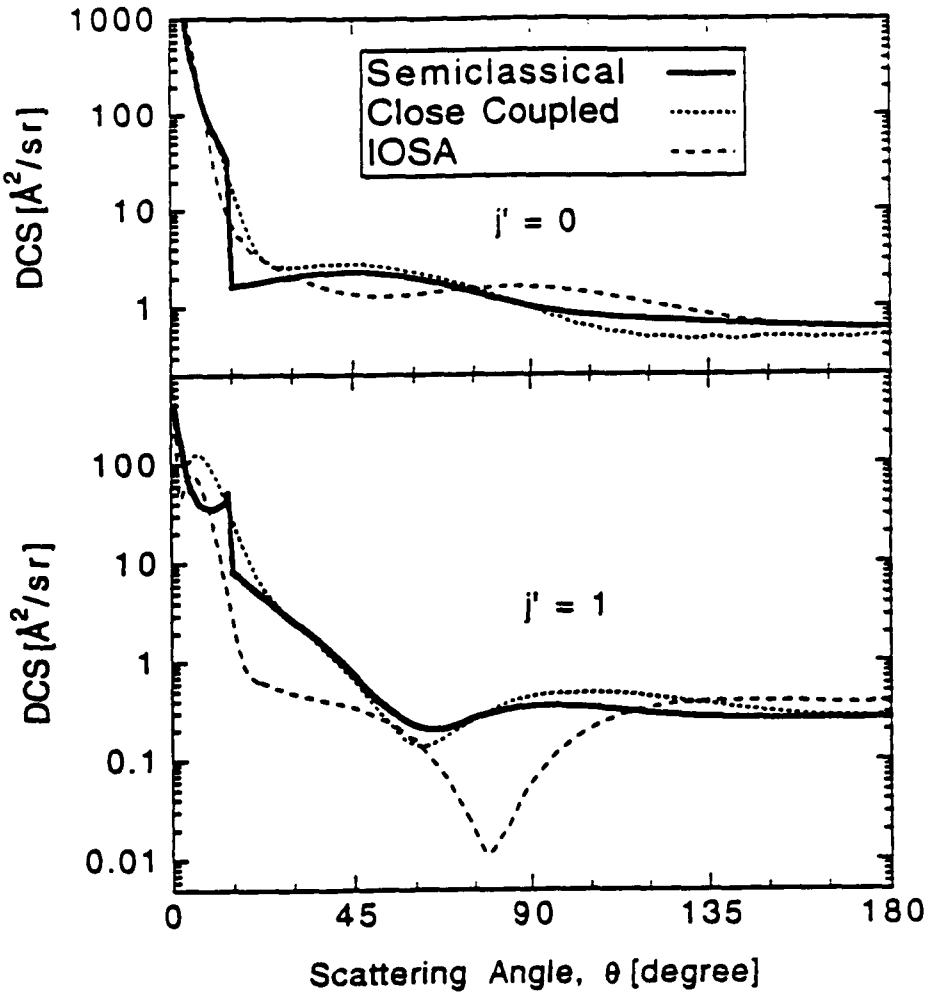

Figure 1. Differential cross sections for Ar+HF(j=0)→Ar+HF(j'=0,1) calculated using the full semiclassical, quantum CC and IOSA formalisms. Relative collision energy, E_{coll} = 135 meV. Note that the CC and IOSA results have been smoothed using a 2° angular averaging function to suppress high frequency oscillations.

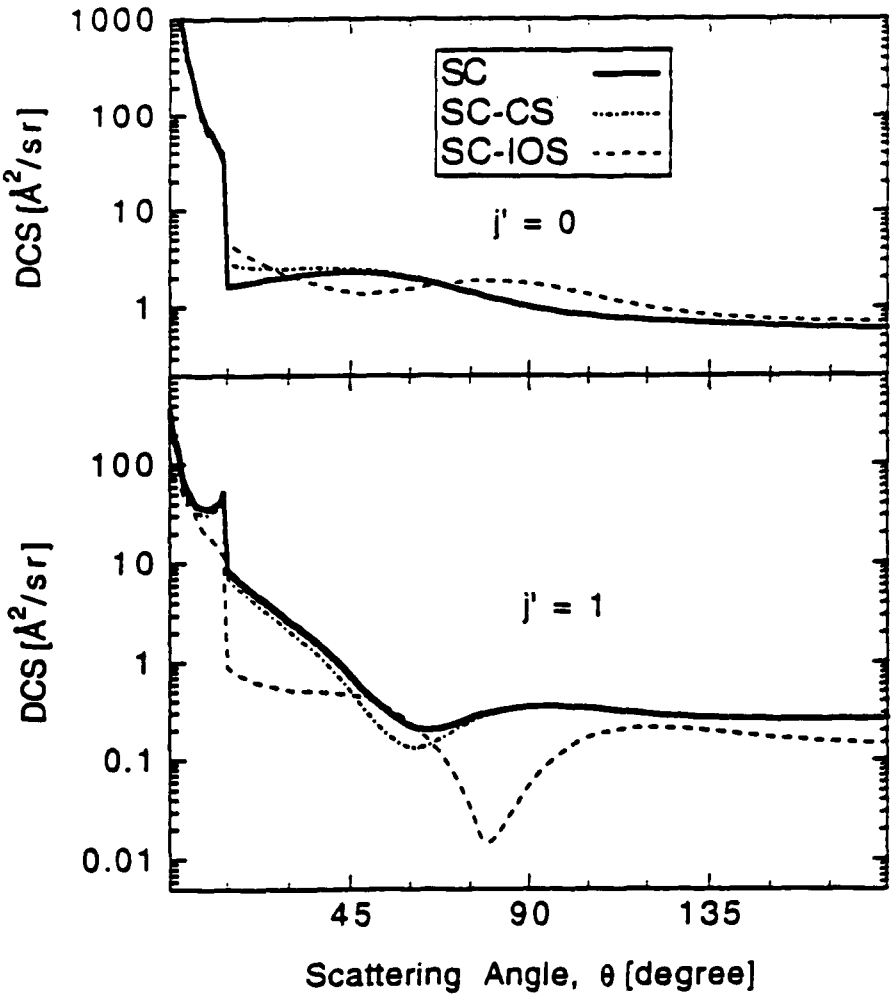

Figure 2. Differential cross sections calculated using the full semiclassical method and indicated approximations. Collision energy and initial rotational state are as in figure 1.

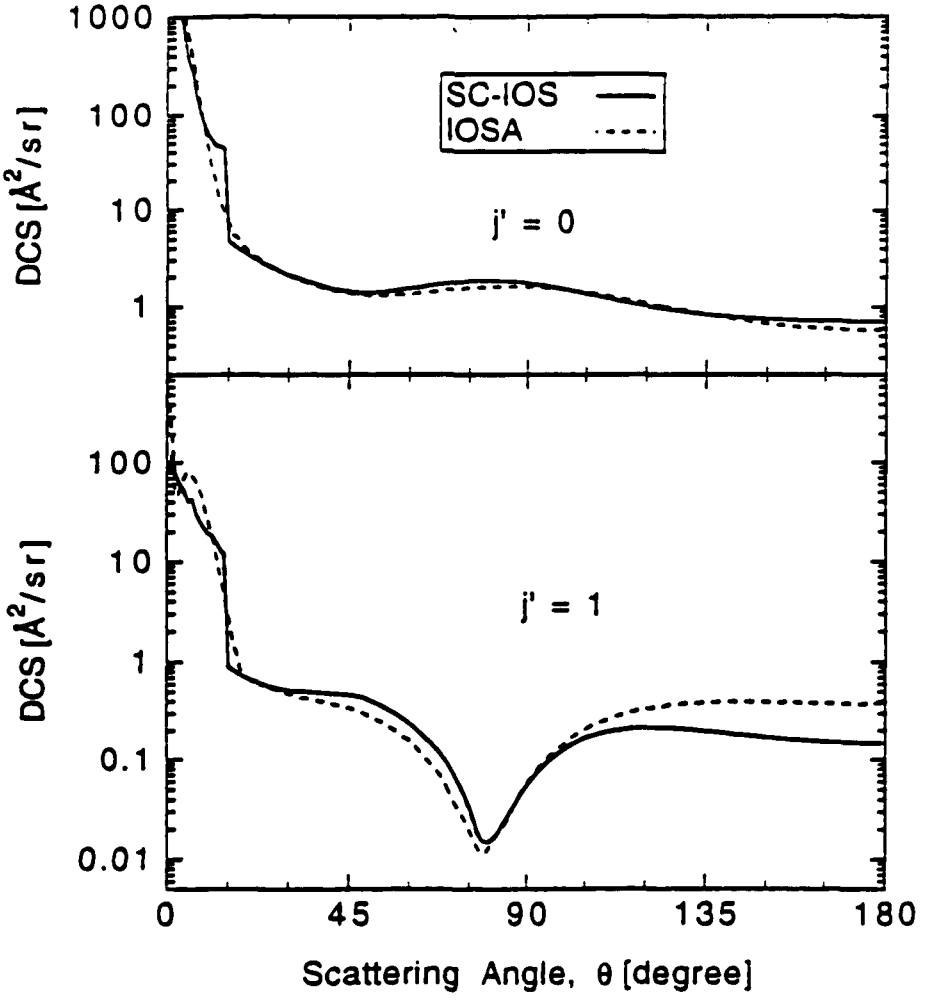

Figure 3. Comparison of DCS from the time-independent quantum IOSA and the semiclassical IOS approximations.

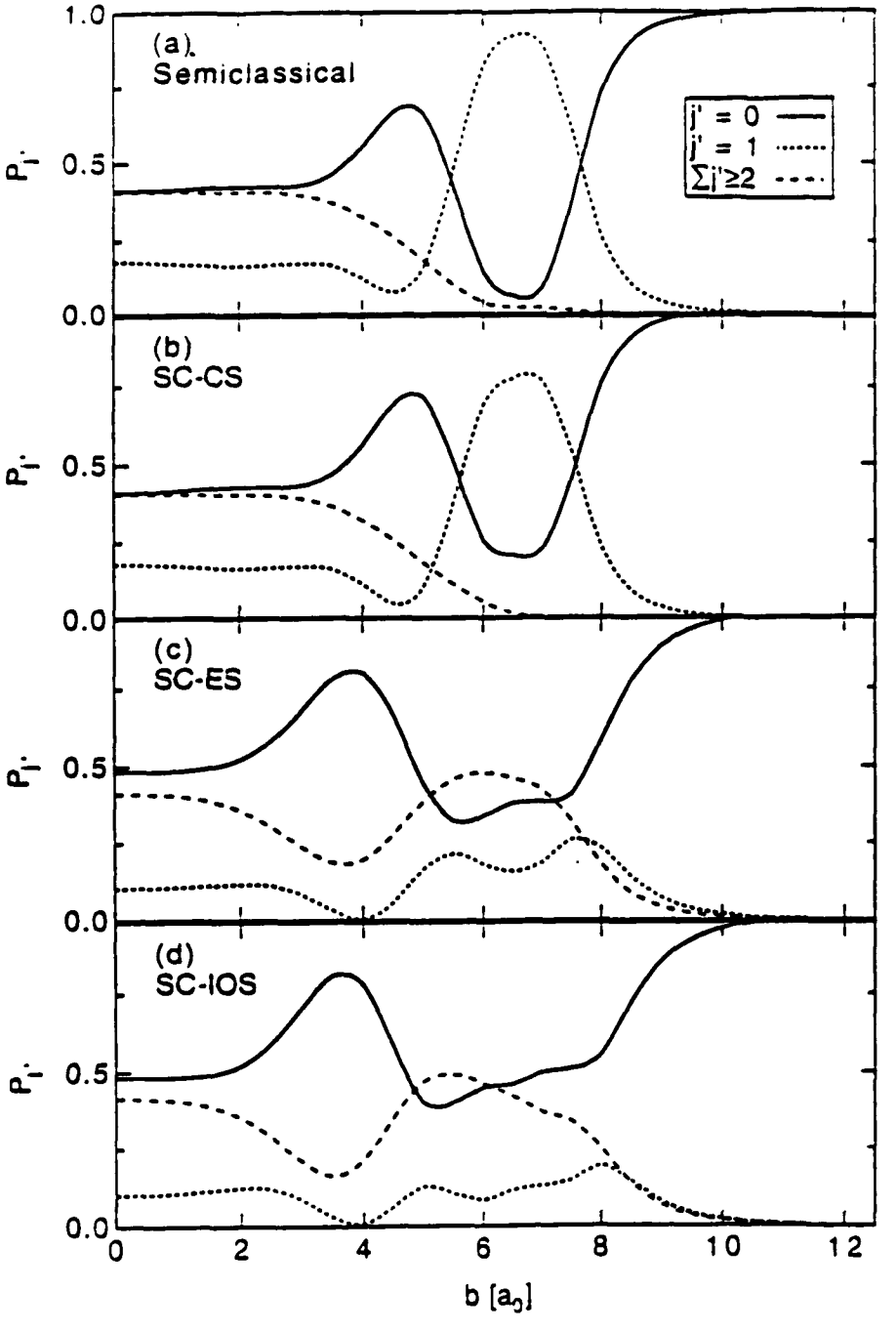

Figure 4. Opacity functions for Ar+HF(j=0)→Ar+HF(j') from: (a)the full semiclassical method; (b)SC-CS; (c)SC-ES; and (d)SC-IOS. The summation refers to the total transition probability into rotational states j'≥2.

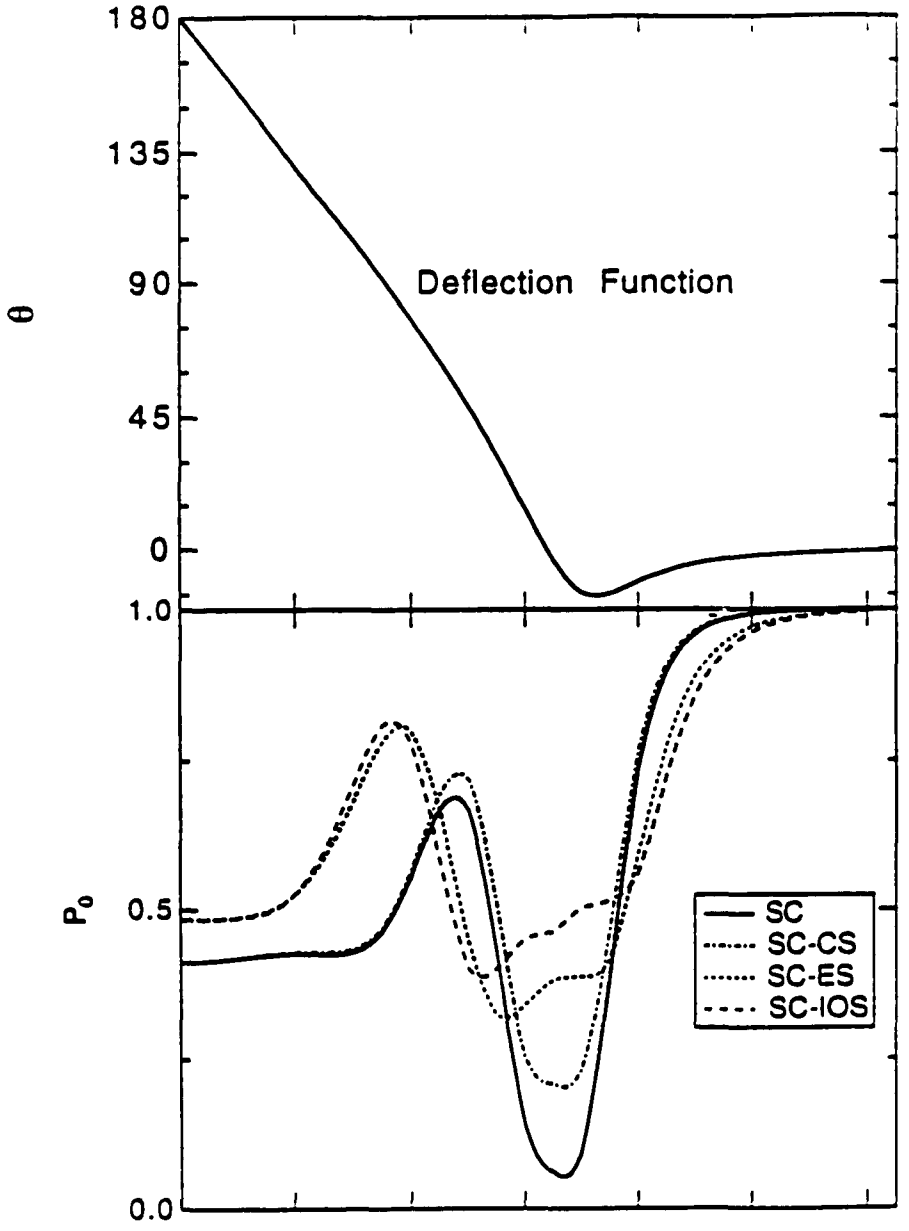

Figure 5. Upper panel: Classical deflection function for elastic Ar+HF(0→0) collision on the Hutson H6 (v=0) surface, used in calculating each of the semiclassical DCS. Lower panel: Comparison of the j'=0 opacity functions from each of the semiclassical approximations.

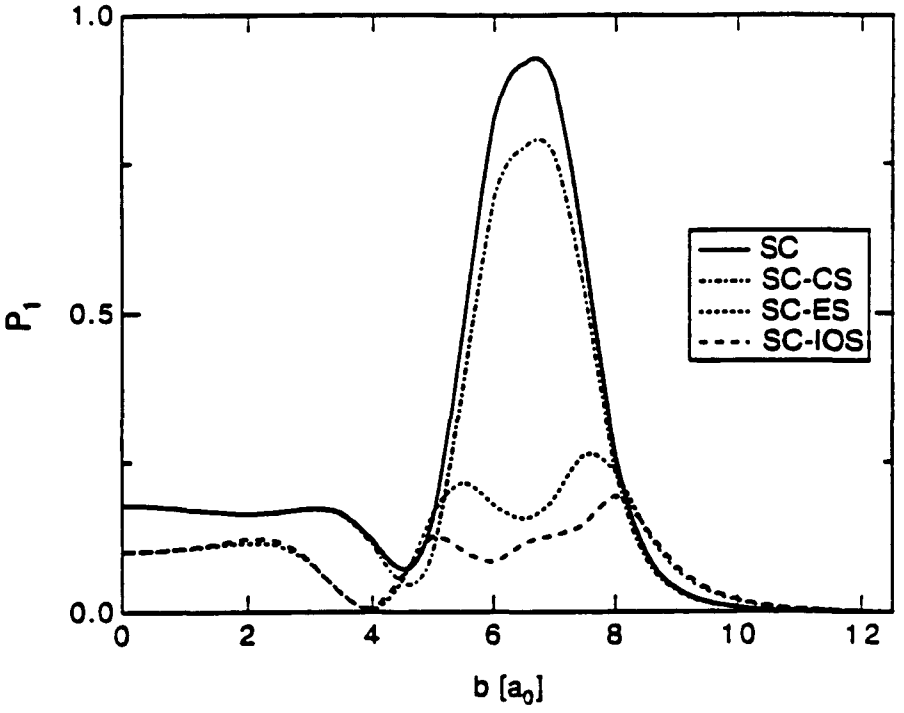

Figure 6. Comparison of the opacity functions for Ar+HF(j=0)→Ar+HF(j'=1) from each of the semiclassical approximations.

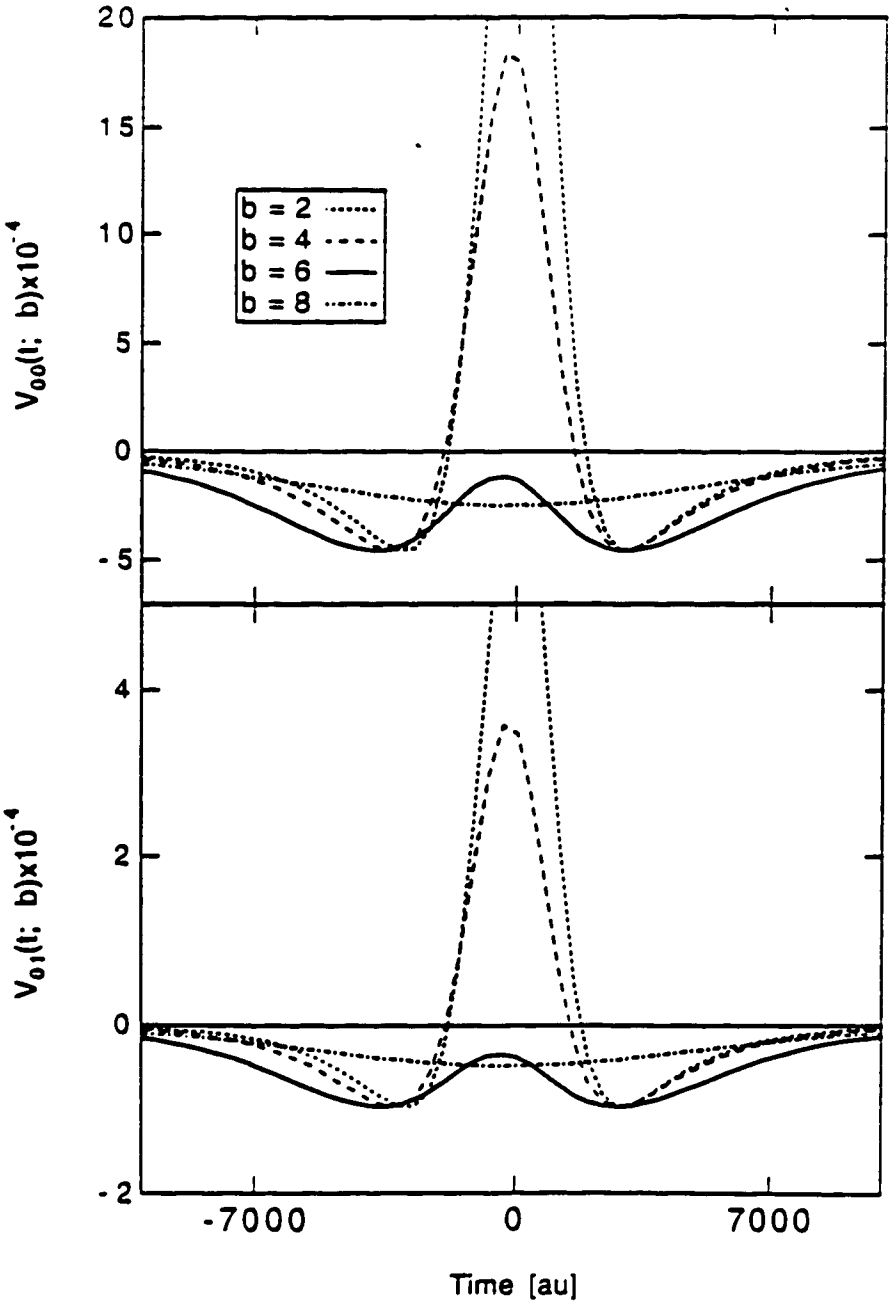

Figure 7. Time-dependent coupling potentials at several impact parameters, b. The upper panel shows <00|V(t)|00>, denoted $V_{00}(t;b)$. The lower panel shows <00|V(t)|10>, denoted $V_{01}(t;b)$.

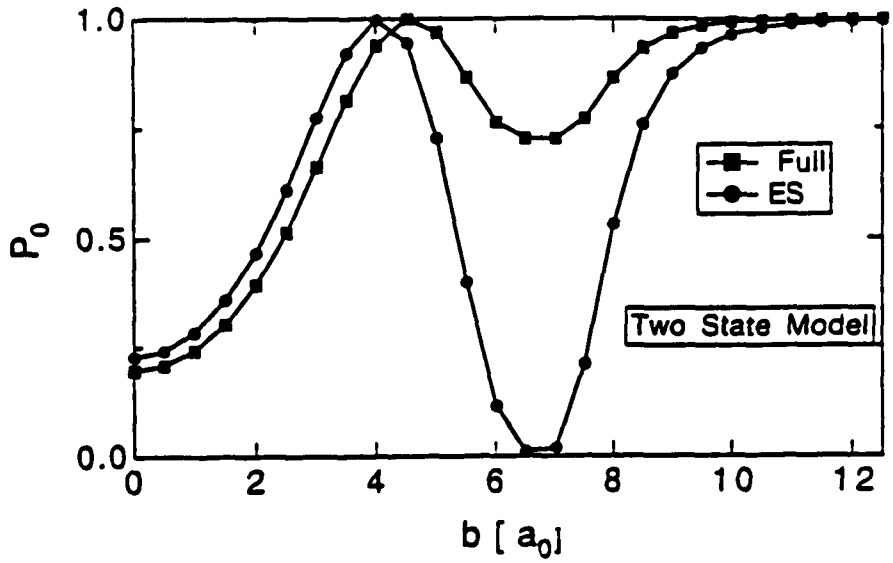

Figure 8. Opacity functions from a two-state model of the Ar+HF collision dynamics. "Full" indicates use of eqs.20; "ES" indicates use of eqs.21.

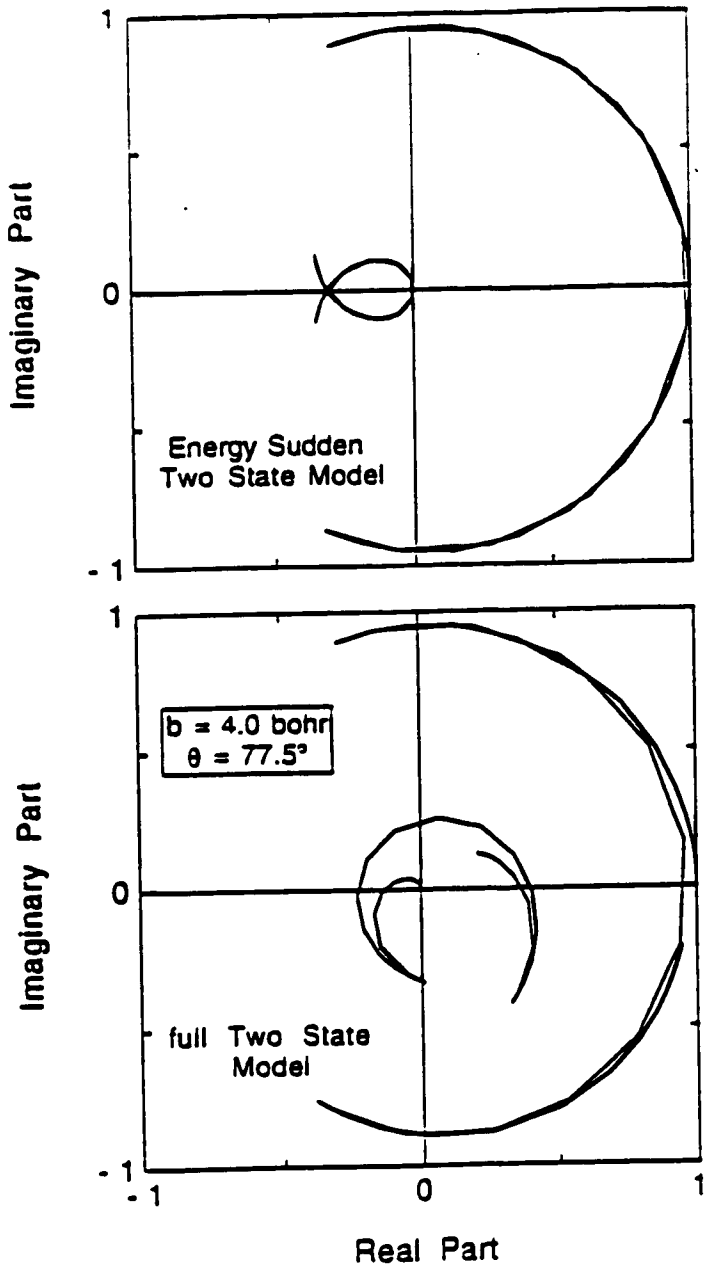

Figure 9. Time evolution of the expansion coefficients c_0 and c_1 from the full (lower panel) and ES (lower panel) two state models at impact parameter, b=4.0 bohr. Initially, c_0 = (1,0), c_1 = (0,0). Thus the outer curve describes the evolution of c_0, the inner curve c_1. The V_{00} potential controlling the dynamics is shown in figure 7. The initial sense of motion is counter-clockwise. At t=-2400 au, V_{00} changes sign, as does the sense of motion. The next reversal occurs at t=2400 au.

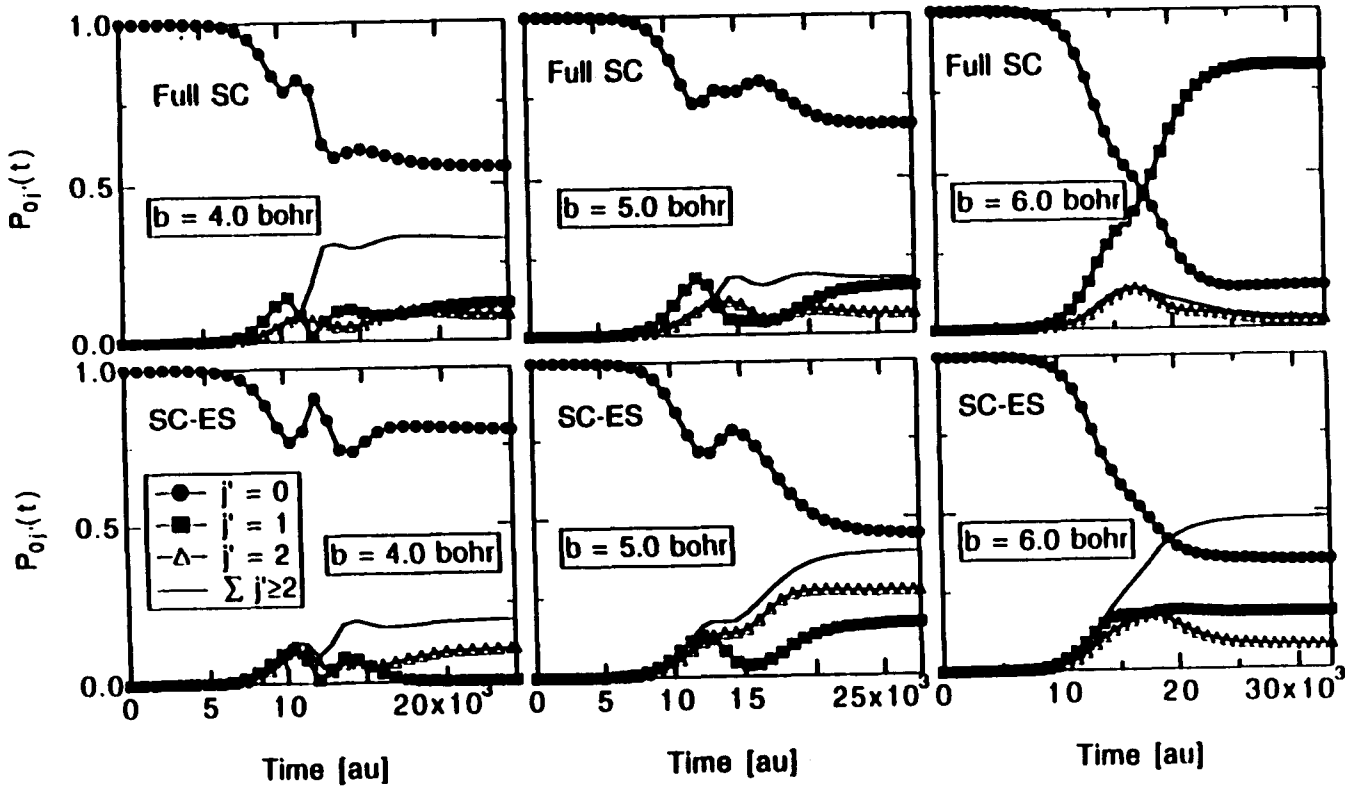

Figure 10. Time evolution of rotational state probability from the full SC and the SC-ES models. In both cases the summation refers to the total probability for rotational states, $j' \geq 2$. Note different time scales for each impact parameter.

Appendix

Ar + HF Classical Trajectories - Differential Cross Section in the Laboratory Frame

I. Calculation of the Differential Cross section in the Lab Frame

For the Ar+HF scattering study that we are conducting we simulate the scattering experiment of Rawluk, et al.[1] A crossed molecular beam scattering apparatus with final rotational state selective detection of the scattered HF is used in this experiment. The scattered HF is detected in the plane defined by the initial molecular beams. The detection system is a "flux detector"; that is, the detection is independent of the final HF velocity.[2]

To simulate this experiment we sample our initial trajectory conditions over the experimental beam conditions. This includes the velocity and angular distribution of the molecular beams and the initial rotational state distribution in the HF beam. All of the HF is initially in the ground

vibrational state and the collision energy of the experiment is below the threshold for vibrational excitation. The beam conditions are given in Table 1. The initial rotational state distribution of the HF is given in Table 2.

The relationship between the center of mass (CoM) frame and the laboratory (Lab) frame is given in the Newton diagram of Figure 1. Using the convention of Toennies,[3] we designate the CoM velocity vectors with **u** and the lab velocity vectors with **v**. Subscripts 1 and 2 refer to the primary (detected) and secondary beams, respectively. Primes (') indicate final velocity vectors. Upper case Greek letters refer to lab angles, lower case to CoM angles. The angle ε is given as the angle between **v'** and **u'**. Due to the cylindrical symmetry of the scattering about $\mathbf{v_r}$ in the CoM frame, the in-plane scattering case leads to two final lab scattering vectors for each CoM trajectory. In general, this will lead to a "fast" and a "slow" lab scattering vector, we describe these with a subscript f or s, respectively. (0,1 or 2 of these final vectors may contribute to the "observed" lab signal.)

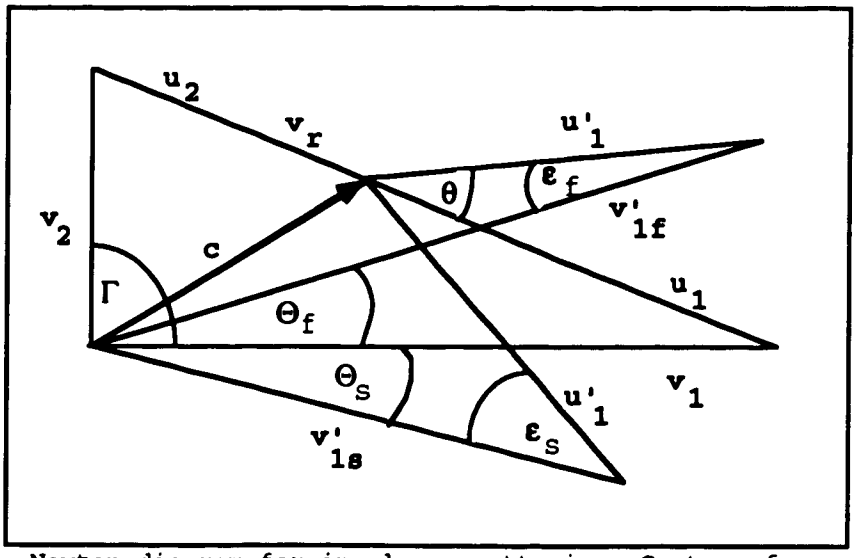

Figure 1. Newton diagram for in-plane scattering. Center of mass motion vector designated as **c**, beam intersection angle as Γ. The angles θ and Θ are the CoM and lab scattering angles, respectively. Other labels are defined in the text. Arrows on most vectors have been omitted for viewing clarity.

To calculate the scattered intensity into a final HF rotational state, j', we need to integrate over all initial conditions. This leads to the expression

$$I_{j'} = K\int_0^{\infty}\int_{\tilde{j}=0}^{\infty} v_r \sigma_{j'}(v_r) p(v_r) h(\tilde{j})\, d\tilde{j}\, dv_r \qquad (1)$$

where v_r is the relative collision velocity; $\sigma_{j'}$ is the v_r dependent, final-state-selected total cross section for j'; p is the density function for v_r; h is the initial rotational state distribution function and the tilde (~) indicates a continuous variable; and K is a constant containing the particle density of the beams and the collision volume.

Normalization over the initial rotational state distribution is given by

$$\int_{\tilde{j}=0}^{\infty} h(\tilde{j})\, d\tilde{j} = 1 \qquad (2)$$

(Note: The initial distribution of HF rotational states is non-continuous function over the integer values, j. Therefore, the integration over $\tilde{j}$ should be replaced by a summation over j

$$\sum_{j=0}^{j_{max}} h_j(j) = 1 \qquad (3)$$

where the h_j are taken from the percent distribution of initial rotational states in Table 2.)

The relative collision velocity is a direct function of the initial beam velocity distribution densities and the

angular divergence of the beams. The beam divergence functions may be combined into an intersection angle density function, $f(\Gamma)$. The velocity densities for the primary and secondary beams may be given as $f(v_1)$ and $f(v_2)$, respectively. The function $p(v_r)$ may now be written as a product of the density functions

$$p(v_r) = f(v_1)f(v_2)f(\Gamma) \tag{4}$$

Using equation 4 in equation 1 and including the summation over the initial rotational state distribution, equation 3, we can write the state selected scattering intensity as

$$I_{j'} = K\sum_{j=0}^{j_{max}} h_j(j)\int_0^\infty\int_0^\infty\int_0^\pi v_r(v_1, v_2, \Gamma)\sigma_{j'}\left[\, v_r(v_1, v_2, \Gamma)\right] f(v_1)f(v_2)f(\Gamma)\, d\Gamma\, dv_2\, dv_1 \tag{5}$$

indicating v_r as a function of v_1, v_2, and Γ. The normalization over the functions, f, is given by

$$\int_0^\infty\int_0^\infty\int_0^\pi f(v_1)f(v_2)f(\Gamma)\, d\Gamma\, dv_2\, dv_1 = 1 \tag{6}$$

The type of CoM differential cross section employed in this study is the over the CoM solid angle, ω, and the recoil velocity u', denoted as, $d^3\sigma/d^2\omega du'$. The relation between the recoil CoM velocity function, $f(u_1')$ and the cross section, σ_r, is given by Warnock and Bernstein[2] as

$$\frac{d^3\sigma(v_r)}{d\omega\, du'} = \sigma(v_r)f(u')u'^2 \tag{7}$$

The normalization for this function over the CoM coordinates is

$$\sigma(v_r) = \int_0^{\infty} \int_0^{2\pi} \int_0^{\pi} \left[\frac{d^3\sigma(v_r)}{d^2\omega\, du} \right] \sin\theta\, d\theta\, d\phi\, du \qquad (8)$$

In order to simplify the notation of equation 5, we will condense the integration (and summation) over all of the initial conditions in to a single function Q, such that

$$\int_q Q\, dQ = \sum_{j=0}^{j_{max}} h_j(j) \int_0^{\infty} \int_0^{\infty} \int_0^{\pi} f(v_1) f(v_2) f(\Gamma)\, d\Gamma\, dv_2\, dv_1 \qquad (9)$$

where dQ indicates the sum and integration over all variables contained in Q. Doing this does not imply a loss of generality for the integration, it is only done for the sake of simplifying the notation. If one substitutes equation into equation 5 and uses the simplification of equation 9, then

$$I_{j'} = K \int_q \int_0^{\infty} \int_0^{2\pi} \int_0^{\pi} v_r Q \left[\frac{d^3\sigma_{j'}(v_r)}{d^2\omega\, du'} \right] \sin\theta\, d\theta\, d\phi\, du'\, dQ \qquad (10)$$

where the dependence of v_r on v_1, v_2, and Γ still exists, but is not explicitly shown.

After transformation of equation 10 into the lab frame and conversion of the intensity to a cross section (details are given in the next section), the average lab DCS is given by

$$\left\langle \frac{d^2\sigma}{d^2\Omega_d} \right\rangle_{j'} = N \int_q n\, v_r Q \sigma_{j'}(v_r) \sum_k P_{j'}\left[\theta(v_k, \Phi_d, \Theta_d)\right] \frac{v_k'^2}{u_k'^2} \left| \frac{1}{\cos\varepsilon_k} \right| dQ \qquad (11)$$

where $P_{j'}$ is the transition probability into a final HF rotational state into the lab solid angle, Ω_d as a function of CoM scattering θ and N is an appropriate normalization

constant. The summation over k refers to the contribution of each CoM trajectory (0,1, or 2) to the lab frame DCS. The n is a factor related to the relative collision velocity.

The integration over the initial conditions, Q, is carried out by Monte Carlo sampling. The initial rotational state function, h(j), is weighted according to the initial j with percent population given in Table 2. From the percent population distribution a cumulative probability distribution function, ρ_j, is generated

$$\rho_j = \sum_{j=0}^{j} h_j(j) \tag{12}$$

The initial j selection is accomplished by generating a random number on the interval 0→1, ζ. For $\rho_j \leq \zeta < \rho_{j+1}$, the initial rotational state is j.

The distribution functions, f, over the beam velocity distributions and the intersection angle are assumed to be Gaussian. A normalized Gaussian distribution centered at X with standard deviation, σ, in standard form[4] is

$$f_{X,\sigma}(x) = \frac{1}{\sigma\sqrt{2\pi}} \exp\left(\frac{-(x-X)^2}{2\sigma^2}\right) \tag{13}$$

A normalized Gaussian random number, ξ, is generated from two random numbers selected on the interval 0→1, ζ_1 and ζ_2, using

$$\xi = \sqrt{-2\ln(\zeta_1)} * \cos(2\pi\zeta_2) \tag{14}$$

A random value of a function, $f(x)$, from a normalized Gaussian distribution is then generated by

$$f(x) = X + \xi * \sigma \tag{15}$$

(Note: FWHM = $\sigma * 2\sqrt{2\ln 2}$.) For the mean and FWHM for the beam velocity and intersection angle distributions refer to Table 1.

A trajectory is calculated in the center of mass (CoM) frame using standard methods[5] to select the initial orientation of the diatom and position of the atom. A Gear (variable step size) integrator is used to solve Hamilton's equations of motion for the trajectory. The exception to the standard methods of reference 5 is the method for selection of the impact parameter, b. To choose b the linear sampling method of Barg et al.[6] is employed. In this method the orbital angular momentum range, ℓ=0-ℓ_{max}, is divided into L $\Delta\ell$-intervals and b selected linearly within each interval. Therefore, each trajectory has a weighting of $(2\ell+1)$.

In the actual trajectory calculation b and the relative collision velocity are selected as independent functions. The ℓ weighting for each trajectory is generated as a continuous function of b and v_r. From the relationship

$$b^2 = \left(\frac{\hbar}{P}\right)^2 \ell(\ell+1) \tag{16}$$

where P is the initial relative momentum, the "continuous" variable, $\tilde{\ell}$, is given by

$$\tilde{\ell} = \sqrt{\frac{b^2P^2}{\hbar^2} + 0.25} - 0.5 \tag{17}$$

and the $(2\tilde{\ell}+1)$ weighting as a function of b and v_r is simply

$$2\tilde{\ell} + 1 = 2\sqrt{\frac{b^2P^2}{\hbar^2} + 0.25} \tag{18}$$

The CoM trajectory is transformed into the lab frame directly, prior to any boxing of the final conditions. On transformation the Jacobian for the trajectory is combined with the CoM scattering angle weighting of $\frac{1}{\sin\theta}$. This produces a transformation weighting factor of

$$w\left(\Theta(\theta)\right) = \frac{v'^2}{u'^2}\left|\frac{1}{\cos\varepsilon}\right|\frac{1}{\sin\theta} \tag{19}$$

Equation 19 along with equation 18 give the correctly weighted contribution, $W(\Theta)_i$, of i^{th} trajectory to the Lab frame DCS

$$W(\Theta)_i = w\left(\Theta(\theta)\right) * \left(2\tilde{\ell} + 1\right) \tag{20}$$

The results of the trajectory are then "boxed" by final rotational state and scattering angle. The final rotational energy from the classical trajectory is continuous. The quantum relation for the final rotational state is

$$\tilde{j}'\left(\tilde{j}'+1\right) = \tilde{J}^2 \tag{21}$$

where $\tilde{J}$ is the length of the classical rotational vector. Solving equation 21 gives the continuous "quantum" number of the final rotational state as

$$\tilde{j}' = \sqrt{\tilde{J}^2 + 0.25} - 0.5 \tag{22}$$

The final rotational state, $\tilde{j}'$, is then boxed to the nearest integer state, j'. For example $\tilde{j}' \leq 0.5$, goes into the j'=0 box; $0.5 < \tilde{j}' \leq 1.5$, goes in the j'=1 box, etc.

The scattering angle, Θ, is boxed using a fixed box size or a variable box size method. The fixed box size method

divides the angular range into equally spaced boxes (typically a $\Delta\Theta$=5° width). The variable box size method divides the angular range such that each angular box holds an equal number of trajectories. The advantage of the variable box size method is that regions of high scattering density are finely divided to reveal structure in the cross section, while regions of sparse density are highly averaged to reduce the relative error.

The trajectory weightings, $W(\Theta)_i$, are now boxed and summed over all trajectories within an ℓ-interval, n_l. This sum is then transformed into an ℓ-weighted transition probability by multiplying by the normalization factor

$$N_l = \frac{\Delta\ell}{n_l} \tag{23}$$

where $\Delta\ell$ is the width of the ℓ-interval. Summation over all ℓ-intervals gives the final state selected transition probability

$$P_{j'}(\Theta_k) = \sum_{l=0}^{L} N_l \sum_{i=1}^{n_l} W_{j'}(\Theta_k)_i \tag{24}$$

Finally, the transition probability is converted into the average lab DCS by multiplication by the factor related to the average relative collision velocity

$$\left\langle \frac{d^2\sigma}{d^2\Omega_d} \right\rangle_{j',\Theta_k} = \frac{\hbar^2}{2p^2\Delta\Theta_k} P_{j'}(\Theta_k) \tag{25}$$

II. Center of Mass to Laboratory Frame Jacobian

In this section the details of converting the CoM DCS into Lab DCS are covered. To accomplish this, the integration of equation 10 over CoM variables, (θ,ϕ,u'), is transformed into the lab variables (Φ,Θ,v'). The Jacobian of this transformation is given by

$$\frac{\partial(\theta,\phi,u')}{\partial(\Phi,\Theta,v')} = \frac{v'^2}{u'^2}\frac{\cos\Phi}{\sin\theta} \tag{26}$$

Use of equations 10 and 26 gives the lab frame signal intensity as

$$I_{j'} = K\int_q\int_0^\infty\int_{-\pi}^{\pi}\int_{-\pi/2}^{\pi/2} v_r Q\left[\frac{d^3\sigma_{j'}(v_r)}{d^2\omega\,du'}\right]\frac{v'^2}{u'^2}\cos\Phi\,d\Phi\,d\Theta\,dv'\,dQ \tag{27}$$

To condense notation, we write the integration over the lab coordinates as $\cos\Phi d\Phi d\Theta = d^2\Omega$, and equation 27 simplifies to

$$I_{j'} = K\int_q\int_0^\infty\int_\Omega v_r Q\left[\frac{d^3\sigma_{j'}(v_r)}{d^2\omega\,du'}\right]\frac{v'^2}{u'^2}d^2\Omega\,dv'\,dQ \tag{28}$$

where the integration over Ω represents the integration over Φ and Θ.

The scattered flux into the solid angle subtended by the detector, $\delta^2\Omega_d = \langle\cos\Phi_d\rangle\delta\Phi_d\delta\Theta_d$, is given by

$$\delta^2 I_{j'}(\Phi_d,\Theta_d) = K\delta^2\Omega_d\int_q\int_0^\infty v_r Q\left[\frac{d^3\sigma_{j'}(v_r)}{d^2\omega\,du'}\right]\frac{v'^2}{u'^2}dv'\,dQ \tag{29}$$

given that the detector current is unity across $\delta^2\Omega_d$ (as is the case for the Keil experiment of reference 1). The differential lab intensity is then given as

$$\frac{\partial^2 I_{j'}(\Phi_d,\Theta_d)}{\partial^2\Omega_d} = K\int_q\int_0^\infty v_r Q\left[\frac{d^3\sigma_{j'}(v_r)}{d^2\omega\, du'}\right]\frac{v'^2}{u'^2}dv'\,dQ \qquad (30)$$

For a given relative collision velocity the average lab differential cross section (DCS) is related to the differential lab intensity by

$$\frac{\partial^2 I(\Phi_d,\Theta_d)}{\partial^2\Omega_d} = Kv_r\left\langle\frac{d^2\sigma}{d^2\Omega}\right\rangle \qquad (31)$$

We now examine the differential cross section, $\frac{d^3\sigma}{d^2\omega du'}$. Recall that there is no ϕ dependence on the scattering function in the CoM, under the experimental conditions of Keil, et al.[1] We now write the differential cross section as

$$\frac{d^3\sigma(v_r)}{d^2\omega\, du'} \equiv \sigma(v_r)u'^2 f(\theta,\phi,u') = N\sigma(v_r)P(\theta,u') \qquad (32)$$

where N is an appropriate normalization constant and P is the scattering probability distribution, $0 \le P \le 1$, for θ and u'.

Using equations 32 and 31 along with equation 30 we may write an expression for the final state selected average lab DCS subtended by the detector solid angle

$$\left\langle\frac{d^2\sigma}{d^2\Omega_d}\right\rangle_{j'} = \int_q N^\dagger\int_0^\infty v_r Q\sigma_{j'}(v_r)P(\theta,u')\frac{v'^2}{u'^2}dv'\,dQ \qquad (33)$$

where $N^\dagger$ is a normalization constant and includes a term which accounts for the dependence of the lab DCS on the relative

collision velocity, which is a function of the initial trajectory conditions.

In equation 33 the scattering probability, P, is dependent upon u' while the integration is over v'. The Jacobian for the transformation between these two variables is obtained from the Newton diagram of Figure 1, and is given by[3]

$$\frac{\partial v'}{\partial u'} = \left|\cos \varepsilon\right|^{-1} \tag{34}$$

Using equation 34 in equation 33, we arrive at equation 11.

References

1. L. J. Rawluk, Y. B. Fan, Y. Apelblat and M. Keil, J. Chem. Phys., **94**, 4205 (1991)

2. T. T. Warnock and R. B. Bernstein, J. Chem. Phys., **49**, 1878 (1968) For a "flux detector" the signal is independent of the particle velocity. For a "density detector" the signal is inversely proportional o the final particle velocity.

3. J. P. Toennies, Chap. 5, "Physical Chemistry - An Advanced Treatise", v. 6A, ed. H. Eyring, D. Henderson and W. Jost, Academic Press, New York, NY (1974)

4. J. R. Taylor, "An Introduction to Error Analysis", University Science Books, Mill Valley, CA, (1982), p. 112

5. L. M. Raff and D. L. Thompson, "Theory of Chemical Reaction Dynamics, v. III; Chap. 1, ed. M. Bear, CRC Press International, Boca Raton, FL, 1985

6. G. D. Barg, G. M. Kendall, J. P. Toennies, Chem. Phys., **16**, 243 (1976)

Table 1. Ar and HF beam conditions from Rawluk, et al. experiment. Γ is the intersection angle of the two beams in the Lab frame.

	HF[km/s]	Ar[km/s]	Γ[deg]
mean	1.21	0.559	90
FWHM	0.2408	0.0414	3.999

Table 2. Initial rotational state distribution in the HF beam of the experiment of reference 1 given as a percent of the total molecules in the beam.

j	%
0	28
1	37
2	21
3	10
4	3.2
5	0.8

List of References

M. Abramowitz and I. A. Stegun, *Handbook of Mathematical Functions with Formulas, Graphs and Mathematical Tables*, NBS, Applied Mathematics Series, **#55**, (1964), p. 878

R. Ahlichs, R. Penco and G. Scoles, Chem. Phys., **19**, 119 (1977)

M. H. Alexander, J. Chem. Phys., **95**, 8931 (1991)

M. H. Alexander, J. Chem. Phys., **96**, 6672 (1992)

J. Andres, U. Buck, F. Huisken, J. Schleusener and F. Torello, J. Chem. Phys., **73**, 1512 (1980)

J. Andres, U. Buck, F. Huisken, J. Schleusener and F. Torello, J. Chem. Phys., **73**, 5629 (1980)

A. M. Arthurs and A. Dalgarno, Proc. Roy. Lond. A, **256**, 540 (1960)

R. A. Aziz, *Inert Gases*, Springer Series in Chemical Physics, ed. M. L. Klein, Springer, Berlin (1984) 34, Chap. 2

M. Baer, H. R. Mayne, V. Khare and D. J. Kouri, Chem. Phys. Lett., **72**, 269 (1980)

G. G. Balint-Kurti, *International Review of Science, Physical Chemistry, Ser. 2*, ed.

G. D. Barg, G. M. Kendall and J. P. Toennies, Chem. Phys., **16**, 243 (1976)

J. A. Barnes, M. Keil, R. E. Kutina and J. C. Polanyi, J. Chem. Phys., **72**, 6306 (1980)

J. A. Barnes, M. Keil, R. E. Kutina and J. C. Polanyi, J. Chem. Phys., **76**, 913 (1982)

J. J. Barrett and H. R. Mayne, Chem. Phys. Res., **1**, 85 (1990)

J. J. C. Barrett, H. R. Mayne and M. Keil, J. Chem. Phys., (in press, 1994)

J. J. C. Barrett, H. R. Mayne, M. Keil and L. J. Rawluk, Can. J. Chem., (in press, 1994)

D. R. Bates, *Atomic and Molecular Processes*, (Academic Press, 1962), Chap.4

D. Beck, U. Ross and W. Schepper, Phys. Rev. A, **19**, 2173 (1979)

D. Beck, U. Ross and W. Schepper, Z. Phys., **A293**, 107 (1979)

C. H. Becker, P. W. Tiedemann. J. J. Valentini and Y. T. Lee, J. Chem. Phys., **71**, 481 (1979)

L. Beneventi, P. Casavecchia, F. Vecchiocattivi, G. G. Volpi, D. Lemoine, and M. H. Alexander, J. Chem. Phys., **89**, 3505 (1988)

K. Bergmann, R. Engelhardt, U. Hefter and J. Witt, J. Chem. Phys., **71**, 2726 (1979)

K. Bergmann, U. Hefter and J. Witt, J. Chem. Phys., **72**, 4777 (1980)

K. Bergmann, U. Hefter, A. Mattheus and J. Witt, Chem. Phys. Lett., **78**, 61 (1981)

M. V. Berry and K. E. Mount, Rep. Prog. Phys., **35**, 315 (1972)

G. D. Billing, Comp. Phys. Rep., **1**, 237 (1984)

J. S. Binkley and J. A. Pople, Int. J. Quant. Chem., **9**, 229 (1975);

D. Bohm, *Quantum Theory*, Dover Publication, Inc., New York, (1989), Chap. 18, pp. 407-409

S. Bosanac, Phys. Rev. A, **22**, 2617 (1980)

C. V. Boughton, R. E. Miller, P. F. Vohralik and R. O. Watts, Mol. Phys., **58**, 827 (1986)

J. M. Bowman and S. C. Leasure, J. Chem. Phys., **66**, 288 (1977)

C. L. Brooks, III, M. Karplus and B. M. Pettitt, Adv. Chem. Phys., **71**, 1 (1988)

P. Brumer, Chem. Phys. Lett., **28**, 345, (1974)

U. Buck, Adv. Chem. Phys., **30**, 313 (1975)

U. Buck, Comments At. Mol. Phys., **17**, 143 (1986)

U. Buck, Comments At. Mol. Phys., **17**, 541 (1979)

U. Buck, F. Huisken, J. Schleusener and J. Schäfer, J. Chem. Phys., **72**, 1512 (1980)

U. Buck, Faraday Discuss. Chem. Soc., **73**, 187 (19482)

U. Buck, H. Meyer and R. J. LeRoy, J. Chem. Phys., **80**, 5589 (1984)

U. Buck, *Atomic and Molecular Beam Methods*, vol. 1, ed. G. Scoles, Oxford U. Press, Oxford, (1988) Chap. 18, 21

U. Buck, M. Kick and H. Pauly, J. Chem. Phys., **56**, 4925 (1974)

U. Buck, Rev. Mod. Phys., **46**, 369 (1974)

A. D. Buckingham, P. W. Fowler and J. M. Hutson, Chem. Rev., **88**, 963 (1988)

U. Burkett and N. L. Allinger, *Molecular Mechanics*, American Chemical Society, Washington, D. C. (1982)

D. Chase, Phys. Rev., **104**, 838 (1956)

M. S. Child and D. J. Nesbitt, Chem. Phys. Lett., **149**, 404 (1988)

M. S. Child, *Molecular Collision Theory*, Academic Press, London, (1974), pp. 143-144

M. S. Child, *Molecular Collision Theory*, Academic Press, New York (1974), pp. 141-148

A. P. Clark, A. S. Dickinson and D. Richards, Adv. Chem. Phys., **36**, 63 (1977)

C. F. Curtiss and F. T. Adler, J. Chem. Phys., **20**, 249 (1952)

P. J. Dagdigian, *Atomic and Molecular Beam Methods*, vol. 1, ed. G. Scoles, Oxford U. Press, Oxford, (1988), Chap. 23

L. J. Danielson and M. Keil, J. Chem. Phys., **88**, 851 (1988)

A. E. DePristo, J. Chem. Phys., **78**, 1237 (1983)

A. S. Dickinson, Comp. Phys. Comm., **17**, 51 (1979)

P.A. M. Dirac, *The Principles of Quantum Mechanic* Oxford University Press, (1947), pp.113-125

T. A. Dixon, C. H. Joyner, F. A. Baiocchi and W. Klemperer, J. Chem. Phys., **74**, 6539 (1981)

C. Douketis, G. Scoles, S. Marchetti, M. Zen and A. J. Thakkar, J. Chem. Phys., **76**, 3057 (1982)

C. Douketis, J. M. Hutson, B. J. Orr and G. Scoles, Mol. Phys., **52**, 763 (1984)

L. Dunfield, A. Burgess and H. Scheraga, J. Phys. Chem., **82**, 2609 (1978)

R. Düren, R. K. B. Helbing and S. Miloševič, Chem. Phys., **151**, 287 (1991)

M. A. Dvorak, S. W. Reeve, W. A. Burns, A. Grushow and K. R. Leopold, Chem. Phys. Lett., **185**, 399 (1991)

Y. B. Fan, L. J. Rawluk and M. Keil, J. Opt. Soc.Am. B, **8**, 1218 (1991)

J. M. Farrar and Y. T. Lee, Chem. Phys. Lett., **26**, 428 (1974)

J. T. Farrell, Jr., O. Sneh, A. McIlroy, A. E. Knight and D. J. Nesbitt, J. Chem. Phys., **97**, 7967 (1992)

M. Faubel, K. H. Kohl and J. P. Toennies, J. Chem. Phys., **73**, 2506 (1980)

M. Faubel, K. H. Kohl, J. P. Toennies, K. T. Tang and Y. Y. Yung, Faraday Discuss. Chem. Soc., **73**, 205 (1982)

M. A. D. Fluendy and K. P. Lawley, *Chemical Applications of Molecular Beams*, Chapman and Hall, London (1973), p.24

K. W. Ford and J. A. Wheeler, Ann. Phys., **7**, 259 (1959)

G. T. Fraser and A. S. Pine, J. Chem. Phys., **85**, 2502 (1986)

A. García-Vela and R. B. Gerber, J. Chem. Phys., **97**, 3297 (1992)

C. W. Gear, *Numerical Initial Value Problems in Ordinary Differential Equations*, Prentice Hall, Englewood Cliffs, NJ (1971)

C. F. Geise and W. R. Gentry, Phys. Rev., **A10**, 2156 (1974)

W. R. Gentry, *Atom-Molecule Collision Theory*, ed. R. B. Bernstein, (Plenum Press, New York, 1979) pp. 397-401

R. B. Gerber and R. Alimi, Israel J. Chem., **31**, 383 (1991)

G. Gioumousis and C. F. Curtiss, J. Math. Phys., **2**, 96 (1961)

B.B. Grayce, R.T. Skodje and J.M. Hutson, J. Chem. Phys., **98**, 3929 (1993).

S. J. Harris, S. E. Novick and W. Klemperer, J. Chem. Phys., **74**, 6539 (1981)

J. A. Harrison and H. R. Mayne, J. Chem. Phys., **88**, 7424 (1988)

K. Haug and H. Metiu, J. Chem. Phys., **97**, 4781 (1992)

U. Hefter, P. L. Jones, A. Mattheus, J. Witt, K. Bergmann and R. Schinke, Phys. Rev. Lett., **46**, 915 (1981)

J. Hepburn, G. Scoles and R. Penco, Chem. Phys. Lett., **36**, 451 (1975)

J. O. Hirschfelder, Ber. Bunsenges. Phys. Chem., **86**, 349 (1982)

Z. S. Huang, K. W. Jucks and R. E. Miller, J. Chem. Phys., **85**, 6905 (1986)

L. W. Hunter and C. F. Curtiss, J. Chem. Phys., **58**, 3884 (1973)

J. M. Hutson and B. J. Howard, Mol. Phys., **43**, 493 (1981)

J. M. Hutson and B. J. Howard, Mol. Phys., **45**, 769 (1982)

J. M. Hutson and B. J. Howard, Mol. Phys., **45**, 791 (1982)

J. M. Hutson, Ann. Rev. Chem. Phys., **41**, 123 (1990)

J. M. Hutson, J. Chem. Phys., **96**, 6752 (1992)

B. Jackson, J. Phys. Chem., **93**, 7699 (1989)

P. L. Jones, U. Hefter, A. Mattheus, J. Witt, K. Bergmann, W. Müller, W. Meyer, and R. Schinke, Phys. Rev. B, **26**, 1283 (1982)

P. L. Jones, E. Gottwald, U. Hefter and K. Bergmann, J. Chem. Phys., **78**, 3838 (1983)

P. L. Jones, U. Hefter, A. Mattheus, J. Witt, W. Müller, W. Meyer and R. Schinke, Phys. Rev. B, **26**, 1283 (1982)

S. D. Jones, J. E. Shirley, M. T. Vonk, C. F. Giese and W. R. Gentry, J. Chem. Phys., **97**, 7831 (1992)

M. Karplus, R. N. Porter and R. D. Sharma, J. Chem. Phys., **43**, 3259 (1965)

M. R. Keenan, L. W. Buxton, E. J. Campell, A. C. Legon and W. H. Flygare, J. Chem. Phys., **74**, 2133 (1981)

R. M. Keenan, L. W. Buxton, T. J. Balle and W. H. Flygare, Chem. Phys., **54**, 173 (1981)

M. Keil, J. T. Slankas and A. Kuppermann, J. Chem. Phys., **70**, 541 (1979)

M. Keil and H. R. Mayne, Chem. Phys. Lett., **85**, 456 (1982)

O. Klein, Z. Phys., **76**, 226 (1932)

R. Klein, Z. Phys., **80**, 514 (1933)

R. Rydberg, Z. Phys., **73**, 326 (1931)

D. A. V. Kliner, A. D. Adelman and R. N. Zare, J. Chem. Phys., **95**, 214 (1991)

D. A. V. Kliner, D. E. Adelman and R. N. Zare, J. Chem. Phys., **95**, 1648 (1991)

P. Kollman, Ann. Rev. Phys. Chem., **38**, 303 (1987)

H. Kornweitz, A. Perksy and M. Baer, J. Chem. Phys., **94**, 5524 (1991)

H. J. Korsch and R. Schinke, J. Chem. Phys., **73**, 1222 (1980)

H. J. Korsch and R. Schinke, J. Chem. Phys., **75**, 3850 (1981)

D. J. Kouri, *Atom-Molecule Collision Theory*, ed. R. B. Bernstein, Plenum, NY, (1979), Chap. 9

L.J. Kovalenko, S.R. Leone and J.B. Delos, J. Chem. Phys., **91**, 6948(1989)

A. Kuppermann and G. C. Schatz, J. Chem. Phys., **62**, 2502 (1975)

Y. T. Lee, J. D. McDonald, R. P. LeBreton and D. R. Herschbach, J. Chem. Phys., **49**, 2447 (1968)

W. A. Lester, Jr., Meth. Comput. Phys., **10**, 211 (1971)

R. D. Levine and R. B. Bernstein, *Molecular Reaction Dynamics and Chemical Reactivity*, Oxford University Press, New York, (1987), p. 861

R. D. Levine and R. B. Bernstein, *Molecular Reaction Dynamics and Chemical Reactivity*, Oxford U. Press, (1987) pp.68-70

J. C. Light, *Atom-Molecule Collision Theory*, ed. R. B. Bernstein, Plenum, NY, (1979), Chap. 6

H. J. Loesch, Adv. Chem. Phys., **52**, 421 (1980)

C. M. Lovejoy and D. J. Nesbitt, J. Chem. Phys., **91**, 2790 (1989)

C. M. Lovejoy, J. M. Hutson and D. J. Nesbitt, J. Chem. Phys., **97**, 8009 (1992)

C. M. Lovejoy, M. D. Schuder and D. J. Nesbitt, Chem. Phys. Lett., **127**, 374 (1986)

C. M. Lovejoy, M. D. Schuder and D. J. Nesbitt, J. Chem. Phys., **85**, 4890 (1986)

G. C. Maitland, M. Rigby, E. B. Smith and W. A. Wakeham, *Intermolecular Forces*, Clarendon, London, (1981)

R. A. Marcus, Chem. Phys. Lett., **7**, 525 (1970)

R. A. Marcus, J. Chem. Phys., **54**, 3965 (1971)

R. A. Marcus, J. Chem. Phys., **59**, 5135 (1973)

H. R. Mayne and M. Keil, J. Phys. Chem., **88**, 883 (1984)

P. McGuire and D. J. Kouri, J. Chem. Phys., **60**, 2488 (1974)

P. McGuire, Chem. Phys. Lett., **23**, 575 (1973)

A. Metropoulos and D. M. Silver, J. Chem. Phys., **81**, 1682 (1984)

W. B. Miller, S. A. Safron and D. R. Herschbach, Discuss. Faraday. Soc., **44**, 108 (1967)

W. H. Miller and S. Shi, J. Chem. Phys., **75**, 2258 (1981)

W. H. Miller, Adv. Chem. Phys., **25**, 69 (1974)

W. H. Miller, J. Chem. Phys., **53**, 1949 (1970)

F. A. Morse, R. B. Bernstein and H. U. Hostettler, J. Chem. Phys., **36**, 1947 (1962)

N. F. Mott, Proc. Camb. Phil. Soc. Math. Phys. Sci., **27**, 553 (1931)

T. Mulloney and G. C. Schatz, Chem. Phys., **45**, 213 (1980)

D. J. Nesbitt, M. S. Child, and D. C. Clary, J. Chem. Phys., **90**, 4855 (1989)

L. Nilsson and M. Karplus, J. Comp. Chem., **7**, 591 (1986)

R. T Pack, Chem. Phys. Lett., **55**, 197 (1978)

R. T Pack, E. Piper, G. A. Pfeffer and J. P. Toennies, J. Chem. Phys., **80**, 4940 (1984)

R. T Pack, J. Chem. Phys., **60**, 633 (1974)

R. T Pack, J. J. Valentini, C. H. Becker and Y. T. Lee, J. Chem. Phys., **77**, 5475 (1982)

G. A. Parker and R. T Pack, J. Chem. Phys., **68**, 1585 (1978)

M. Pattengill, J. Chem. Phys., **66**, 5042 (1977)

J. C. Polanyi and K. B. Woodall, J. Chem. Phys., **56**, 1563 (1963)

W. H. Press, S. A. Teukolsky, W. T. Vetterling and B. P. Flanery, *Numerical Recipes*, Cambridge U. Press, New York (1992) pp. 145-148

L. M. Raff and D. L. Thompson, *Chemical Reaction Dynamics*, ed. M. Baer, CRC Press, Boca Raton, FL (1985), p.41

L. M. Raff, D. L. Thompson, L. B. Sims and R. N. Porter, J. Chem. Phys., **56**, 5998 (1972)

L. J. Rawluk and M. Keil, J. Opt. Soc.Am. B, **6**, 1278 (1989)

L. J. Rawluk, M. Keil, M. H. Alexander, H. R. Mayne and J. J. C. Barrett, Chem. Phys. Lett., **202**, 291 (1993)

L. J. Rawluk, Y. B. Fan, Y. Apelblat and M. Keil, J. Chem. Phys., **94**, 4205 (1991)

A. L. G. Rees, Proc. Phys. Soc. London, **59**, 998 (1947)

W. R. Rodwell and G. Scoles, J. Phys. Chem., **86**, 1053 (1982)

W. R. Rodwell, L. T. Sin Fai Lam and R. O. Watts, Mol. Phys., **44**, 2265 (1981)

K. Rudolph and J. P. Toennies, J. Chem. Phys., **65**, 4483 (1976)

G. C. Schatz and A. Kuppermann, J. Chem. Phys., **65**, 4668 (1976)

G. C. Schatz and M. A. Ratner, *Quantum Mechanics in Chemistry*, Prentice Hall, Engelwood Cliffs, NJ, (1993), p. 60

G. C. Schatz, Ann. Rev. Phys. Chem., **39**, 317 (1988)

G. C. Schatz, Top. Curr. Phys., **33**, 25 (1983)

W. Schepper, U. Ross and D. Beck, Z. Phys. A, **290**, 131 (1979)

H. A. Scheraga, Adv. Phys. Org. Chem., **6**, 103 (1968);

R. Schinke, Phys. Rev. B, **26**, 1283 (1982)

R. Schinke and H. J. Korsch, Chem. Phys. Lett., **74**, 449 (1980)

R. Schinke and J. M. Bowman, *Molecular Collision Dynamics*, ed. J. M. Bowman, Springer, Berlin (1982), Chapter 4

R. Schinke, H. J. Korsch and D. Poppe, J. Chem. Phys., **77**, 6005 (1982)

R. Schinke, H. Krüger, V. Hermann, H. Schmidt, and F. Linder, J. Chem. Phys., **67**, 1187 (1977)

R. Schinke, W. Müller and W. Meyer, J. Chem. Phys., **76**, 895 (1982)

R. Schinke, W. Müller, W. Meyer and P. McGuire, J. Chem. Phys., **74**, 3916 (1981)

B. Schramm and U. Leuchs, Ber. Bunsenges. Phys. Chem., **83**, 847 (1979)

D. Secrest, *Atom-Molecule Collision Theory*, ed. R. B. Bernstein, Plenum, NY, (1979), Chap. 8

D. Secrest, J. Chem. Phys., **62**, 710 (1975)

J. A. Serri, A. M. Morales, W. Moskowitz, D. E. Pritchard, C. H. Becker and J. L. Kinsey, J. Chem. Phys., **72**, 6304 (1980)

Y. Shimoni and D. J. Kouri, J. Chem. Phys., **65**, 706 (1976)

D. M. Silver, Comp. Phys. Commun., **14**, 91 (1978)

D. M. Silver, J. Chem. Phys., **72**, 6445 (1980)

G. Starkshall and R. G. Gordon, J. Chem. Phys., **54**, 663 (1970)

A. G. Suits, L. S. Bontuyan, P. L. Houston and B. J. Whitaker, J. Chem. Phys., **96**, 8618 (1992)

J. R. Taylor, *An Introduction to Error Analysis*, University Science Books, Mill Valley, CA, (1982), p. 112

J. Tellinghuisen, Comput. Phys. Commun., **6**, 221 (1974)

D. L. Thompson, J. Chem. Phys., **67**, 5224 (1977)

D. L. Thompson, J. Chem. Phys., **76**, 5947 (1982)

J. P. Toennies, *Physical Chemistry - An Advanced Treatise*, v. 6A, ed. H. Eyring, D. Henderson and W. Jost, Academic Press, New York, NY (1974), Chap. 5

D. G. Truhlar, ed., *Resonances in Electron-Molecule Scattering, van der Waals Complexes and Reactive Chemical Dynamics Calculations*, ACS Symp. Ser. 263., Am. Chem. Soc., Washington, DC, (1984), 552

R. M. van Aalst, J. A. Schuurman and J. Elsken, Chem. Phys. Lett., **35**, 558 (1975)

P. F. Vohralik, R. E. Miller and R. O. Watts, J. Chem. Phys., **90**, 2182 (1989)

P. F. Vohralik, R. E. Miller and R. O. Watts, J. Chem. Phys., **90**, 913 (1982)

P. F. Vohralik, R.E. Miller and R.O. Watts, J. Chem. Phys., **90**, 2182 (1989)

A. F. Wagner and A. C. Wahl, J. Chem. Phys., **69**, 3756 (1978)

D. Wang and J. M. Bowman, J. Chem. Phys., **96**, 8906 (1992)

T. T. Warnock and R. B. Bernstein, J. Chem. Phys., **49**, 1878 (1968)

Special issue of Ber. Bunsenges. Phys. Chem., **86**, 348-483 (1982)